Spring 2013

Size-dependent reactivity of hematite nanoparticles: environmental implications of dissolution mechanisms and aggregation

Caylyn Ashley Lanzl
University of Iowa

SIZE-DEPENDENT REACTIVITY OF HEMATITE NANOPARTICLES: ENVIRONMENTAL IMPLICATIONS OF DISSOLUTION MECHANISMS AND AGGREGATION

by

Caylyn Ashley Lanzl

An Abstract

Of a thesis submitted in partial fulfillment
of the requirements for the Doctor of
Philosophy degree in Civil and Environmental Engineering
in the Graduate College of
The University of Iowa

May 2013

Thesis Supervisor: Associate Professor David M. Cwiertny

ABSTRACT

The interfacial reactivity of iron oxides such as hematite (α-Fe_2O_3) has been extensively studied because they are naturally abundant materials that are also versatile in a range of engineering applications. A poorly understood determinate of iron oxide interfacial reactivity is their particle size, a factor that has received increasing scrutiny given the emergence of nanoscience and nanotechnology. In natural systems, size-dependent trends in dissolution may have a profound influence on the rate and extent of iron redox cycling, which will indirectly effect the numerous processes in which soluble ferric [Fe(III)] and ferrous [Fe(II)] iron subsequently participate.

This work seeks to establish (i) the size-dependent dissolution of hematite nanoparticles across a range of dissolution mechanisms (e.g. proton-promoted, ligand-promoted, thermal reductive and photoreductive dissolution) and pH values, (ii) the extent to which nanoparticle aggregation effects the reactivity of hematite nanoparticles and trends observed in size-dependent reactivity of such aggregates, and (iii) how size-dependent dissolution activity of hematite impacts the production of environmentally relevant reactive oxygen species in sunlit surface waters via the photo-Fenton chemical reaction. Results herein reveal that size-dependent reactivity for two sizes of hematite nanoparticles, 8 and 40 nm, is observed throughout all dissolution processes and mechanisms investigated. Notably, this work is among the first where size-dependent reactivity is clearly observed into circumneutral and neutral pH values representative of most natural systems. Enhanced reactivity of the smaller 8 nm hematite is likely due to available reactive surface area compared to its larger analog. Under native aggregation of nanopowders (i.e., minimal ionic strength and no sonication) and induced aggregation of nanoparticle suspensions (i.e. high ionic strengths) mass normalized rates of reductive dissolution were greater for aggregates of 8 nm hematite, and aggregate size exhibited little influence on size-dependent reactivity. Finally, size-dependent reactivity also occurs

in model surface water reactions, specifically the dissolved organic matter mediated photo-Fenton reaction. Smaller nanophase hematite exhibits greater rates of Fe(II) production, which in turn yields greater steady-state hydroxyl radical concentrations. Insights from this work advance current knowledge of size-dependent reactivity of natural nanomaterials and their implications for pollutant fate and elemental cycling in environmental systems.

Abstract Approved: _____
Thesis Supervisor

_____
Title and Department

_____
Date

SIZE-DEPENDENT REACTIVITY OF HEMATITE NANOPARTICLES: ENVIRONMENTAL IMPLICATIONS OF DISSOLUTION MECHANISMS AND AGGREGATION

by

Caylyn Ashley Lanzl

A thesis submitted in partial fulfillment
of the requirements for the Doctor of
Philosophy degree in Civil and Environmental Engineering
in the Graduate College of
The University of Iowa

May 2013

Thesis Supervisor: Assistant Professor David M. Cwiertny

Graduate College
The University of Iowa
Iowa City, Iowa

CERTIFICATE OF APPROVAL

PH.D. THESIS

This is to certify that the Ph.D. thesis of

Caylyn Ashley Lanzl

has been approved by the Examining Committee
for the thesis requirement for the Doctor of Philosophy
degree in Civil and Environmental Engineering at the May 2013 graduation.

Thesis Committee: _____
David M. Cwiertny, Thesis Supervisor

_____
Edward G. Gillan

_____
Sarah C. Larsen

_____
Michelle M. Scherer

_____
Richard L. Valentine

To my family, thank you for all the love and support.

ACKNOWLEDGMENTS

First and foremost I would like to extend my sincerest gratitude to my thesis advisor, Dr. David Cwiertny, whose guidance, patience, and optimism was exceptional and essential for receiving my doctorate. His mentorship provided me the opportunity to excel as both a student and researcher. Skills that I have learned under his mentorship are invaluable and will undoubtedly be essential for my future career as an engineer. One could not ask for a more sincere and friendly advisor with a penchant for tackling scientific inquires enthusiastically and creatively.

I would also like to thank my friends and colleagues who helped to make my graduate school experience great. Specifically, Rebekah Oulton, Dr. Shen Qu, Edgard Verdugo, and Dr. Yang Xie whose discussion, guidance, and camaraderie made working in lab enjoyable and fun. Our graduate experience was unique, we started in California and moved to Iowa, which for many of us was both exciting and difficult, but it was an adventure nonetheless, which I am glad to have shared with you all.

I would like to thank my thesis committee, Michelle Scherer, Richard Valentine, Sarah Larsen, and Ed Gillan, for their expertise and valuable input that went into shaping and improving my work. Their careers in the scientific field have yielded numerous advances in science and engineering, some of which have contributed to the foundations of my specific research, and provided me both inspiration and invaluable knowledge. Your insightful opinions, discussion, and questions have led to improvement in my research and thesis, of which I am very grateful.

Collaborators throughout my graduate work have added to my outstanding graduate experience. Dr. Sharon Walker and Dr. Amy Gong at the University of California Riverside, whose guidance, input, and collaboration was a pleasure. Also, Dr. Jonas Baltrusaitus who now resides at the University of Twente. He has helped me tremendously with material characterization and shared valuable insights and discussion regarding our work. Additionally, I would like to thank the department of Chemical and

Environmental Engineering at UCR for giving me the opportunity to pursue a doctorate and the department of Environmental Engineering and Sciences at the University of Iowa for accepting me into this exceptional program with unparalleled faculty and research opportunities.

Finally, I would like to thank my family for all their unwavering support, love, and encouragement throughout this process. My parents, Bruce Lanzl and Catherine Carlson-Lanzl have supported and encouraged me throughout my life to pursue my dreams no matter how difficult. Their unconditional love and guidance has shaped me into the person I am today, it is because of them that I have achieved so much in both my personal life and my career. I would especially like to thank my older brother, Justin, for his support, tutoring, and encouragement. Like many older siblings he had to cope with me copying everything he did, including becoming an engineer which has led me to where I am today, so thank you for being such a great role model and brother. I would also like to thank my grandmother, Eunice Lanzl, for her love and support. Lastly, I would like to thank my fiancée, Dr. Tracy Kam, whose love and support has been the light in my life for the last seven years, without which my success would not have been possible. We both pursued our graduate degrees at the same time, in different fields, yet we found support and strength in each other's struggles and successes.

ABSTRACT

The interfacial reactivity of iron oxides such as hematite (α-Fe_2O_3) has been extensively studied because they are naturally abundant materials that are also versatile in a range of engineering applications. A poorly understood determinate of iron oxide interfacial reactivity is their particle size, a factor that has received increasing scrutiny given the emergence of nanoscience and nanotechnology. In natural systems, size-dependent trends in dissolution may have a profound influence on the rate and extent of iron redox cycling, which will indirectly effect the numerous processes in which soluble ferric [Fe(III)] and ferrous [Fe(II)] iron subsequently participate.

This work seeks to establish (i) the size-dependent dissolution of hematite nanoparticles across a range of dissolution mechanisms (e.g., proton-promoted, ligand-promoted, thermal reductive and photoreductive dissolution) and pH values, (ii) the extent to which nanoparticle aggregation effects the reactivity of hematite nanoparticles and trends observed in size-dependent reactivity of such aggregates, and (iii) how size-dependent dissolution activity of hematite impacts the production of environmentally relevant reactive oxygen species in sunlit surface waters via the photo-Fenton chemical reaction. Results herein reveal that size-dependent reactivity for two sizes of hematite nanoparticles, 8 and 40 nm, is observed throughout all dissolution processes and mechanisms investigated. Notably, this work is among the first where size-dependent reactivity is clearly observed into circumneutral and neutral pH values representative of most natural systems. Enhanced reactivity of the smaller 8 nm hematite is likely due to available reactive surface area compared to its larger analog. Under native aggregation of nanopowders (i.e., minimal ionic strength and no sonication) and induced aggregation of nanoparticle suspensions (i.e., high ionic strengths) mass normalized rates of reductive dissolution were greater for aggregates of 8 nm hematite, and aggregate size exhibited little influence on size-dependent reactivity. Finally, size-dependent reactivity also occurs in model surface water reactions, specifically the dissolved organic matter mediated

photo-Fenton reaction. Smaller nanophase hematite exhibits greater rates of Fe(II) production, which in turn yields greater steady-state hydroxyl radical concentrations. Insights from this work advance current knowledge of size-dependent reactivity of natural nanomaterials and their implications for pollutant fate and elemental cycling in environmental systems.

TABLE OF CONTENTS

LIST OF TABLES IX

LIST OF FIGURES X

CHAPTER 1. INTRODUCTION 1

1.1 Nanoscale effects 1
1.2 Nanoscale iron oxide occurrence and applications 2
1.3 Importance of nanoscale iron oxide dissolution 3
1.4 Aggregation and size-dependent trends 9
1.5 Iron oxide nanoparticles in surface water 11
1.6 Overview and thesis organization 13
1.7 Expected outcomes 14

CHAPTER 2. DISSOLUTION OF HEMATITE NANOPARTICLE AGGREGATES: INFLUENCE OF PRIMARY PARTICLE SIZE, DISSOLUTION MECHANISM, AND SOLUTION pH 19

2.1 Abstract 19
2.2 Introduction 20
2.3 Experimental methods 23
2.4 Results and discussion 30
2.5 Conclusion 41

CHAPTER 3. INFLUENCE OF AGGREGATE SIZE EFFECTS ON THE REDUCTIVE DISSOLUTION OF NANOSCALE HEMATITE 57

3.1 Abstract 57
3.2 Introduction 58
3.3 Experimental methods 61
3.4 Results and discussion 67
3.5 Conclusion 77

CHAPTER 4. INFLUENCE OF HEMATITE PRIMARY PARTICLE SIZE ON DOM-MEDIATED PHOTOREDUCTIVE DISSOLUTION IMPLICATIONS FOR THE FENTON REACTION 89

4.1 Abstract 89
4.2 Introduction 90
4.3 Experimental methods 94
4.4 Results and discussion 100
4.5 Conclusion 107

CHAPTER 5. CONCLUSIONS 118

5.1 Generality of size-dependent dissolution 118
5.2 Influence of aggregation on reactivity 120
5.3 Size-dependent reactivity and ROS production 122
5.4 Future research 123

APPENDIX. INFLUENCE OF VARYING LEVELS OF EXTRACELLULAR POLYMERIC SUBSTANCES(EPS) ON HYDROXYL RADICAL MEDIATED DISINFECTION OF *Escherichia* coli 128
A.1 Abstract 128
A.2 Introduction 129
A.3 Experimental methods 131
A.4 Results and discussion 136
A.5 Conclusion 141

BIBLIOGRAPHY 151

LIST OF TABLES

Table 1-1. Common iron oxide dissolution mechanisms and species involved. 17

Table A-1. Resulting data from photochemical disinfection: rate constant (k) and fitting parameter (m), reduced chi^2, adjusted R^2, and induction time (t_s) 144

Table A- 2. Characterization of EPS content removed from bacterial surfaces by the sonication method 149

LIST OF FIGURES

Figure 1-1. Dispersed particles (left) compared to the same number of particles aggregated (right). Aggregation may affect the rate of reactivity (R) associated with either dispersed particles or tightly aggregated particles. 18

Figure 2-1 Powder X-ray diffraction (XRD) patterns for synthesis products derived from the methods of (a) Sorum [117] and (b) Schwertmann and Cornell [118]. Also provided is the reference pattern (PDF#072-0469) for hematite (α-Fe2O3). For comparison, the diffraction patterns are normalized to the diffraction line with greatest intensity (at 2θ of ~38°). This reveals the expected line broadening for the smaller (8 nm) primary particles produced by the method of Sorum relative to the larger primary particles (~40 nm) obtained from the method of Schwertmann and Cornell.. 45

Figure 2-2 (a) TEM image of the synthesis product from Sorum's method. Based on sizing analysis of 200 particles (b), this method yielded particles that were approximated as spherical (see inset in (a)) with an average diameter, *d,* of 8.1 (± 1.6) nm. (c) TEM image of the synthesis product from the method of Schwertmann and Cornell, which was rhombohedral in shape (see inset in (c)). Sizing of 100 particles suggests they have an average length, *a*, of 39.5 (± 7.9) nm and width, *b*, of 29.2 (±5.4) nm, as defined by dimensions shown in the inset of (c). 46

Figure 2-3 (a) Representative sedimentation curves obtained for 8 and 40 nm hematite suspensions pH 2 and pH 7. Also shown are exponential decay model fits applied to data for $t \leq 15$ min, which were used to determine first-order coefficients for sedimentation [or *k*(sedimentation) values]. Results of linear regression analysis typically yielded R^2 values greater than 0.9 (e.g., the R^2 values for data shown were 0.93 and 0.92 for 8 and 40 nm at pH 2, respectively, and 0.98 and 0.96 for 8 and 40 nm at pH 7, respectively. Sedimentation experiments were conducted with 0.5 g/L suspensions in 25 mM NaCl at an analytical wavelength (λ) of 510 nm. (b) Comparison of *k*(sedimentation) values obtained from sedimentation studies and hydrodynamic diameter values obtained from dynamic light scattering analysis for 8 and 40 nm hematite suspensions. 47

Figure 2-4 Sedimentation rate constants and hydrodynamic diameters based on pH. (a) Initial coefficients for settling [*k*(sedimentation) values] and (b) hydrodynamic diameters from DLS analysis as a function of pH for suspensions of 8 nm and 40 nm hematite (α-Fe_2O_3). Suspensions contained 0.5 g/L α-Fe_2O_3 and 25 mM NaCl (as noted in the text, ionic strength was slightly higher from pH 1-2 due to the HCl concentration necessary to achieve these low pH values). All suspensions were made at least 12 hours in advance and allowed to equilibrate before analysis. Sedimentation coefficients were determined by modeling the initial change (for data $t \leq 15$ min) in light transmittance ($\lambda_{incident}$ = 510 nm) through hematite suspensions as a first-order process (i.e., exponential decay). Uncertainty associated with *k*(sedimentation) values represents 95% confidence levels associated with the linear regression analysis used in their quantification from semi-log plots of absorbance versus time. Uncertainties in hydrodynamic diameters represent standard deviations from triplicate analyses. 48

Figure 2-5 Alkalimetric titrations curves and zeta potential (a) Alkalimetric titration performed on 4 g/L suspensions of 8 and 40 nm hematite. Initially near pH 4.0, suspensions were autotitrated with 0.1 N NaOH until reaching a final pH of 10. Titrations clearly reveal that a larger volume of base was necessary to raise the 8 nm hematite suspension to pH 10, thus indicating its greater base-neutralizing capacity for these particles. (b) Zeta potential measurements as a function of pH for 8 and 40 nm hematite suspensions. Suspensions of 0.5 g/L were prepared in 25 mM NaCl, adjusted to the appropriate pH with dilute acid or base, and subsequently diluted to an absorbance of 0.3-0.35 at λ of 246 nm for zeta potential analysis. 49

Figure 2-6 Representative Fe(III) dissolution curves for proton-promoted dissolution of 8 and 40 nm hematite suspensions Suspensions consist of 0.5 g/L at pH 1. Also shown are the results of best fit linear regression analyses, from which the rate of Fe(III) dissolution was quantified using the resulting slope. For all dissolution mechanisms considered (i.e., proton-promoted, oxalate-promoted, reductive dissolution via ascorbic acid, photoreductive dissolution in irradiated oxalate suspensions), Fe(III) or Fe(II) concentration profiles over time were of comparable quality and all experiments were conducted in triplicate to account for uncertainty. 50

Figure 2-7. Rates of proton-promoted dissolution (blue) and oxalate (1 mM) promoted dissolution (green) for 8 and 40 nm hematite suspensions as a function of pH. Numbers adjacent to 8 nm data points (triangles) indicate their magnitude of rate enhancement (including 95% confidence intervals) relative to 40 nm particles (circles). Lines represent results of best-fit linear regression analyses to determine the empirical relationship between dissolution rate and $\Gamma H^+]$, results of which are provided. All suspensions contained 0.5 g/L α-Fe_2O_3 and 25 mM NaCl (as noted in the text, ionic strength was slightly higher from pH 1-2 due to the HCl concentration necessary to achieve these low pH values). Uncertainties represent one standard deviation from at triplicate dissolution experiments. Dissolution rates were quantified from the initially linear increase in soluble Fe(III) concentration over time as described in the text. Uncertainties associated with rate data represent the 95% confidence interval for the slope of this linear-regression analysis. 51

Figure 2-8 Rate of reductive dissolution via reaction of ascorbic acid (10 mM) with 8 or 40 nm hematite suspensions as a function of pH. Numbers adjacent to 8 nm data points (triangles) indicate their magnitude of rate enhancement (including 95% confidence intervals) relative to 40 nm particles (circles). Lines represent results of best-fit linear regression analyses to determine the empirical relationship between dissolution rate and $[H^+]$, results of which are provided. All suspensions contained 0.5 g/L α-Fe_2O_3 and 25 mM NaCl (as noted in the text, ionic strength was slightly higher at pH 2 due to the HCl concentration necessary to achieve this low pH values). Dissolution rates were quantified from the initially linear increase in soluble Fe(III) concentration over time as described in the text. Uncertainties associated with rate data represent the 95% confidence interval for the slope of this linear-regression analysis. 52

Figure 2-9 Photoreductive dissolution rates, oxalate absorption, and oxalate nomalized photoredutive dissolution rates (a) Rates photoreductive dissolution as a function of pH in hematite suspensions containing 0.5 g/L of 8 and 40 nm α-Fe_2O_3 and 1 mM oxalate. Lines represent results of best-fit linear regression analyses to determine the empirical relationship between dissolution rate and $[H^+]$, results of which are provided. Reactions were conducted in the absence of O_2, and suspensions also contained 25 mM NaCl. Dissolution rates were quantified from the initially linear increase in soluble Fe(III) concentration over time as described in the text. Uncertainties associated with rate data represent the 95% confidence interval for the slope of this linear-regression analysis. (b) Adsorbed oxalate concentration determined from dark control experiments. Adsorbed oxalate concentrations are shown as a function of pH per unit mass of 8 and 40 nm α-Fe_2O_3. (c) Rates of photoreductive hematite dissolution normalized to the concentration of adsorbed oxalate. In all instances, numbers adjacent to 8 nm data points (triangles) indicate their magnitude of rate enhancement (including 95% confidence intervals) relative to 40 nm particles (circles). 53

Figure 2-10 TEM images before and after reductive dissolution. TEM images of 8 and 40 nm hematite before (a and e, respectively) and after reaction with 10 mM ascorbic acid at pH 2 for 20 hours (b and f, respectively) and 13 days (c, d and g, h, respectively). For images of 40 nm hematite, evidence of dissolution along edges (indicated by black arrows) and internal defects (indicated by white outline arrow) is highlighted. 55

Figure 2-11 TEM images before and after oxalate promoted dissolution.TEM images of aggregates of 8 nm hematite (on left) and 40 nm hematite (on right) as a function of reaction time (either 20 h or 14 d) with 1 mM oxalate at pH 2. While TEM images of 8 nm aggregates show little discernible change in the morphology of primary particles comprising the aggregate, 40 nm particles within aggregates exhibit rounding, indicative of preferential etching at their sharpest edges (indicted by black arrows). Also over 14 d, evidence develops for dissolution via internal defects within the hematite (indicated by the white outlined arrow). Similar changes in particle morphology were also observed for aggregates of 8 and 40 nm hematite after reaction with 10 mM ascorbic acid at pH 2 (see Figure 2-10). 56

Figure 3-1. Examples of Fe(II) dissolution curves and dissolution rate analysis for 8 nm hematite. Data are shown for the heavy fraction (~ 7440 µM Fe_T) and light fraction (~ 660 µM Fe_T) obtained after 10 minutes of gravitational settling of a 0.5 g/L suspension. Dissolution rates were determined from the slope obtained via linear regression analysis (shown as solid lines) and then normalized by the total amount of iron measured in each fraction. 79

Figure 3-2. Fraction of total hematite mass present in light and heavy sediment fractions generated as a function of increasing settling time. Data are shown for initial suspensions (0.5 g/L, pH 3, 25 mM NaCl) prepared from powders of both 8 nm (red) and 40 nm (blue) hematite. For each settling time there is a representative point for both the heavy fraction (open markers) and light fraction (closed markers). The lightest fraction generated (with $\leq$ 5 % total hematite mass) was obtained after 40 min settling time, while the heaviest fraction (with 65-70 % total hematite mass) corresponded to the heavy fraction generated at the shortest duration of settling (1 min settling time). 80

Figure 3-3. Cryo-TEM images of representative particles in the lightest fraction (stable after 40 min of settling) of 8 nm (a,b) and 40 nm (c,d) hematite suspensions. These particles comprise the lightest 5% of hematite mass present in suspension mass for each light fraction. Details of image collection and sample preparation are provided in the text. 81

Figure 3-4. SEM images of aggregates present in the heavy fractions of (a) 8 nm and (b) 40 nm hematite suspensions, respectively. Particles represent those deposited out of solution after 40 minutes of settling, corresponding to the ~95% of the total hematite mass initially present in suspensions (0.5 g/L, pH 3, 25 mM NaCl). Details of image collection and sample preparation are provided in the text. 82

Figure 3-5. (a) Average r_M values as a fraction of mass available in gravity-separated fractions of 8 and 40 nm hematite. The numbers below each set of fractions corresponds to the settling time used to generate "light" (shown on the left) and "heavy" (shown on the right) fractions. (b) All r_M values measured for fractions of 8 and 40 nm suspensions. Data in (b) represent those values averaged in (a) at each settling time. (c) Average r_M values for suspension fractions [r_M (fraction)] normalized to r_M value measured for the bulk (i.e., non-fractionated) suspension [r_M (bulk)]. The horizontal dashed line represents a ratio of unity, indicating the reactivity of the suspension fraction is identical to that of the bulk 0.5 g/L suspension. (d) All data points shown for mass normalized rates of each fraction normalized to the rate of the bulk suspension 83

Figure 3-6. Fraction of total iron oxide mass present in light and heavy sediment fractions generated as a function of increasing settling time for goethtite microrods, goethite nanorods, and ferrihydrite. Data is shown for initial suspensions (0.5 g/L, pH 3, 25 mM NaCl) prepared from powders of both goethtite microrods (purple), nanorods (green) and ferrihydrite (orange). For each settling time there is a representative point for both the heavy fraction (open markers) and light fraction (closed markers). 84

Figure 3-7. Average r_M values as a fraction of mass available in gravity-separated fractions the iron oxides considered herein (see key). Solid data points represent experiments conducted with10 mM ascorbic acid at pH 3 low ionic strength (25 mM NaCl) suspensions. Also shown are data collected in high ionic strength (1 M $NaClO_4$) suspensions (open symbols). For each oxide, the dashed horizontal line represents the r_M value measured in a bulk (i.e., non-fractionated) suspensions of each oxide. Uncertainties represent one standard deviation obtained from at least triplicate experiments. 85

Figure 3-8. Sedimentation curves of normalized absorbance (A/A_0) at λ 510 nm for 0.5 g/L (or equivalent) suspensions of iron oxides at pH 3. Solid markers represent data for suspensions in 25 mM NaCl and open markers are data obtained at 1 M $NaClO_4$ 86

Figure 3-9. Representative cryo-TEM images of non-dried suspensions of 8 nm hematite (NAD 8 nm α-Fe_2O_3; left) and 40 nm hematite (NFD 40 nm α-Fe_2O_3; right). 87

Figure 3-10. Dissolved Fe(II) production as a function of time for (a) oxalate-promoted dissolution, (b) proton-promoted dissolution and (c) reductive dissolution with ascorbic acid for suspensions (0.5 g/L) prepared from 8 nm hematite powder. Data represent average and standard deviations from triplicate experiments in 25mM NaCl (red solid symbols) and 1 M $NaClO_4$ (open symbols). Lines represent results of best-fit linear regression analyses from which r_M values were determined from the slope. These r_M values are provided. Oxalate (1 mM) and ascorbic acid (10 mM) mediated dissolution were conducted at pH 3.0, whereas proton promoted dissolution was conducted at pH 2.0. 88

Figure 4-1. Semi-log plot of phenol decay over time in irradiated ($\lambda \geq 305$ nm) suspensions (0.5 g/L) of 8 nm hematite and 5 mg/L of SRHA at pH 3. The pseudo-first order rate constant, k_{obs}, from which steady-state •OH concentrations could be measured was determined from the slope of the best fit linear regression (shown). 110

Figure 4-2. Sorption of SRHA onto 0.5 g/L suspensions of 8 and 40 nm in 25 mM NaCl. At pH 3 (a) sorption capacity of SRHA13 is about two fold greater than at pH 5 (b) for both sizes of hematite at SRHA concentrations greater than 5 mg/L. However all photo-experiments were run at 5 mg/L SRHA loading, for which both 8 and 40 absorb almost all SRHA. Additionally, a separate SRHA09 batch was tested, with sorption onto both sizes of hematite at pH 3 (c) and pH 6 (d). For this particular batch of SRHA sorption onto 8 and 40 nm was equivalent at both pH 3 and 6. 111

Figure 4- 3. Dissolution of Fe(II) in the presence of 5 mg/L SRHA ($\lambda \geq 305$nm) with 0.5g/L suspensions of 8 nm and 40 nm hematite at (a) pH 3 and (b) pH 5. At pH 3, 8 nm hematite produces approximately 3 fold more Fe(II) than its larger counterpart at 5.8 (±1.4) µM Fe(II) h^{-1} and 2 (±0.3) µM Fe(II) h^{-1}, respectively . At pH 5 the rates of production of iron are lower than at pH 3, 2.9 (±0.1) µM Fe(II) h^{-1} and 1.4 ±(0.2) µM Fe(II) h^{-1}, for 8 nm and 40 nm, respectively. Notably, a 2 fold increase in Fe(II) production is still observed for 8 nm hematite nanoparticle suspension compared to 40 nm.....112

Figure 4-4. Sorption for Fe(II) onto the surface of 0.5 g/L 8 and 40 nm hematite buffered at pH 7 under anaerobic conditions. Initial concentrations of Fe(II) ranged from 0-1500 µM. Uptake of Fe(II) is slightly greater for 8 nm hematite and best observed at high concentrations of Fe(II) (> 800 µM). Error bars represent standard deviations based on replicate (at least 3 or more) experiments. 113

Figure 4- 5. Irradiated ($\lambda \geq 305$ nm) suspensions of 0.5 g/L hematite suspensions with 5 mg/L SRHA. Initial concentrations of phenol were approximately 100 µM. Phenol decay was measured over time at both pH 3 (filled markers) and pH 5 (open markers). At pH 3 $[•OH]_{ss}$ measurements were about 4 times greater for 8 nm suspension at 3 $x10^{-15}$ M compared to 8 $x10^{-16}$ for the 40 nm suspension. At pH 5 suspensions of 8 nm hematite produced about 6 $x10^{-16}$ M steady-state hydroxyl radical. At pH 5 suspensions of 40 nm showed insufficient phenol decay, thus accurate determination of $[•OH]_{ss}$ was not possible. 114

Figure 4-6. Control experiments to ensure phenol decay was an iron dependent process. Initial controls with only irradiated ($\lambda \geq 305$ nm) 5 mg/L SRHA showed no phenol decay. Irradiated reactors with 0.5 g/L 8 nm hemaitite, 5mg/L SRHA, and 0.2 mg/mL DFOM had no observable phenol decay. Finally, dark controls using 0.5 g/L 8 nm hematite and 5 mg/L SRHA showed no probe decay. Phenol decay at pH 3 is shown for reference. 115

Figure 4-7. H_2O_2 production in 5 mg/L SRHA ($\lambda \geq 305$ nm) at pH 3 with no iron oxide present. From a simple linear regression, H_2O_2 production rate was determined to be approximately 2 $\mu M\ h^{-1}$. Similar concentrations were observed at higher pH as well. 116

Figure 4-8. H_2O_2 production (solid diamonds) from 5 mg/ L SRHA ($\lambda \geq 305$ nm) with no iron oxide present at pH 3. At 2.5 hours 8 nm hematite (0.5g /L) was added to the irradiated reactor (open diamonds). After addition of the iron oxide decay of photo-generated H_2O_2 in solution was observed. Controls were performed using SRHA in the dark (open circles) in which no H_2O_2 was detected. Additional controls using reactors spiked with H_2O_2 (~ 10 μM) in 0.5 g/L suspensions of 8 nm and 40 nm hematite in the dark showed no measurable amount of H_2O_2 decay. This suggests that decay shown (open diamonds) in irradiated suspensions of 5 mg/L SRHA with the addition of 8 nm hematite was due to Fenton-like processes. 117

Figure A-1. Plots of *E. coli* DC1 exposed to light with wavelength ≥ 305 nm. a) Disinfection data presented as the natural log of cell viability normalized by initial viability versus the time of light exposure as a function of steady-state hydroxyl radical concentration ($[\bullet OH]_{ss}$). b) Results from non-linear regression analysis obtained from best-fit analyses of data presented in (a) with equation 1. The induction time (t_s) and viability loss rate constant (k) are shown as a function of steady-state hydroxyl radical concentration. Note that direct photochemical disinfection is the only process occurring when $[\bullet OH]_{ss}=0$. 143

Figure A-2. (a) Normalized phenol decay ([P] = phenol concentration; $[P]_0$= initial phenol concentration) over time indicates the production of hydroxyl radical (•OH) by nitrate at wavelengths ≥ 305 nm. (b) Calculated steady-state hydroxyl radical concentrations ($[\bullet OH]_{ss}$) as a function of nitrate concentration (mg/L).These •OH concentrations (4.37×10^{-16} - 1.70×10^{-15} M) generated over the range of aqueous nitrate concentrations (50-500 mg/L) are slightly lower than other studies of •OH production from nitrate photolysis, most likely due to differences in our reactor setup and lamp power output. 146

Figure A-3. Plots of *E. coli* DC1 exposed to light at wavelength ≥ 305 nm conducted at 0 and 1.7×10^{-15}M $[\bullet OH]_{ss}$ with or without the presence of excess formate ($CHOO^-$, 50 mM), a known •OH scavenger. Data presented as the natural log of cell viability normalized by initial viability versus the time of light exposure. Data is consistent•OH as the primary agent responsible for bacteria kill in all systems. Photochemical experiments with *E. coli* DC1 that were conducted with $[\bullet OH]_{ss}$ in the presence of excess formate revealed viability losses consistent with a direct photochemical reaction only. 147

Figure A-4 *E. coli* was exposed to light ≥ 305 nm as a function of EPS level.(a) Changing viability in cell population due to *direct* (open symbols) and *indirect* (symbols with dot in center). Indirect disinfection experiments were conducted in the presence of 250 mg/L nitrate which generated $[\bullet OH]_{ss}=1.39 \times 10^{-15}$ M. Data are presented as the natural log of cell viability normalized by initial viability versus the time of light exposure. The remaining figures provide the rate constant, k (min^{-1}) and induction time, t_s (min) with respect to sonication times for experiments conducted (b) in the presence ($[\bullet OH]_{ss}=1.39\times10^{-15}$ M) and (c) absence ($[\bullet OH]_{ss}=0$) of photochemically generated hydroxyl radical. In panels (b) and (c), longer sonication times imply a greater extent of EPS removal. For systems conducted with $[^{\bullet}OH]_{ss} = 1.39\times10^{-15}$ M, values of k and t_s are also shown with respect to (d) total EPS, (e) protein, and (f) sugar removed from cell surfaces.....148

Figure A-5. Bacteria was exposed to light ≥ 305 nm as a function of EPS level. (a) Photochemical disinfection of *E. coli* strains DC1, HU1, SP4, and O157:H7 in the presence of a constant hydroxyl radical concentration ($[\bullet OH]_{ss}=1.39\times10^{-15}$ M). The EPS was removed via 300 s sonication and compared to full EPS presence. Data presented as the natural log of cell viability normalized by initial viability versus the time of light exposure. The remaining figures provide the rate constant, k (min^{-1}) and induction time, t_s (min) with respect to (b) total EPS, (c) protein, and (d) sugar removed from cell surfaces..... 150

CHAPTER 1
INTRODUCTION

This work explores the size-dependent reactivity of iron oxides. The content herein spans a range of concepts from nanoscale reactivity to broad behavior of iron oxides in the natural environments. Specifically this work investigates size-dependent reactivity with regard to dissolution mechanisms and solution chemistries, the impact of aggregation on size-dependent reactivity, and reactivity in model photochemical reactions present in environmental systems. Collectively, it encompasses many pathways that may be encountered for nanoscale iron oxide reactivity in aqueous media.

1.1 Nanoscale effects

Nanoscale science and technology has been extensively studied since the topic's inception by Richard Feynman [1]. Nanomaterials are those defined as having a characteristic dimension between 1 to 100 nm in size [2]. The driving force behind nanoscale engineering is the ability to control fabrication down at an atomic level, a process Feynman termed the "bottom-up" approach. While the field is relatively young it has extensive capabilities that have been utilized in commercial products and cutting edge research.

As materials are manipulated down to nanometer scales, classic reactivity that may be observed in the same material at larger scales diverges, a phenomenon that has been termed "nanoeffects". Divergence from bulk material behavior is observed at these small scales for a variety of properties, including optical, electrical, and magnetic properties due to quantum effects of atoms within materials [3]. An example of this behavior is best observed with CdSe quantum dots [4]. As the semiconductor crystal size is decreased quantum confinement effects become apparent, as bandgap energies associated with fluorescence increase, and upon excitation light is emitted at a shorter wavelength (higher energy) than would be seen from a larger semiconductor crystal [5,

6]. Quantum dots allow for the unique ability to visualize nanoscale size effects, but decreasing the size of particles can also have a large impact on less obvious properties, such as thermal properties [7-9] (i.e., melting point) and inherent magnetism [10, 11].

An essential aspect of nanoscale engineering, and perhaps the most obvious, is the surface area to volume ratio of nanoparticles compared to their larger counterparts[3]. Increases in surface area can serve to enhance chemical reactivity due to greater availability of reactive surface sites [3] and greater surface energies associated with surface atoms versus bulk atoms [12]. Increases in specific surface area have substantial implications for heterogeneous reactions that rely of surface availability, such as catalytic reactions that are used in fuel cells [13]. Intuitively dissolution rates for a particular mass of material would be expected to scale with available surface area, which in turn controls the concentration of surface sites at which the dissolution reaction will occur. However, for nanoparticles, changes in surface energy associated with decreasing crystal grain sizes may enhance dissolution to rates not achievable with larger analogs [14]. For instances of engineered nanomaterial discharged into the environment, these enhancements in dissolution activity could be associated with greater nanotoxicity [15]. In other instances, inherently greater dissolution activity for certain natural nanomaterials (e.g., nanoscale iron oxides) may have more positive effects (e.g., the release fixed iron for biological utilization) [16, 17].

1.2 Nanoscale iron oxide occurrence and applications

Nanoscale iron oxides are ubiquitous phases encountered in nature [18] including the lithosphere, hydrosphere, and the atmosphere. Evidence of their existence has been discovered in coatings on sand in coastal plains [19], in glacial sediments [20], in certain marine sediments [21], and in atmospheric aerosols [22, 23]. Natural formation of nanoscale iron oxides can occur by various mechanisms including weathering of larger mineral phases, in highly acidic regimes (i.e. elevated concentrations of dissolved iron)

such as acid mine drainage [24, 25], or via oxidation of ferrous iron [Fe(II)] and subsequent precipitation of ferric iron [Fe(III)] on mineral surfaces [26]. Additionally, nanoparticle formation of iron oxides can occur due to microbial oxidation of iron bearing constituents [27]. Their presence in nature is well-documented, yet their role as reactive entities in most natural systems and the magnitude of their contribution to iron redox cycling remains the subject of ongoing investigation.

Beyond natural systems, iron oxides are also versatile materials for a range of applications. Iron oxides are utilized in a array of materials due to the ability to tune their chemical composition, size, electronic structure, optical properties, and crystallinity [24]. The popularity of iron oxides, including nanoscale iron oxides, is derived in part because they are inexpensive materials that exhibit desirable qualities for engineered applications. For example, magnetic iron oxide nanoparticles can be used in biomedical procedures such as magnetic resonance imaging and drug delivery [28], and they can also be functionalized and incorporated into biosensors [29]. In addition, small sectors of energy research are focused on the application of doped iron oxides, which are exploited for their optical properties, and used as photo-catalysts for water oxidation [30].

1.3 Importance of nanoscale iron oxide dissolution

In general, naturally occurring iron oxides are the major source of fixed iron in the environment, with dissolution of Fe from the oxide lattice representing a key source of soluble iron for biological and chemical processes. For instance, Beller et al. [31] demonstrated that the addition of iron oxides to microcosms of Fe-limited anoxic river water promoted degradation of organic pollutants by microbial mediated redox reactions involving sulfur species and iron. At a larger, global scale, Boyd et al. [32] demonstrated that iron fertilization stimulated phytoplankton growth in Fe-limited portions of the polar Southern Ocean, demonstrating its critical role as a limiting nutrient in primary biological productivity. Accordingly, Ridgwell [33] has suggested that the availability of Fe plays a

key role in biogeochemical processes that may affect CO_2 sequestration in the oceans [34].

1.3.1 Iron oxide dissolution processes. Under most environmentally relevant conditions (i.e., neutral pH) the solubility of iron oxides is limited. For example, the solubility of goethite and hematite will produce approximately $10^{-5.8}$ to $10^{-10.9}$ μM of total Fe at pH 7 [35, 36], indicative of the range of concentrations likely to be encountered in natural waters containing such oxides. While solubility of iron oxide nanoparticles may differ from their larger counterparts [37, 38], their overall solubility at environmentally relevant conditions is still relatively limited. Trolard and Tardy [39] demonstrated that while the solubility of goethite increased 250-fold when crystal size was decreased from 100 nm to 10 nm, dissolved iron was only measured to be 1.4 $x10^{-4}$ μM at pH 7 for the 10 nm goethite particles. In addition to size, iron oxide crystallinity is also believed to play an important role in the release of iron at the lattice-solution interface. For example, amorphous iron oxides such as ferrihydrite have weaker bonds holding Fe in the lattice and thus dissolution is typically greater for the less crystalline iron oxides [40].
Several natural dissolution routes exist that help to circumvent the lack of inherent solubility of mineral phases and are summarized in Table 1-1. These dissolution processes help to increase the amount of Fe solubilized from the iron oxide surface and available for various aqueous processes.

1.3.1.1 Proton-promoted dissolution. One of the more simplistic forms of dissolution involves the non-reductive dissolution of mineral phases under acidic conditions known as proton-promoted dissolution [41]. Under this dissolution process, protons adsorb to surface hydroxyl groups. The adsorption of protons is thought to destabilize the Fe-O bond by polarization, thus enabling dissolution of Fe from the solid matrix [24]. The steps for dissolution of an Fe(III) (hydr)oxide are shown with Eq. 1-1, where "‖" represents surface bound Fe(III) [24, 42].

$$\equiv FeOOH + nH^+ \leftrightarrow [\equiv Fe(OH)_{3-n}]^{n+} \rightarrow Fe(III)_{aq} + (n-1)H_2O \quad (1\text{-}1)$$

Detachment of Fe(III) from the surface is considered to be the rate limiting step of the dissolution process, and the rate (R) of proton promoted dissolution is often described as in Eq. 1-2 [24]

$$R = \partial[Fe(III)]/\partial t = k_H[H^+]^n \quad (1\text{-}2)$$

where *n* is the reaction order with respect to proton concentration, which has been shown to be anywhere from 0 to 1. In Eq. 1-2, k_H is the rate constant for proton-promoted dissolution.

1.3.1.2 Ligand-promoted dissolution. A ligand, or a molecule that binds to a metal atom, can also promote non-reductive dissolution of iron oxides. Ligand-promoted dissolution can be performed with model ligands, such as oxalate and malonate, which are known to form complexes with two bonds to a central metal atom (i.e., bidentate ligand), or succinate, which is a unidentate ligand [43]. Naturally occurring ligands such as siderophores [44] and natural organic matter [45] can also promote dissolution of mineral phases in the environment. Zhang et al. [46] demonstrated the rate of Fe(III) release from the oxide surface is dependent on both ligand surface concentration (L_s) and proton concentration as shown in Eq. 1-3

$$R = \partial[Fe(III)]/\partial t = k_L[L_s]^m[H^+]^n \quad (1\text{-}3)$$

where k_L is the rate constant for ligand-promoted dissolution and *m* and *n* are reaction orders for oxalate and protons, respectively. Protons help facilitate dissolution by weakening the Fe-O bond and *n* has been shown to be between 0-1 [24]. Similar to proton promoted dissolution, the release of Fe(III) from the surface is considered to be the rate limiting step [46].

1.3.1.3 Thermal (dark) reductive dissolution. Reductive dissolution, unlike non-reductive dissolution, involves the transfer of an electron to the surface Fe(III) atom, which then reduces to Fe(II) [24]. Abiotic reductants in natural systems such as H_2S [47]

and quinone moieties incorporated into larger marcromolecules (i.e., NOM) [48] may play a role in reducing surface iron and promoted dissolution [49]. Additionally, Fe(II) itself promotes reductive dissolution of structural Fe(III) [50]. Furthermore, biologically mediated reduction driven by iron-reducing bacteria (e.g., *Shewanella alga*) can promote iron dissolution in natural systems [51, 52]. Model reducing ligands such as ascorbate have been extensively studied for mineral dissolution rates [40, 53, 54]. Similar to the non-reductive dissolution cases, Fe(II) dissolution depends on both the concentration of adsorbed reductant (i.e., ascorbate) and proton concentrations (see Eq. 1-3). Reduction of surface Fe(III) atom to Fe(II) can help destabilize surface Fe, due to charge loss and inherent differences in the size associated with Fe(II) (0.078 nm) and Fe(III) (0.064 nm) atoms [24]. Again, the rate limiting step is thought to be detachment from the surface [42].

1.3.1.4 Photoreductive dissolution. Equivalent to the net result of thermal (dark) reductive dissolution, photoreductive dissolution is an important process for labile Fe production in sunlit systems including surface water and aerosol. Natural chromophores that bind to the iron oxide surface such as NOM can mediate photoreductive dissolution [48]. Previous work [55, 56] has demonstrated photoreductive dissolution of Fe(III) with the model chromophore and bidentate ligand, oxalate. Adsorption of oxalate onto surface Fe(III) produces an efficient chromophore that upon irradiation and results in ligand-to-metal charge transfer from photon-excited oxalate to Fe(III). This charge transfer processes results in the reduction of Fe(III) to Fe(II), whereas the oxidation of oxalate can produce transient radicals that may also participate in redox processes on the oxide surface. As with all other dissolution processes, surface Fe(II) release is believed to be the final and rate-limiting step resulting in labile Fe formation via photoreduction.

1.3.2 Size-dependent reactivity of nanoscale iron oxides. Recent evidence suggests each of these dissolution mechanisms for iron oxides is influenced by primary particle size. Such reports of enhanced dissolution reactivity may be partially attributed to surface area differences between two distinct sizes of iron oxide particles. As such, reactivity rates measured between two different sizes of the same iron oxide phase can be normalized by mass or by surface area measurements [57-59]. When comparing surface area normalization, metrics of reactivity (e.g., dissolution rates) can still be several-fold greater for nanoparticle iron oxides relative to their larger analogs. These instances where differences in reactivity cannot be rationalized solely by differences in available surface area are indicative of behavior that is dependent on particle size.

Enhancements in reactivity can be particularly high for nanoparticles with characteristic dimensions equal to or less than 10 nm, a cut off below which most reports of size-dependent activity is observed for metal and metal oxide nanoparticles [15]. For example, Anschutz and Penn [60] noted that 4 nm six-line ferrihydrite showed surface area normalized reactivity of up to 20 times greater than 6 nm, six-line ferrihydrite. They suggested that enhanced reactivity was generally attributed to increasing surface energy with decreasing particle size. Cwiertny et al. [59] demonstrated that nanorod goethite, with widths below 10 nm, exhibited greater dissolution rates per unit mass than larger scale goethite (so-called microrods) when exposed to oxalate. Even though the goethite nanorods had less oxalate adsorbed per unit surface area, surface-area-normalized dissolution rates were ~4 times greater for nanorods relative to microrod goethite. They proposed that the higher reactivity for the goethite nanorods was due in part to differences in the density of surface hydroxyl groups, often assumed to be critical surface reactive sites [24], and the relative amounts of specific reactive crystal faces on nanorods compared to their larger analogs. Recently, work by Echigo et al. [61] demonstrated that 7 nm hematite particles exhibited 2-fold greater surface area normalized rates of

reductive dissolution by ascorbic acid (pH 3.35) relative to larger 30 nm hematite. They attributed the enhanced rates of dissolution observed for 7 nm hematite particles to the presence of monodispersed particles in 7 nm suspensions, which they proposed were highly reactive and dissolved first, thus causing an initially greater rate of dissolution for the smaller hematite particles. In contrast, larger 30 nm hematite particles were subject to specific dissolution at crystal imperfections and edges [62].

Despite such observations, definitive evidence as to the underlying cause of size-dependent iron oxide behavior, including their dissolution activity, remains limited. Notably, most studies to date demonstrating enhanced dissolution of nanoscale iron oxides have been conducted in moderate to highly acidic media (pH $\leq$ 3.75) [59-61, 63-65] not relevant to circumneutral pH surface waters and have limited their reactivity studies to single dissolution mechanisms (e.g. proton-promoted, reductive, photoreductive, or ligand promoted). This makes it difficult to predict whether prior reports of size-dependent iron oxide dissolution are a general phenomenon observable across a broad range of mechanisms and aqueous conditions, or simply unique behavior limited to highly specific system conditions. Understanding the broad applicability of size-dependent reactivity may enhance predictability and accuracy of models dependent on labile iron existence in the environment.

We also note that accurately quantifying the influence of surface area can be confounded by our abilities to accurately measure this property of nanomaterials. Indeed, surface area measurements typically depend on the procedure used [66]. For example, common methods for surface area measurements include gas adsorption [67], adsorption of a model solute under precise solution conditions [68, 69], and geometric surface area estimations [70]. Brunaer, Emmett, and Teller (BET) gas adsorption isotherms [67] is perhaps the most commonly utilized approach for measurement of specific surface area, but it is limited to dry nanopowders. Thus, its applicability to particles in aqueous

suspensions remains questionable, particularly for those systems in which nanoparticles are extensively aggregated.

1.4 Aggregation and size-dependent trends

While size-dependent reactivity has been observed in lab-bench scale experiments [60] and to some extent in natural environments [21], reactivity is dependent on available surface area. Aggregation (the coalesce of primary particles into clusters or colloids) of nanoparticles in suspension is a well-known phenomenon, yet the extent to which aggregation affects reactivity is not yet clearly understood (Figure 1-1). Numerous solution phase variables including pH and ionic strength are recognized driving forces for iron oxide aggregation [71-74]. The presence of co-solutes such as organic matter [75, 76] can also effect the surface charge on iron oxides, which may either stabilize or destabilize iron oxide suspensions. In addition to these solution phase drivers, irreversible aggregation may also be inherent when drying iron oxides [77, 78], as is common practice in laboratory oxide preparation for use in reactivity studies. All these aggregation mechanisms have the potential to change aggregate structure and density, which may in turn affect the inherent size-dependent reactivity of the nanoparticles.

Recent investigations [78-82] support the prevailing wisdom that aggregation of iron oxide nanoparticles will be an important consideration in their reactivity. It is widely recognized that changes in morphology and porosity [24] induced by aggregation, which likely consumes the amount of available surface area in suspension, limit iron oxide interfacial reactivity. Gilbert et al. [78] examined changes in Cu(II) uptake onto ferric iron oxyhydroxide nanoparticles in response to different aggregation mechanisms including pH, ionic strength, freezing, and drying. They concluded that aggregation mechanisms can have a large impact on metal uptake, with drying resulting in the most compact aggregates that exhibited limited Cu(II) uptake compared to other aggregation mechanisms (i.e., pH, ionic strength, and freezing). Interestingly, they noted that the

more compact aggregate structures formed by drying also minimized desorption of Cu(II) possibly due to pore constriction and tortuosity. Consistent with such a scenario, Hofmann et al. [83] also observed that drying 2-line ferrihydrite aggregates increased aggregate density which resulted in 25% reduction in aggregate porosity and smaller pore sizes.

Dissolution reactivity has also been shown to be affected by nanoparticle aggregation. Under proton promoted dissolution and ionic strength induced aggregation, Rubensinghege et al. [64] demonstrated that the dissolution activity of nanorod goethite was quenched via the formation of dense aggregates at high ionic strengths. Similarly, Bligh and Waite [82] proposed that aggregation during aging (i.e., aggregates formed by particle-particle or cluster-cluster collisions by Brownian motion) in seawater (ionic strength ~0.7 M) was responsible for observed loss in dissolution (i.e. ligand promoted and reductive dissolution) activity for amorphous iron oxides generated from Fe(II) and Fe(III). Raiswell et al. [77] observed decreases in Fe extraction via ascorbic acid from ferrihydrite due to aggregation. They suggested that de-watering techniques had the greatest impact on dissolution due to the density of aggregates formed and the presence of nanopores, which may limit solute transport into the aggregate and iron transport from the aggregate interstices.

As previous discussed, a particularly challenging consequence of aggregation is the uncertainty it introduces into attempts to quantify size-dependent reactivity trends for nanoparticles. For example, He et al. [81] established that smaller (~ 12 nm) nanoparticles aggregate more extensively under the same pH and ionic conditions when compared to their larger counterparts (~ 65 nm). Such differences in aggregation complicate attempts to evaluate size-dependent trends via surface area normalization of reactivity metrics, as is commonly used for nanomaterials. In particular, numerous questions persist as to how reactivity of iron oxide nanoparticles changes in response to

aggregation state (e.g. aggregate size, structure, and density), as well as how the reactivity of aggregates is influenced by the size of the primary nanoparticle from which they are constructed.

Aggregation effects on nanoparticle reactivity may be process dependent phenomenon. As mentioned earlier, work has shown that aggregation of nanoparticles can limit metal uptake [78] and proton promoted (non-reductive) dissolution [64]. However, Cwiertny et al. [84] observed that increased aggregation associated with greater particle concentrations of nanogoethite had no impact on the amount of Fe(II) adsorbed per gram of iron oxide. The process of Fe(II) uptake onto an iron oxide surface is a distinct example of an interfacial redox reaction, and has been observed by many others [50, 85-87]. Thus, it remains largely unclear if aggregation effects are observable across all reactivity mechanisms associated with iron oxides.

1.5 Iron oxide nanoparticles in surface water

While it is widely believed that iron oxide nanoparticles play a prominent role in iron oxide redox cycling, there remains little laboratory or field-scale evidence for their contributions to processes other than Fe solubilization. One overlooked process for which iron oxide nanoparticles may play a key role is the photochemical Fenton reaction, a well-recognized process in sunlit surface waters critical to production of reactive oxygen species (ROS). Specifically, the Fenton reaction (Eq. 1-4) generates highly potent hydroxyl radical (•OH) via the reduction of hydrogen peroxide by Fe(II).

$$Fe(II) + H_2O_2 \rightarrow Fe(III) + OH^- + \bullet OH \qquad (1\text{-}4)$$

In sunlit surface waters, light can initiate heterogenous Fenton-like reactions by reducing colloidal Fe(III) to soluble Fe(II), most often through adsorbed ligands acting as chromophores that drive ligand-to-metal charge transfer [56]. The heterogenous Fenton reaction involves a complicated series of reactions to ultimately lead to •OH production [88, 89]. After initial sorption of a chromophore to the oxide surface, photon absorption

by the chromophore (C) and subsequent charge transfer leads to the formation of surface Fe(II) as shown in Eq. 1-5.

$$\equiv\text{Fe(III)-C} \xrightarrow{\lambda} \equiv\text{Fe(II)-C} \qquad (1\text{-}5)$$

The newly formed surface Fe(II) is destabilized, by the larger atomic radius and weakening of the Fe-O bond by protonation and ligand adsorption [24]. Parallel dissolution of the surface Fe(III) is also possible (Eq. 1-6)

$$\equiv\text{Fe(III)-C} \rightarrow \text{Fe(III)-C(aq)} \qquad (1\text{-}6)$$

Simultaneously, absorption of photons by photoactive natural organic matter (NOM*) yields H_2O_2 from the disproportionation of superoxide anion (Eq. 1-7 and 1-8) [89-91].

$$\text{NOM*} + O_2 \xrightarrow{\lambda} \text{NOM(oxidized)} + HO_2/O_2^{\bullet-} \qquad (1\text{-}7)$$

$$2HO_2/O_2^{\bullet-} \rightarrow H_2O_2 + O_2 \qquad (1\text{-}8)$$

Simultaneous reactions involving solubilized Fe(II) and Fe(III) can also occur, one being the Fenton reaction (Eq. 1-4) which leads to the formation of •OH. Additional reactions that can occur were detailed by Kwan and Voelker [88] and are summarized herein (Eq. 1-9 – 1- 12).

$$\text{Fe(III)} + H_2O_2 \rightarrow \text{Fe (II)} + HO_2/O_2^{\bullet-} \qquad (1\text{-}9)$$

$$\text{Fe(III)} + HO_2/O_2^{\bullet-} \rightarrow \text{Fe (II)} + O_2 \qquad (1\text{-}10)$$

$$\text{Fe(II)} + \bullet\text{OH} \rightarrow \text{Fe (III)} + OH^- \qquad (1\text{-}11)$$

$$\text{Fe(II)} + HO_2/O_2^{\bullet-} \rightarrow \text{Fe (III)} + HO_2 \qquad (1\text{-}12)$$

The reactions shown with Eq. 1-4 and Eq. 1-9 through 1-12 illustrate a Fenton-like chain reaction where Fe(II) and Fe(III) can be perpetually regenerated via photo-redox cycling. While complex, this so-called heterogenous photo-Fenton reaction has been implicated in pollutant degradation [92, 93], bacterial kill [94], and viral inactivation [95] in circumneutral waters.

Iron dependent processes such as the Fenton reaction may be disproportionately influenced by the size-dependent nanoscale iron oxide reactivity. It may be contended

that nanoscale iron oxides, which evidence suggests are more prone to (photo)reductive dissolution per unit mass relative to their larger counterparts [59, 61] should enhance •OH formation. This enhancement in a potent ROS could in turn produce greater pollutant degradation and bacteria kill in surface water bodies.

1.6 Overview and thesis organization

The objective of this work is to elucidate the size-dependent reactivity of iron oxides. Using hematite as a model, work herein explores its size-dependent reactivity as a function of dissolution mechanism, solution conditions (e.g., pH) and suspension aggregation state. Hematite is among the most thermodynamically stable iron oxides, it is naturally abundant, and expected to play important roles in a variety of natural and engineered systems. Focusing on laboratory synthesized hematite with primary particle sizes of 8 nm and 40 nm, size-dependent trends in interfacial reactivity will be quantified and the implications of such size-dependent reactivity will be assessed in model surface water reactions in which iron redox cycling is critical to pollutant transformation reactions.

This thesis contains three chapters of original research investigating the size-dependent reactivity of hematite nanoparticles. The first original research chapter, Chapter 2, explores fundamental dissolution mechanisms of 8 and 40 nm hematite nanoparticles. Dissolution reactivity was examined using proton-promoted, ligand-promoted, thermal reductive, and photoreductive dissolution mechanisms. Importantly, this work is the first to demonstrate that size-dependent hematite nanoparticle reactivity can extend into circumneutral and neutral pH values via thermal reductive and photoreductive dissolution, thus making size-dependent reactivity a feasible variable in environmentally relevant systems.

A key variable in all nanomaterial suspensions is the aggregation effect. Chapter 3 explores how aggregation affects size-dependent reactivity toward thermal reductive

dissolution by ascorbic acid. Previous work has shown aggregation can lead to limitations in reactivity [64, 82], thus rending size-dependent enhancement irrelevant. This work used gravitational fractionation and ionic strength induced aggregation to determine the effects of both the size of the aggregate and the overall aggregation state, and how each impact size-dependent reactivity. Results and environmental implications are discussed within.

Chapter 4 applies knowledge gained from the previous chapters regarding size-dependent reactivity of 8 and 40 nm hematite particles to surface water process critical to pollutant fate. Specifically, work in that chapter examines how dissolved organic matter mediated photo-generation of Fe(II) affects the photo-Fenton reaction in model surface water systems. The generation of H_2O_2 from illuminated model humic acids and resultant production of hydroxyl radical from reaction with Fe(II) were quantified using the simple organic probe, phenol. Prior work [89, 96] has demonstrated that Fenton reactions in neutral waters can occur from natural organic matter and labile ferrous iron. However, no work has demonstrated that sources of Fe(II), specifically, naturally abundant hematite, can contribute to this reaction based on size-dependent reactivity of the given iron oxides.

1.7 Expected outcomes

Results from this research will provide important information regarding nanohematite reactivity and their ability to contribute to both environmental and engineered systems. Hematite is a naturally occurring semi-conductor [24] with implications for natural [26] reduction-oxidation (redox) reactions as well as those specifically engineered [97] for useful purposes. Broadly, knowledge gained from this work investigating size-dependent roles of redox active parameters may help improve efficacy and efficiency of engineered processes that utilize hematite[98].

Specifically, the work herein seeks to use measurements of iron production rates as a simple means to understanding relative rates of reactivity between the two sizes of

hematite nanoparticles. Investigations establishing both redox and non-redox reactivity across a range of solution chemistries and dissolution mechanisms is merited (Chapter 1). By exploring a large range of solution pH, simple empirical models can be used to describe size-dependent reactivity within a given mechanism of dissolution. Work that will be specifically applicable to grasping size-dependent reactivity in solutions chemistries ranging from highly acidic, which may occur in unique locations of the environment (i.e., acid mine drainage and atmospheric water droplets) to more neutral systems which may also be seen in nature (i.e., surface and ground water) or even engineered applications (i.e., wastewater energy conversion).

Additionally, investigating aggregation effects (Chapter 2), which are largely overlooked in the literature, will allow for a more consistent interpretation of environmental and engineered systems where nanomaterial suspensions are present. As of now, common techniques of comparing size-dependent reactivity are through mass or surface-area normalization of the particles. Surface area normalization is often based on of measurements taken under one condition (i.e., BET measurements on dry powders), while reactivity is measured under another condition (i.e., in suspension). Furthermore, aggregation itself is not universal. Different solution chemistries or preparation techniques may all cause aggregation, but each technique itself can inherently change aggregate structure or morphology. Thus, normalizations may fall short when trying to encompass true reactivity of each nanoparticle investigated. This work will establish how aggregation affects size-dependent reactivity associated with primary nanoparticles across a range of aggregate sizes (i.e., aggregates made up of primary nanoparticles) under a range of aggregation methods and dissolution mechanisms. From this, the intent of this work is to gain a thorough understanding of aggregation methods and aggregate sizes as applied to specific reactivity that may be encountered in natural settings (i.e.,

reductive and non-reductive dissolution) and commercial systems (i.e., redox active capabilities)

A comprehensive understanding of size-dependent reactivity through a variety of mechanisms, under a range of solution chemistries, and across aggregation sizes and techniques will allow for reactivity predictability in real world systems. As such, work in Chapter 3 seeks to investigate the relevance of size-dependent reactivity in a model environmental system with a complex set of variables, the photo-Fenton reaction. Applying all knowledge gained from initial fundamental size-dependent reactivity investigations will apply to this more complicated system, including solute uptake and subsequent surface dependent reductive dissolution. Results will be directly applicable to iron oxide rich surface waters. Furthermore, understanding size-dependent reactivity in more complex systems will allow for future modeling and engineered application of iron oxide reactivity. Collectively, the results garnered from this complete work will be applicable to modeling environmental systems where nanohematite may play a dominant role in reactivity as well as new and emerging engineered systems where size effects are playing a considerable role in reactivity.

Table 1-1. Common iron oxide dissolution mechanisms and species involved.

Dissolution mechanism	Dissolution process	Common species involved
Non-Reductive	Proton promoted	H^+ (i.e. HCl)
	Non-reductive ligand promoted	Oxalate, siderophores
Reductive	Reductive ligand	Ascorbate, hydroquinone
	Photoreductive	Natural organic matter (NOM)

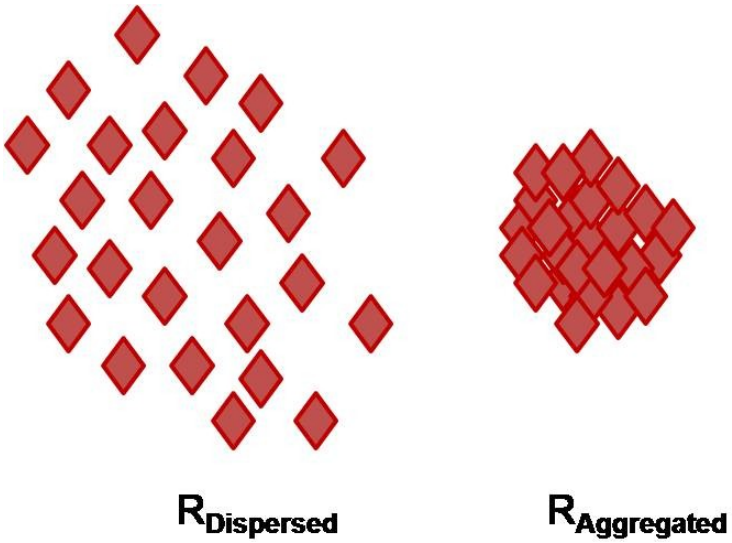

Figure 1-1. Dispersed particles (left) compared to the same number of particles aggregated (right). Aggregation may affect the rate of reactivity (R) associated with either dispersed particles or tightly aggregated particles.

CHAPTER 2
DISSOLUTION OF HEMATITE NANOPARTICLE AGGREGATES: INFLUENCE OF PRIMARY PARTICLE SIZE, DISSOLUTION MECHANISM AND SOLUTION pH

2.1 Abstract[a]

The size-dependent dissolution of nanoscale hematite (8 and 40 nm α-Fe_2O_3) was examined across a broad range of pH (pH 1-7) and mechanisms including proton- and ligand- (oxalate-) promoted dissolution and dark (ascorbic acid) and photochemical (oxalate) reductive dissolution. Empirical relationships between dissolution rate and pH reveal that suspensions of 8 nm hematite exhibit between 3.3-to-10-fold greater reactivity per unit mass than suspensions of 40 nm particles across all dissolution modes and pH, including circumneutral. Complementary suspension characterization (i.e., sedimentation studies and dynamic light scattering) indicates extensive aggregation, with steady-state aggregate sizes increasing with pH but being roughly equivalent for both primary particles. Thus, while the reactivity difference between 8 and 40 nm suspensions is generally greater than expected from specific surface areas measured via N_2-BET or estimated from primary particle geometry, loss of reactive surface area during aggregation limits the certainty of such comparisons. We propose that the relative reactivity of 8 and 40 nm hematite suspensions is best explained by differences in the fraction of aggregate surface area that is reactive. This scenario is consistent with TEM images revealing uniform dissolution of aggregated 8 nm particles whereas 40 nm particles within aggregates undergo preferential etching at edges and structural defects. Ultimately, we show that comparably sized hematite aggregates can exhibit vastly different dissolution activity depending on the nature of the primary nanoparticles from

[a] An abbreviated version of this chapter has been published: Lanzl, C. A.; Baltrusaitis, J.; Cwiertny, D. M., Dissolution of Hematite Nanoparticle Aggregates: Influence of Primary Particle Size, Dissolution Mechanism, and Solution pH. *Langmuir* 2012, 28, (45), 15797-15808.

which they are constructed, a result with wide-ranging implications for iron redox cycling.

2.2 Introduction

Mounting experimental evidence suggests that nanoparticles of iron (oxyhydr)oxide (hereafter referred to iron oxides) exhibit dissolution rates far greater than those of their larger analogues [59-61, 63-65, 99], behavior also reported for nanoparticles of metals (e.g., Ag) [100], other metal oxides (e.g., ZnO) [101, 102] and metal sulfides (e.g., PbS) [103]. For example, Anschutz and Penn [60] demonstrated that surface-area-normalized rate constants for the reductive dissolution of goethite (α-FeOOH) nanorods by hydroquinone were 2-fold greater than rate constants measured for micron-sized goethite (i.e., microrods). In a later study also with goethite, Rubasinghege et al. [64] observed even greater enhancements for proton-promoted dissolution (pH 2) of nanorods relative to microrods. Unique to nanoscale iron oxides is their ubiquity in the natural environment [19, 21, 104, 105], such that these findings of size-dependent dissolution have broad implications for iron bioavailability, elemental cycling, and pollutant fate in a range of natural systems. For instance, focus on nanogoethite reactivity is motivated in part by reports [21] that it represents the dominant reactive iron oxide phase in lake and marine sediments. Further, there is growing appreciation for the role that iron oxide nanoparticles, either initially present in mineral dust aerosol or formed during aerosol atmospheric processing, plays in the release of bioavailable iron after deposition in the open ocean (see [106] and references therein).

The fundamental cause of these [59-61, 63-65, 99] and other [57, 58, 104, 107, 108] reports of size-dependent iron oxide behavior remains complicated by the myriad factors recognized to influence the microscopic and macroscopic behavior of nanomaterials [109]. For instance, differences in shape, surface structure, and inherent defects, all of which can vary with primary particle size [110], can influence iron oxide dissolution [41, 111, 112]. It is certainly possible, therefore, that nanoscale oxides simply

possess types and distributions of surface sites unique relative to larger phases, which may explain reported differences in their macroscopic reactivity (e.g., measured dissolution rates). Moreover, evidence for such a scenario exists in the literature. Molecular dynamics calculations by Rustad and Felmy [113] indicated that the surfaces of acicular goethite nanoparticles can accumulate charge at sites distinct from those on larger goethite slabs. Adsorption studies by Villalobos [114] suggested that the surface site density of goethite may change with decreasing particle size. In previous work [59], ATR-FTIR revealed a greater density of surface hydroxyl groups on nanorods relative to microrods, and we proposed that this difference was primarily responsible for size-dependent trends we measured for ligand (oxalate)-promoted dissolution.

Despite such observations, definitive evidence as to the underlying cause of size-dependent iron oxide behavior, including their dissolution activity, remains limited. This makes it difficult to predict whether prior reports of size-dependent iron oxide dissolution are a general phenomenon observable across a broad range of mechanisms and aqueous conditions, or simply unique behavior limited to highly specific system conditions. Notably, most studies to date demonstrating enhanced dissolution of nanoscale iron oxides have been conducted in moderate to highly acidic media ($pH \leq 3.75$) [59-61, 63-65, 99] not relevant to circumneutral pH surface waters and have limited their reactivity studies to a single dissolution mechanism (e.g., proton-promoted, reductive, photoreductive, or ligand-promoted).

A major hurdle to a more definitive understanding of nanoscale iron oxide dissolution is their tendency to extensively aggregate in most aqueous systems. While reactive surface area of freely dispersed nanoparticles can often be approximated from analysis of dry powders (e.g., specific surface areas calculated from TEM particle sizing or BET isotherm measurements), the reactive portion of suspended aggregates of nanoparticles is far more challenging to quantify. Although its influence on dissolution of nanoscale iron oxides has not been fully explored, aggregation is generally assumed to

limit the rate and extent of most interfacial processes (e.g., sorption and electron transfer [78, 84, 115, 116]) via loss of reactive surface area as particles coalesce. Consistent with this scenario, Bligh et al. [82] recently examined the reactivity of amorphous ferric oxides (AFO) generated from Fe(II) and Fe(III) in seawater (pH 8.1), concluding that loss of reactive surface area via aggregation is responsible for observed decreases in dissolution rate as a function of AFO aging. Thus, a critical question regarding the dissolution of nanoscale iron oxides, particularly in circumneutral pH waters, relates to what fraction of the primary particle surface is reactive, and how this fraction changes in response to system conditions that transform freely suspended nanoparticles into densely packed aggregates. Much remains to be discovered in this regard as most prior reports of size-dependent dissolution [59-61, 63-65, 99] have utilized acidic media likely to minimize aggregation.

In this work, we examine the dissolution of two sizes of hematite (α-Fe_2O_3) nanoparticles (8 and 40 nm) over a range of pH values and across a spectrum of dissolution mechanisms. Hematite is naturally abundant, expected to play a prominent role in the reactivity of iron oxides in soils, sediments and aerosol, and its size-dependent dissolution behavior has not been as extensively investigated as other phases (e.g., goethite and ferrihydrite). Yet it is an ideal system to consider because of the extensive body of literature on the dissolution of natural and synthetic hematite samples (see Schwertmann and Cornell ([24]) and references therein), thereby providing a baseline for comparing our observations for hematite nanoparticles to established behavior most often developed with larger particles.

We employ a complementary approach linking the stability of hematite suspensions (i.e., the extent to which hematite particles remain freely suspended in solution) to their dissolution activity. The aggregation state of each size of hematite was evaluated using dynamic light scattering (DLS) and sedimentation studies under highly acidic (pH 1) to circumneutral (pH 7) pH conditions. In parallel, we measured

dissolution rates in suspensions of each particle size over the same pH range. Specific dissolution processes investigated include proton-promoted dissolution, ligand-promoted dissolution with oxalate, reductive dissolution via ascorbic acid, and photochemical reductive dissolution in irradiated suspensions of oxalate. By considering a range of dissolution processes and conditions, we expand upon recent work by Echigo et al. [61] that demonstrated size-dependent trends in the reductive dissolution of two similarly sized hematite particles (7 and 30 nm) by ascorbic acid at pH 3.35, aiming to determine the generality of this result. Further, by using pH as a master variable, we construct empirical relationships between dissolution rates and suspension pH for both sizes of hematite, which will allow any size-dependent trends in their interfacial reactivity to be more quantitatively predicted across different aquatic systems. Notably, the range of pH values considered (up to pH 7 in some instances) allows us to explicitly address whether size-dependent trends in nanoparticle activity previously observed in acidic media can be reasonably extrapolated to more environmentally relevant, circumneutral pH values. Finally, via observed changes in suspension stability over the pH range investigated, we address whether the macroscopic reactivity of hematite aggregates depends on the size of primary particle from which they are constructed.

2.3 Experimental methods

2.3.1 Reagents. All chemicals were of reagent grade or better. Hematite was synthesized from ferric nitrate nonahydrate (Fisher; 100%). Sodium oxalate (Sigma Aldrich, 99%), L-ascorbic acid (Sigma Aldrich; ≥99%), and concentrated hydrochloric acid (Fisher; 34-37%, trace metal grade) were used in dissolution experiments. Concentrations of dissolved ferrous iron [Fe(II)] were determined colorimetrically with 1,10-phenanthroline (Sigma Aldrich; ≥99%), a buffer from ammonium acetate ($C_2H_7NO_2$; Sigma Aldrich; ≥98%) and glacial acetic acid (Acros Organics; 99.8%), while ammonium fluoride (Fisher; 99.5%) was used to limit analytical interference from ferric iron [Fe(III)]. Measurements of total dissolved iron concentrations used the reductant

hydrochloric hydroxylamine (Sigma Aldrich; 99%). All solutions were prepared in deionized water (Millipore, Q-Grad 2). O_2-free experiments (i.e., reductive dissolution) used solutions previously sparged with N_2 gas (1 h/L) prior to experimentation and were conducted within an anaerobic chamber (95 % N_2, 5 % H_2, Coy Laboratory Products).

2.3.2 Hematite synthesis. Hematite nanoparticles were prepared by the methods of Sorum [117] and Schwertmann and Cornell [118]. The method of Sorum [117], known to yield nanoparticles ~10 nm in diameter [118], involves the drop-wise addition (0.5 mL/min via peristaltic pump) of 1 M ferric nitrate into boiling water mixed via a magnetic stirrer. After cooling the nanoparticle suspension was placed in dialysis bags, and the bags were submerged in water that was changed 3-4 daily over 4 d. The suspension was then air dried, and dried particles were ground by mortar and pestle and passed through a 53 μm sieve before use. The method of Schwertmann and Cornell [118] is known to yield larger particles on the order of 30-40 nm. A mixture of 0.02 M ferric nitrate in 0.002 M $HNO_3$was baked for 7 d at 98°C in a 1 L HDPE Nalgene bottle. Particles were separated via centrifugation and washed three times with deionized water prior to freeze-drying. Dried particles were then processed as described previously. We note that a subset of reactivity experiments, some of which will be the focus of a future investigation, demonstrated that the relative reactivity of hematite suspensions prepared by these methods was largely insensitive to specifics of their processing and handling during synthesis. Specifically, quality control studies evaluating the impact of dialysis versus centrifugation for purification and the method of drying (freeze-drying, air-drying, or working with suspensions without any drying) suggest that the relative trends in hematite reactivity reported subsequently are invariant to such process consideration.

2.3.3 Characterization of hematite powders. Each synthesis product was characterized via powder X-ray diffraction (XRD) using a Rigaku MiniFlex II X-ray diffractometer with a Co source. Specific surface areas were measured using a Quantachrome BET Nova 4200e automated surface area analyzer. Samples were

outgassed overnight at110°C prior to analysis via a seven point N_2 BET adsorption isotherm. The size and morphology of hematite samples were determined from transmission electron microscopy (TEM). TEM images were collected on a high resolution JEOL 2100F transmission electron microscope operating in bright field mode at 200 kV. For TEM samples were prepared through the addition of a drop of dilute hematite suspension onto a holey carbon Cu grid. Average particle sizes were determined from measurement of at least 100 particles in the software program Image J.

2.3.4 Characterization of hematite suspensions. The surface chemistry of suspended hematite aggregates was probed via potentiometric titrations with a 798 Titrino autotitrator (Metrohm). A solution of 25 mM NaCl was sparged with N_2 gas for 1 h to remove any dissolved CO_2 and then used to prepare 4 g/L hematite suspensions. Suspensions were sonicated for 5 min (Bransonic Ultrasonics Corporation, 151OR-DTH, 42 kHz ± 6%) to disperse the particles before titration. The suspensions were once again sparged with N_2 for an additional 10 min to remove any residual CO_2, and the sparging continued throughout the titration. Suspensions were adjusted to a pH value slightly below 4 immediately prior to the addition of sodium hydroxide (0.1 M) at 0.01 mL/min until a suspension pH of 10 was achieved.

The stability of hematite suspensions as a function of pH was examined using sedimentation tests. Suspensions (0.5 g/L) were prepared in deionized water with 25mM NaCl, and the solution pH was adjusted as needed with dilute HCl or NaOH. Once adjusted, pH values were essentially stable during analysis. As a result of HCl concentrations needed to achieve very low pH values (pH 1, 1.5 and 2), the ionic strengths in these suspensions (110 mM, 50 mM, and 30 mM, respectively) were greater than in other systems. All suspensions mixed overnight prior to sedimentation experiments, thereby allowing sufficient time for aggregate sizes to reach steady-state. A portion of suspension was then transferred to a 1 cm quartz cuvette and rates of settling

were measured by the change in light transmittance (λ of 510 nm) as a function of time using a UV/visible spectrophotometer (Thermo Fisher Scientific, Genesys 10S).

Additional information on aggregate size and suspension stability was obtained through dynamic light scattering (DLS) and zeta potential measurements conducted on a ZetaPALS analyzer (Brookhaven Instruments Corporation, Holtsville, NY). Analysis required the aforementioned 0.5 g/L suspensions be diluted to achieve an absorbance of ~0.3 at λ of 246 nm. Dilutions were made with pH adjusted 25 mM NaCl, and suspensions were allowed to equilibrate for several hours prior to analysis, during which time the pH was monitored to ensure there was no drift. Analyses were conducted in triplicate, in which single measurements were collected from three different reactor vessels. All data presented represent averages of these replicate studies.

TEM images were also collected for hematite suspensions (0.5 g/L) after dissolution with either 10 mM ascorbic acid or 1 mM oxalate at pH 2 for 20 h and 13 days (described in more detail below). After the allotted time several drops of suspension were diluted into methanol, and this mixture was subsequently applied drop-wise to a TEM grid. Roughly 20 images were collected for each sample over a range of magnifications and at various locations across the TEM grid. Images presented subsequently are representative of typical images collected for each sample.

2.3.5 Hematite dissolution in the absence of light. Dissolution experiments were conducted at room temperature with 0.5 g/L suspensions of hematite in 25 mM NaCl. Because we anticipated extensive aggregation in our suspensions, the extent of which will vary as a function of hematite mass concentration (in g/L), we decided against conducting our experiments at a constant surface area loading (in m^2/L) as was recently advocated by Barton et al. [58]. Suspensions (30 mL) were prepared in screw cap vials that were covered with Al foil to omit light and mixed end-over-end (Cole Parmer, Roto-Torque) at 60 rpm during experiments. Solution pH was monitored routinely using an Accumet Basic AB15 pH meter with combination pH electrode (Fisher Scientific).

Suspension pH generally varied little over time, but small amounts of dilute HCl or NaOH were added as needed to maintain the pH near its initial value (± 0.05 pH units).

Rates of proton-promoted dissolution were measured at pH 1.0, 1.5 and 2.0. To initiate dissolution, an appropriate mass of hematite was added directly to solutions at each pH prepared from HCl. Ligand-promoted dissolution with sodium oxalate was examined at pH 2.0, 3.0 and 4.0. To initiate dissolution, a small aliquot of sodium oxalate stock solution (prepared daily) was added to hematite suspensions at each pH value, producing an initial oxalate concentration of 1 mM. Rates of reductive dissolution with L-ascorbic acid were measured from pH 2 to 6 via experiments within an anaerobic chamber. Stock solutions of ascorbic acid were prepared daily and deoxygenated via sparging with N_2 prior to use. To initiate dissolution, a small aliquot of ascorbic acid stock solution was added to hematite suspensions prepared at each pH value, producing an initial ascorbic acid concentration of 10 mM.

All experimental systems were sampled periodically over time by removing 1 mL aliquots from well-mixed suspensions so as not to disrupt the solid-to-water ratio of the system. Samples were passed through a 0.2 μm nylon Xpertek filter (P.J. Corbert Associates; Saint Louis, MO). Additional analyses suggested that 0.2 μm filters were sufficient to remove most if not all hematite from suspension. Dissolved iron concentrations measured in the filtrate were statistically equivalent whether the filtrate was analyzed by 1,10-phenantroline immediately or after acidification (to a final concentration ~5 M HCl), which would dissolve any particles that broke through the filter during sampling and in turn be expected to produce larger dissolved iron values. Filtered samples were promptly covered by Al foil to minimize any potential for photochemical reactions prior to analysis of dissolved iron. The concentrations of dissolved ferrous iron [Fe(II)] and total dissolved iron [TOT(Fe) = Fe(II) + Fe(III)] were then determined colorimetrically using 1,10-phenanthroline. The detection limit for this method under

these conditions was 1 μM of Fe(II). All dissolution experiments were conducted in triplicate.

2.3.6 Photoreductive dissolution of hematite. Experiments measuring rates of oxalate-mediated photoreductive dissolution utilized a 1000 W O_3-free Xe arc lamp (Newport Corporation) equipped with a water filter to remove IR radiation and a long pass optical filter that selectively transmitted wavelengths of light greater than 305 nm. Experiments were performed in a custom photoreactor with total volume of ~70 mL. The photoreactor was equipped with a water jacket to maintain 25°C, ports for sample withdrawal and pH measurement, and a removable screw-cap with quartz window. The screw-cap allowed experiments to be conducted in the absence of O_2 when the reactor's contents were sparged and then maintained at an overpressure of N_2. From ferrioxalate actinometery [119, 120] the incident photon flux to the reactor was 1.1 x 10^{-3} einstein s^{-1} m^{-2}, whereas estimated irradiance was approximately 10 W/m^2 ($\lambda \geq 305$ nm).

Photodissolution rates were measured from pH 5 to 7 in 0.5 g/L hematite suspensions with an initial oxalate concentration of 1 mM. Controls were also conducted with hematite in the absence of oxalate. Prior to irradiation, the hematite and oxalate mixture was purged with N_2 for at least 10 minutes, and an overpressure of N_2 was maintained in the photoreactor headspace throughout irradiation to minimize oxidation of Fe(II). Samples were removed via a disposable syringe fitted with Teflon tubing that could be lowered into solution through the sampling port. Samples were passed through a 0.2 μm nylon filter, and 1 mL of filtrate was immediately added to 40 μL of 5 M HCl to preserve Fe(II) for analysis.

2.3.7 Quantifying hematite dissolution rates. For all processes, rates of hematite dissolution were determined from the initially linear portion of plots of Fe(II) (reductive dissolution) or Fe(III) (non-reductive dissolution) concentration over time. Dissolution rates (i.e., d[Fe(II)]/dt or d[Fe(III)]/dt in units of $\mu M \cdot h^{-1}$) were quantified from the slope of best-fit linear regression analyses of concentration versus time data. Replicate

(triplicate) experiments yielded nearly identical dissolved iron concentrations over time, such that a single regression analysis was conducted using the average concentration measured at each sampling point. Reported uncertainties associated with rate data represent the 95% confidence interval for the slope of this linear-regression analysis. In all cases, this procedure yielded rates (and associated uncertainty) that were statistically equivalent to those calculated by averaging the rates measured in each replicate.

2.3.8 Analytical methods. Soluble Fe(II) and TOT(Fe) were measured with 1,10-phenantroline [121, 122]. Samples for TOT(Fe) analysis were first treated with 20 µL of hydroxylamine to reduce soluble Fe(III) to Fe(II). For Fe(II) analysis, a small amount (50 µL) of 0.43 M ammonium fluoride was added to reduce potential interference from Fe(III). For colorimetric analysis, 200 µL of 1 g/L phenanthroline and 200 µL of 100 g/L ammonium acetate buffer were added to samples, which were then allowed to sit in the dark for ~30 min prior to absorbance measurements on a Shimadzu UV-visible spectrophotometer (at λ = 510 nm).

In photoreductive dissolution experiments, the concentration of oxalate was monitored as a function of irradiation time, as well as in dark control systems to measure adsorption. Filtered samples were transferred to an amber 1.5 mL crimp seal autosampler vial, and oxalate concentrations were measured on a 1260 series HPLC (Agilent Technologies) equipped with diode array detector (DAD). The method used a mobile phase of 0.01N H_2SO_4 at a flow rate of 1 mL/min on a Prevail organic acid column (Grace Davison/Discovery Sciences) and an analytical wavelength of 210 nm. Aqueous phase concentrations were determined from standards of sodium oxalate that were prepared in a matrix equivalent to that of the samples. In dark controls, adsorbed oxalate concentrations were determined from the difference in concentration between the initial amount of oxalate and the amount remaining in solution at equilibrium.

2.4 Results and discussion

2.4.1 Characterization of hematite powders. Powder XRD patterns indicated that both products were indeed hematite (Figure 2-1). TEM images revealed the expected primary particle size and morphology for both synthesis products (Figure 2-2a and 2-2c). Sorum's method yielded nanoparticles with pseudo-hexagonal platelet morphology [57, 61], which we approximated to be spherical with an average diameter of 8.1 nm (± 1.6) (values represent the mean and standard deviation from TEM sizing of n = 200 particles). The nanoparticles were comparable in size and morphology to others [57, 58, 61, 107, 110] prepared recently by this method. The method of Schwertmann and Cornell yielded larger primary particles that were rhombohedral in shape, with lengths and widths (see Figure 2-2b) of roughly 39.5 (± 7.9) and 29.2 (± 5.4) nm, respectively (based on sizing of n = 100 particles). Hereafter, the two materials will be referred to as 8 nm and 40 nm, respectively.

From N_2-BET measurements, the specific surface area of 8 nm particles was 80 m^2/g, a value two-fold greater than that measured for 40 nm hematite (40 m^2/g). We report a standard deviation from replicate BET measurements of ± 6% for each sample. In their work with similarly sized hematite nanoparticles (7 and 37 nm), Madden and Hochella [57] found that specific surface areas from BET agreed well (within 3%) with geometric estimates for their larger, rhombohedral hematite particles. However, for their smaller hematite particles with pseudo-hexagonal platelet morphology, BET surface area was considerably less than their geometric estimate. From TEM and AFM characterization, they showed that the geometric surface area of their 7 nm particles could be reasonably approximated using a spherical morphology, in which specific surface area (in m^2/g) is equal to $3/(\rho \cdot r)$ where ρ is the density of hematite and r is the average radius for the assumed spherical particles. Indeed, such an estimate of geometric surface area for our 8.1 (± 1.6) nm particles (140 ± 30 m^2/g) was significantly greater than the value

measured via N_2-BET, now yielding a value 3.5 (±0.7)-fold greater than that for 40 nm hematite.

2.4.2 Stability of hematite nanoparticle suspensions. Representative sedimentation curves for suspensions of each hematite particle size are shown in Figure 2-3a. Comparison coefficients of sedimentation were quantified by assuming changes in absorbance over time initially followed exponential decay (representative model fits are provided in Figure 2-3a). Comparison of *k*(sedimentation) and hydrodynamic diameter are shown in Figure 2-3b. The relationship follows expectations, in which larger hydrodynamic diameters generally correspond to the greatest coefficients of sedimentation. The data also show the relatively strong agreement between the suspension stability of 8 and 40 nm hematite, suggesting that aggregates of comparable size are generated in each suspension. These first-order sedimentation coefficients [or *k*(sedimentation) values] are presented as a function of pH for suspensions of 8 and 40 nm hematite in Figure 2-4a. Over the pH range considered, *k*(sedimentation) values were essentially equivalent for 8 and 40 nm suspensions, which generally exhibited greater stability [i.e., lower values of *k*(sedimentation)] at pH values well below the point of zero charge for hematite (reported pH_{zpc} values range from pH 8.5-8.8) [24]. An exception occurred in pH 1 suspensions of 40 nm hematite, likely in response to the higher ionic strength in these suspensions. Notably, 8 nm suspensions at pH 1 generally followed the trend in increasing stability at lower pH values, a difference between 8 and 40 nm suspension stability that is not entirely understood.

Characterization by DLS further supports formation of similarly sized aggregates in suspensions of each hematite particle size. At most pH values, nearly identical hydrodynamic diameters were measured for steady-state aggregates in each suspension (Figure 2-4b). Notably, average hydrodynamic diameters were one to two orders of magnitude greater than the primary particles sizes from TEM, even at pH values far below the pH_{zpc} of hematite, revealing extensive aggregation over the entire pH range. As

expected, hydrodynamic diameters did increase with pH (from ~500 nm at pH 2 to ~1500 nm at pH 7), a trend that agrees well with observations from sedimentation studies (Figure 2-3b).

2.4.3 Characterization of suspended hematite aggregates. During alkalimetric titration (Figure 2-5a), greater volumes of 0.1 M NaOH were needed to increase the pH of suspensions with 8 nm hematite particles, indicating they exhibited greater total acidity (i.e., base-neutralizing capacity) than the 40 nm particles. Despite this difference, the inflection points of the titration curves, corresponding to the greatest buffering capacity of each suspension due to surface deprotonation, were nearly identical for 8 and 40 nm suspensions (pH 5.6 and 5.4, respectively). Thus, while the acid-base character (i.e., surface pK_a values) of each size of hematite is similar, the amount of ionizable surface hydroxyl groups from which the suspension's base neutralizing capacity is derived is markedly greater for aggregates of 8 nm particles. We also observed relatively minor differences in pH-dependent zeta potential values for suspensions of 8 and 40 nm hematite (Figure 2-5b). For suspensions of each particle size, zeta potentials were initially positive (~30 mV) and roughly constant up to pH 5. Above pH 5, zeta potentials rapidly decreased, yielding negative values above pH 6.0. Their near identical magnitude and pH-dependence of zeta potential values further suggest remarkable similarity in the surface chemistry of suspended aggregates constructed of 8 and 40 nm hematite particles.

2.4.4 Proton-promoted dissolution. Representative Fe(III) concentration profiles with corresponding fits from linear regression analyses are shown in Figure 2-6. Whereas measured proton-promoted dissolution rates of ferric iron (i.e., d[Fe(III)]/dt) are shown in Figure 2-7. In Figure 2-7, proton-promoted dissolution rates are plotted as a function of pH for suspensions of 8 and 40 nm hematite. Suspensions of 8 nm primary particles exhibited anywhere between 3.4-and 10-fold greater dissolution rates relative to suspensions of 40 nm particles.

This magnitude of enhancement is greater than anticipated from the difference in specific surface area between 8 and 40 nm hematite measured by N_2-BET and equal to or greater than surface area differences when a spherical geometry is assumed for 8 nm hematite. Although normalization of reactivity metrics by BET or geometric specific surface area is commonly used to evaluate size-dependent reactivity of nanomaterials [15], this procedure must be applied with caution to our suspensions in which multiple lines of evidence support their extensive aggregation. Specifically, while specific surface area is a characteristic of hematite primary particles, rates reported in Figure 2-7 reflect aggregate dissolution. Given that the extent of aggregation, and thus presumably the availability of reactive surface area, varies both as a function of the hematite primary particle size and suspension pH, the magnitude and trend of surface-area-normalized dissolution rates for 8 and 40 nm hematite are of highly uncertain value.

Rates of iron oxide dissolution via protonation are described empirically according to Eq. 2-1 [24], in which $[H^+]$ is the aqueous concentration of protons, k is the rate-coefficient for proton-promoted dissolution, and n is the reaction order with respect to aqueous phase protons. Reported n values for proton-promoted dissolution range between 0 and 1, with typical values often close to 0.5 [24].

$$d[\text{Fe(III)}]/dt = k[H^+]^n \qquad (2\text{-}1)$$

$$\log(d[\text{Fe(III)}]/dt) = \log k - n\text{pH} \qquad (2\text{-}2)$$

For 8 and 40 nm hematite suspensions, linear plots of $\log(d[\text{Fe(III)}]/dt)$ versus pH (Eq. 2-2) yielded n values of 1.0 and 1.2, respectively, revealing a likely first-order dependence on $[H^+]$ for both particle sizes. A comparable dependence on $[H^+]$ was reported previously for the initial 2-3% of goethite proton-promoted dissolution [123], although we observed considerably more dissolution of hematite herein (e.g., over one week roughly 18% of hematite mass dissolved in 8 nm suspensions at pH 1.0). The relatively strong dependence on $[H^+]$, and therefore pH, may be in part due to our choice

of HCl in dissolution experiments, as chloride is known to promote dissolution of iron oxides [123].

It is noteworthy that proton-promoted dissolution rates of 8 nm suspensions are consistently greater than 40 nm suspensions at all pH. First, this reactivity trend runs counter to that observed for hematite aggregation, in which measured hydrodynamic diameters and sedimentation rates indicate more extensive aggregation in 8 nm suspensions than 40 nm suspensions at pH 1 (see Figure 2-4). We caution, however, that this may simply reflect differences in aggregate structure, which Gilbert et al. [78] have shown to be a critical variable in governing nanoscale iron oxide interfacial reactivity.

Second, this behavior is in marked contrast to recent reports [64] of size-dependent dissolution for goethite nanorods and microrods. While nanorods exhibited higher mass- and surface-area-normalized rates for proton-promoted dissolution at pH 2, Rubansinghe et al. [64] found nanorod dissolution was orders of magnitude slower than microrods at pH 1. Formation of dense nanorod aggregates was implicated as the cause for their quenched dissolution activity. Our contrasting result emphasizes that in addition to aggregate size and structure, factors such as phase (hematite versus goethite) and primary particle morphology (rod versus spherical) are also likely to influence size-dependent dissolution trends.

2.4.5 Oxalate-promoted dissolution. For dissolution in the presence of 1 mM oxalate, suspensions of 8 nm hematite exhibited between 3.9- to 5.2-fold greater reactivity than 40 nm suspensions (Figure 2-7) over the pH range from 2 to 4. This extent of enhanced dissolution is comparable to that observed for hematite proton-promoted dissolution and reminiscent of the nearly 10-fold increase in mass-normalized rate of oxalate-promoted dissolution (pH 3, 1 mM oxalate) previously reported for goethite nanorods (81 ± (27) nm × 7 ± (2) nm) relative to microrods (670 ± (370) nm × 25 ± (9) nm) [59]. Consistent with established behavior [124], the rates of oxalate-promoted dissolution were considerably greater than proton-promoted dissolution rates for each

particle size of hematite. At pH 2, for example, rates of oxalate-promoted dissolution were approximately 125- and 250-fold greater than proton-promoted dissolution rates for 8 and 40 nm hematite suspensions, respectively.

The rate of iron release in ligand-containing suspensions is dependent upon both the adsorbed concentration of the ligand and protons (Eqs 2-3 and 2-4) [46].

$$d[\mathrm{Fe(III)}]/dt = k\,\Gamma^{m}[\mathrm{H^{+}}]^{n} \qquad (2\text{-}3)$$

$$\log(d[\mathrm{Fe(III)}]/dt) = \log k + m\log\Gamma - n\mathrm{pH} \qquad (2\text{-}4)$$

In Eqs 2-3 and 2-4, Γ is the surface concentration of oxalate, $[H^{+}]$ is the proton concentration in bulk solution, and *m* and *n* represent the empirical reaction orders for the ligand and protons, respectively. The rate-determining step in oxalate-promoted dissolution of hematite is proposed to be the release of the adsorbed complex via breaking of the Fe-O bond at the hematite surface [46].

We observed rates of oxalate-promoted dissolution to be nearly independent of pH, with plots of $\log(d[\mathrm{Fe(III)}]/dt)$ versus pH yielding *n* values of 0.3 and 0.2 for 8 and 40 nm hematite suspensions, respectively (Figure 2-7). Once again, as we observed for proton-promoted dissolution, these relationships are roughly independent of hematite primary particle size. Measured reaction orders also agree reasonably well with earlier results of Zhang et al. [46] who reported a *n* value of 0.1 for dissolution of 90 nm hematite by oxalate over the pH range 1.5 to 4.0. This implies that the pH-dependent reactivity of hematite toward oxalate may be predictable over a much broader range of primary particle sizes. We note that Zhang et al. [46] also reported a first-order dependence of Fe(III) dissolution on adsorbed oxalate concentrations. We are unable to report accurate *m* values because significant Fe(III) dissolution occurred over the timescales necessary for sorption equilibrium with oxalate. Instead, the influence of adsorbed oxalate concentration is considered for the photochemical dissolution of hematite, for which experiments were conducted at higher pH values where rates of non-photochemical dissolution by oxalate were negligible.

2.4.6 Reductive dissolution with ascorbic acid. Reduction of hematite by excess (10 mM) ascorbic acid (pK_a values of 4.1 and 11.8) yielded enhanced rates of Fe(II) production in suspensions of 8 nm hematite relative to 40 nm particles (Figure 2-8).

From pH 2 to 6, reductive dissolution of 8 nm hematite was between 3.3-6.5 times faster than in 40 nm hematite suspensions on the basis of mass, a difference roughly equivalent to reports by Echigo et al.[61] for ascorbic acid reduction of similarly sized hematite nanoparticles (7 and 30 nm) at pH 3.35. Thus, the relative reactivity of 8 and 40 nm suspensions is consistent across both reductive and non-reductive (e.g., proton- and oxalate-promoted) dissolution processes.

Hematite reduction by ascorbic acid has been extensively studied at fixed pH values, where dissolution is modeled as a second-order process involving charge transfer between an Fe(III) center and surface-complexed ascorbate. The rate-determining step is detachment of Fe(II) from the hematite surface [125], which is accelerated by protonation of adjacent surface sites. Thus, as was observed herein (Figure 2-8), rates of Fe(II) production typically increase with decreasing pH values even though the concentration of adsorbed ascorbate is typically less at lower pH values [125]. As with oxalate, adsorbed concentrations of ascorbate were not explicitly measured because of significant Fe(II) release over the timescales necessary for sorption equilibrium.

As with the other dissolution processes, the empirical rate law describing the influence of pH on hematite reduction by ascorbate is shown in Eqs 2-5 and 2-6, where all variables are as previously defined for oxalate-promoted dissolution (see Eqs 2-3 and 2-4).

$$d[\mathrm{Fe(II)}]/dt = k\Gamma^{m}[\mathrm{H^{+}}]^{n} \qquad (2\text{-}5)$$

$$\log(d[\mathrm{Fe(II)}]/dt) = \log k + m\log\Gamma - n\mathrm{pH} \qquad (2\text{-}6)$$

Previously, Suter et al. [125] reported a n value of 0.36 for 65 nm hematite for reaction with 0.1 mM ascorbate over pH 2.5-4.0. We observed comparable pH

dependencies in suspensions of 8 and 40 nm hematite, with plots of (d[Fe(II)]/dt) versus pH yielding nearly identical n values of 0.26 and 0.28, respectively.

As with all other dissolution processes, 8 and 40 nm suspensions exhibit essentially identical dependencies on pH for reduction by ascorbic acid. These results are practically significant, suggesting that changes in the dissolution activity of hematite in response to solution pH may be easily predictable across various aquatic systems regardless of primary particle size. From a more fundamental perspective, the surface of hematite consists of a distribution of reactive sites (e.g., steps, kinks, defects, and adatoms) often implicated in dissolution [41, 111, 112]. Although the type and amounts of these sites are likely to vary with primary particle size and synthesis method [110], the identical relationships between dissolution rate and pH observed for 8 and 40 nm suspensions speaks to similarities in the rate-limiting steps controlling iron dissolution of their aggregates.

A final noteworthy outcome with ascorbic acid is the observation that 8 nm hematite suspensions remained more active than 40 nm hematite at pH values approaching circumneutral (i.e., pH 6). This represents among the first demonstration that enhanced dissolution of iron oxide nanoparticles can extend beyond acidic pH regimes. Naturally abundant nanoscale iron oxides can, therefore, exhibit enhanced dissolution in a far larger number of environmentally relevant aquatic systems (e.g., circumneutral surface waters) than is currently realized from outcomes of prior dissolution studies.

2.4.7 Photochemical reductive dissolution in oxalate-containing suspensions. Rates of Fe(II) production resulting from irradiation of 0.5 g/L hematite suspensions in the presence of 1 mM oxalate are shown as a function of pH in Figure 2-9a. Comparison of Fe(II) production rates on the basis of hematite mass loading reveals size-dependent trends consistent with the other dissolution mechanisms considered. Specifically, Fe(II) production rates were between 3.5-7 times greater in suspensions of 8 nm hematite relative to 40 nm hematite over the pH range considered, which extended to pH 7.

Further, the pH-dependent trends in dissolution were essentially identical for both particle sizes, with plots of log(d[Fe(II)]/dt) versus pH yielding n values 0.67 and 0.70 for 8 and 40 nm hematite, respectively. We note that in control experiments examining hematite photoreduction in the absence of oxalate, Fe(II) was not measurable (i.e., below our analytical detection limit) over the timescales associated with Fe(II) production in the presence of oxalate.

The higher pH values (pH > 5) used in photoreductive dissolution studies produced negligible rates of dissolution in non-irradiated (i.e., dark) hematite suspensions. In dark control experiments, therefore, we were able to quantify accurately the extent of oxalate adsorption in suspensions of each hematite particle size. From Sulzberger and co-workers [55, 56], it is generally believed that the Fe-oxalate surface complex is the chromophore that initiates Fe(III) reduction (and oxalate oxidation) via ligand-to-metal charge transfer. Accordingly, the extent of oxalate uptake in suspensions of each particle size should provide insight as to the relative number of photoactive surface complexes, and thus surface sites for oxalate uptake and Fe(II) dissolution, on suspended aggregates of 8 and 40 nm hematite.

The pH-edge behavior for oxalate adsorption in suspensions of 8 and 40 nm hematite is shown in Figure 2-9b, while rates of Fe(II) photochemical dissolution normalized to adsorbed oxalate concentrations are presented in Figure 2-9c. As expected for adsorption of an anionic solute on iron oxides [24], the amount of adsorbed oxalate decreases with increasing pH. The mass of adsorbed oxalate per gram of hematite was 3-to-4-fold greater in 8 nm hematite suspensions, consistent with previous reports of greater affinity for Cu(II) uptake on 7 nm hematite versus 25 and 88 nm particles [107]. The magnitude of this increase in oxalate uptake is also on the order of the rate enhancement observed for the photoreductive dissolution of 8 nm hematite suspensions. Consequently, normalization by adsorbed oxalate concentrations reveals rates of Fe(II) production with

reasonable agreement between 8 and 40 nm hematite over the pH range investigated (Figure 2-9c).

The agreement in oxalate-normalized rates of photoreductive dissolution provides strong evidence that the reactivity difference between suspensions of 8 and 40 nm hematite simply relates to the amount of reactive surface area available in each system. The greater extent of oxalate uptake per unit mass on aggregates of 8 nm hematite implies that a greater fraction of the aggregate's surface area is available for oxalate complexation and photoreaction relative to aggregates of 40 nm hematite. We propose that this is likely also the case for proton-promoted, (dark) oxalate-promoted, and ascorbic acid mediated reductive dissolution. It remains unclear as to how well, if at all, differences in surface area measured or estimated for primary particles reflect the relative amount of reactive surface available on their similarly sized aggregates.

2.4.8 TEM images of hematite aggregates after reaction with ascorbic acid and oxalic acid. Recently, Echigo et al. [61] utilized high resolution HRTEM and high angle annular dark field –scanning transmission electron microscopy (HAADF-STEM) to evaluate morphological changes in two similarly sized hematite particles (7 and 30 nm) after reaction with 5 mM ascorbic acid at pH 3.35. They observed that their smaller hematite particles exhibited near uniform (i.e., isotropic) dissolution over the entire particle, while dissolution of their larger rhombohedral particles initiated along edges and at internal defects before occurring more uniformly across the particle surface over longer reaction times.

In this work, TEM was used to examine changes in primary particle and aggregate morphology arising from reaction of hematite suspensions with either 10 mM ascorbic acid at pH 2 for up to 13 days (resulting in approximately ~25 and 7% total Fe dissolution for 8 and 40 nm hematite, respectively). Representative TEM images of unreacted aggregates from 8 and 40 nm hematite suspensions are shown in Figure 2-10a

and 2-10e, respectively, whereas images collected as a function of reaction time are shown for 8 and 40 nm hematite in Figures 2-10b-d and 2-10f-h, respectively.

We note that during imaging, most particles in 8 and 40 nm suspensions were present as aggregates with little to no evidence of freely suspended primary particles. However, we are hesitant to draw any quantitative conclusions regarding aggregation state, aggregate size and aggregate morphology from these images due to structural changes potentially induced by sample preparation, drying, and analysis under vacuum. However, as in the work of Echigo et al. [61], relative morphological changes resulting from dissolution should be distinguishable from comparison of pre- and post-reaction images.

Our TEM analysis provides evidence that hematite dissolution proceeds as described by Echigo et al. [61] For suspensions of 40 nm hematite, dissolution via ascorbic acid resulted in slight, but visible changes to the morphology of primary particle within aggregates. A close comparison of Figure 2-10e (an unreacted 40 nm hematite aggregate) to Figure 2-10f (collected after 20 h of reaction) and Figures 2-10g and 2-10h (collected after 13 days of reaction) reveals that the corners of the rhombohedral particles become progressively more rounded after extensive reductive dissolution (as indicated by black arrows in Figures 2-10f), consistent with preferential reaction at these edge sites. The high magnification images in Figure 2-10h also show evidence for increased dissolution at internal defects within the primary particle. Both types of structural changes were also observed by Echigo et al. [61] for their 30 nm rhombohedral hematite.

In contrast, comparison of images collected for unreacted 8 nm hematite (Figure 2-10a) to those collected after 20 h (Figure 2-10b) and 13 days (Figures 2-10c and 2-10d) of reaction with ascorbic acid revealed little discernible change to the morphology of primary particles. Even though roughly one quarter of the total iron mass was solubilized after nearly two weeks, there were no obvious signs of preferential etching on the 8 nm particles within aggregates. We believe this difference in the dissolution of 8 nm and 40

nm hematite particles, which was also observed during oxalate-promoted dissolution (Figure 2-11), explains the near-consistent differences observed in the reactivity of their suspensions. Because dissolution of 8 nm hematite occurs more uniformly over the entire primary particle surface, their aggregates are also likely to be more uniformly prone to dissolution. In contrast, aggregates built from 40 nm particles with localized reactivity at edges and defects will exhibit a smaller fraction of their total surface area susceptible to dissolution.

2.5 Conclusion

In this work, batch dissolution studies in complement with material and suspension characterization yielded new insights into the size-dependent reactivity of hematite nanoparticles. Suspension characterization indicates extensive aggregation of 8 and 40 nm hematite particles over a broad pH range. Further, aggregates tend to grow to a steady-state value that is largely independent of the primary particle size used as the building block for aggregate formation. This steady-state size, often orders of magnitude greater than primary particle dimensions, likely relates to the aggregate surface area necessary to minimize surface free energy via solvation.

From dissolution studies, aggregates constructed of 8 nm hematite exhibit anywhere between 3.3- to 10-fold greater reactivity per unit mass than aggregates of 40 nm hematite. As evidenced by the empirical relationships between dissolution rate and pH developed herein, this reactivity difference was observed across all dissolution modes and pH values considered. Furthermore, this rate enhancement almost always surpasses expectations from specific surface area measured by BET (including 95% confidence intervals, 13 out of 15 dissolution rates measured for 8 nm suspensions are significantly greater than differences expected from BET surface area), and is also significantly greater in a near majority of cases when more conservative geometric estimates of surface area are instead used for 8 nm primary particles (7 out of 15 dissolution rates for 8 nm suspensions are significantly greater in this case). However, the likely loss of primary

particle surface area during their extensive aggregation in suspension introduces considerable uncertainty into such surface-area-normalized rate comparisons. In fact, we believe that the range of rate enhancements (3.3- to 10-fold) per unit mass exhibited by 8 nm hematite likely reflects subtle changes in the aggregation state and aggregate structure within both suspensions over the range of experimental conditions employed.

Accordingly, we contend that the dissolution rates reported herein are most reflective of aggregate reactivity rather than the reactivity of discretely dispersed hematite nanoparticles. Observed differences in the reactivity of 8 and 40 nm hematite suspensions therefore imply that comparably sized aggregates can exhibit vastly different reactivity depending on the nature of the primary particles from which they are constructed. Given that our suspensions are likely polydisperse mixtures of aggregates exhibiting a range of sizes, further work is needed to evaluate how hematite reactivity changes along the size spectrum from freely suspended, primary nanoparticles to the orders of magnitude larger aggregate sizes achieved at steady state.

The underlying cause of the reactivity difference between aggregates of 8 and 40 nm hematite merits further investigation. Based on data presented herein, we hypothesize that the difference simply results from more reactive surface area being available on aggregates of 8 nm hematite because 8 nm primary particles appear more uniformly reactive than 40 nm primary particles. This scenario is supported by TEM images, which support near uniform dissolution of 8 nm particles, whereas 40 nm hematite dissolves preferentially at edges and internal defects. Notably, our proposal runs counter to that of Echigo et al. [61], who hypothesized that the initially greater dissolution rate of their 7 nm hematite was attributable to dissolution of freely dispersed nanoparticles that were markedly more reactive than their aggregates. From suspension characterization conducted herein, we believe that the overwhelming majority of our hematite exists as aggregates, and that the number of freely dispersed particles is likely too small to affect significantly the macroscopic dissolution rates measured herein.

Regardless of the fundamental cause for their different reactivities, there are several practical implications of this work for iron redox cycling in natural aquatic environments. We provide some of the first evidence that nanoscale iron oxides will exhibit greater rates of soluble iron production per unit mass than larger phases in near-neutral pH soil, sediments, surface waters and aerosol, even when these particles extensively aggregated. We also present empirical relationships that will help to better quantify changes in hematite dissolution in response to variations in pH. For example, hematite is a common component of mineral dust aerosol, for which dissolution can occur under extremely acidic pH (e.g., arising from atmospheric processing with anthropogenic HNO_3 and H_2SO_4) or via photochemically driven processes [106, 126]. These relationships may help better predict the rate and extent of hematite dissolution, a process with implications for the amount of bioavailable iron upon aerosol deposition in nutrient-limited portions of the open ocean [127], over its lifetime in the atmosphere.

Finally, the consistency in the relative reactivity of 8 and 40 nm suspensions, as well as its general agreement with the existing literature for hematite dissolution, suggests similar reactivity trends are likely to be observed for dissolution processes not explicitly considered herein. For example, recent reports of size-dependent bioavailability of hematite to aerobic bacteria [128] implies this behavior also extends to siderophore-mediated dissolution [129, 130]. There are also potential implications for pollutant fate. The interaction of Fe(II) with hematite is now widely recognized as a redox process driven by interfacial electron transfer [26, 86, 131], a process that can influence the fate of trace metal pollutants (e.g., Ni(II) and Zn(II)) associated with the hematite surface or incorporated into its structure [132, 133]. We contend that the rate of interfacial electron transfer, and the uptake or release of trace pollutants driven by this process, will also exhibit similar trends in hematite particle and aggregate size reported herein. Similarly, photochemically generated Fe(II) can promote hydroxyl radical production in irradiated surface waters containing natural organic matter via Fenton chemistry [134]. Based on

results herein, nanoscale hematite phases may play a disproportionate role in the production of hydroxyl radical, a potent oxidant of organic micropollutants in surface waters, due to their greater rate of photoreduction in the presence of organic ligands.

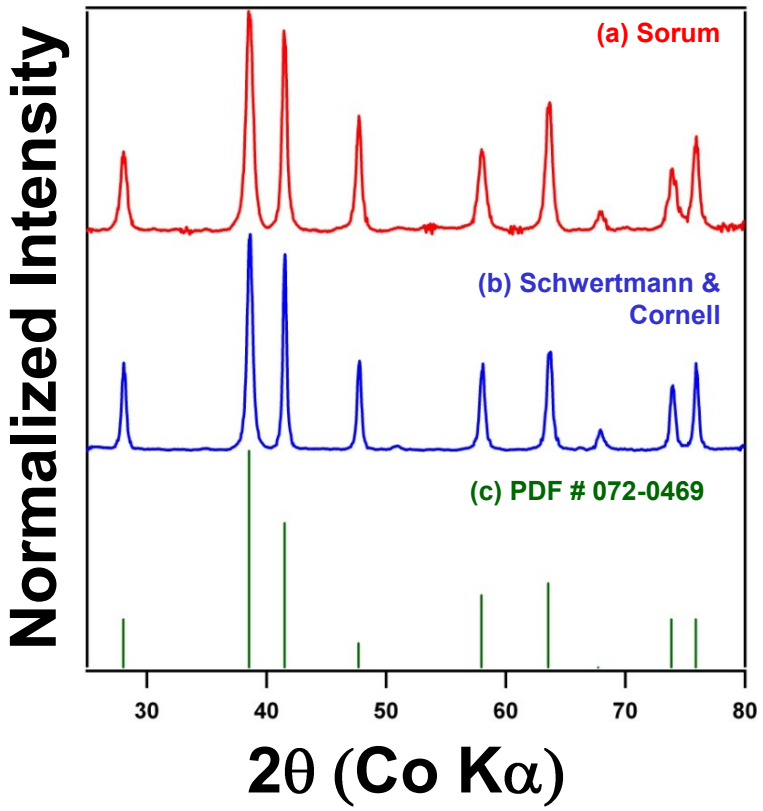

Figure 2-1 Powder X-ray diffraction (XRD) patterns for synthesis products derived from the methods of (a) Sorum [117] and (b) Schwertmann and Cornell [118]. Also provided is the reference pattern (PDF#072-0469) for hematite (α-Fe2O3). For comparison, the diffraction patterns are normalized to the diffraction line with greatest intensity (at 2θ of ~38°). This reveals the expected line broadening for the smaller (8 nm) primary particles produced by the method of Sorum relative to the larger primary particles (~40 nm) obtained from the method of Schwertmann and Cornell.

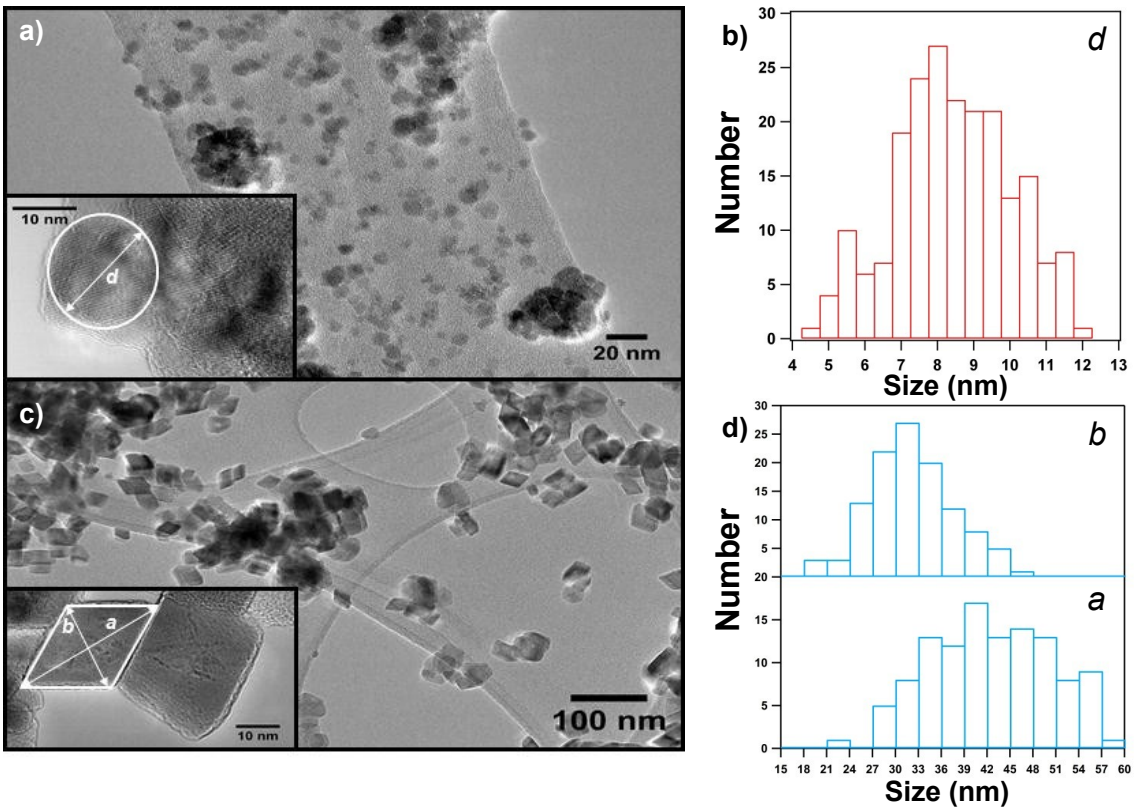

Figure 2-2 (a) TEM image of the synthesis product from Sorum's method. Based on sizing analysis of 200 particles (b), this method yielded particles that were approximated as spherical (see inset in (a)) with an average diameter, *d,* of 8.1 (± 1.6) nm. (c) TEM image of the synthesis product from the method of Schwertmann and Cornell, which was rhombohedral in shape (see inset in (c)). Sizing of 100 particles suggests they have an average length, *a*, of 39.5 (± 7.9) nm and width, *b*, of 29.2 (±5.4) nm, as defined by dimensions shown in the inset of (c).

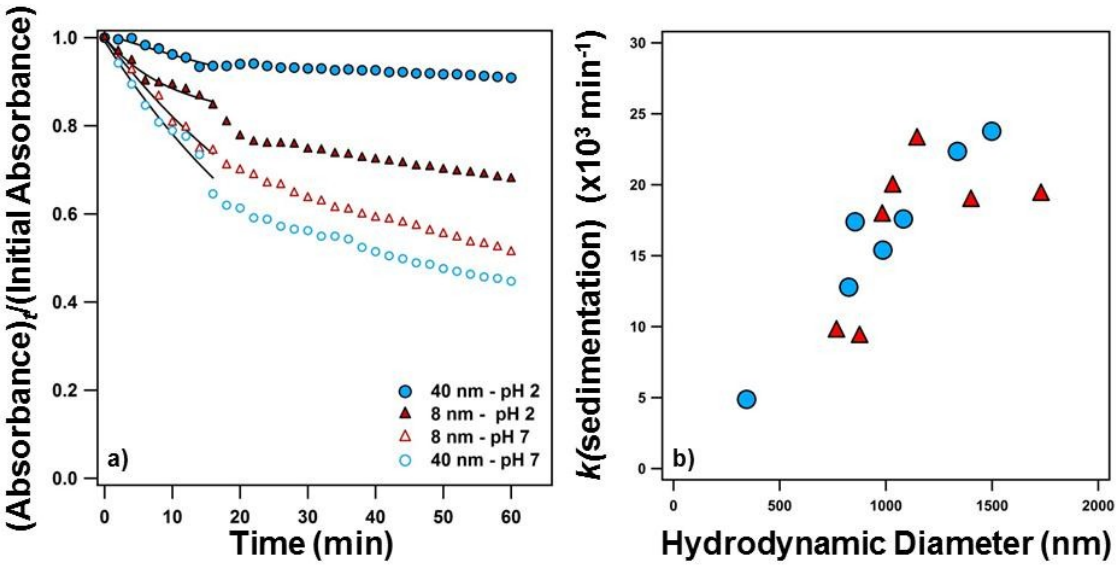

Figure 2-3 (a) Representative sedimentation curves obtained for 8 and 40 nm hematite suspensions pH 2 and pH 7. Also shown are exponential decay model fits applied to data for $t \leq 15$ min, which were used to determine first-order coefficients for sedimentation [or k(sedimentation) values]. Results of linear regression analysis typically yielded R^2 values greater than 0.9 (e.g., the R^2 values for data shown were 0.93 and 0.92 for 8 and 40 nm at pH 2, respectively, and 0.98 and 0.96 for 8 and 40 nm at pH 7, respectively. Sedimentation experiments were conducted with 0.5 g/L suspensions in 25 mM NaCl at an analytical wavelength (λ) of 510 nm. (b) Comparison of k(sedimentation) values obtained from sedimentation studies and hydrodynamic diameter values obtained from dynamic light scattering analysis for 8 and 40 nm hematite suspensions.

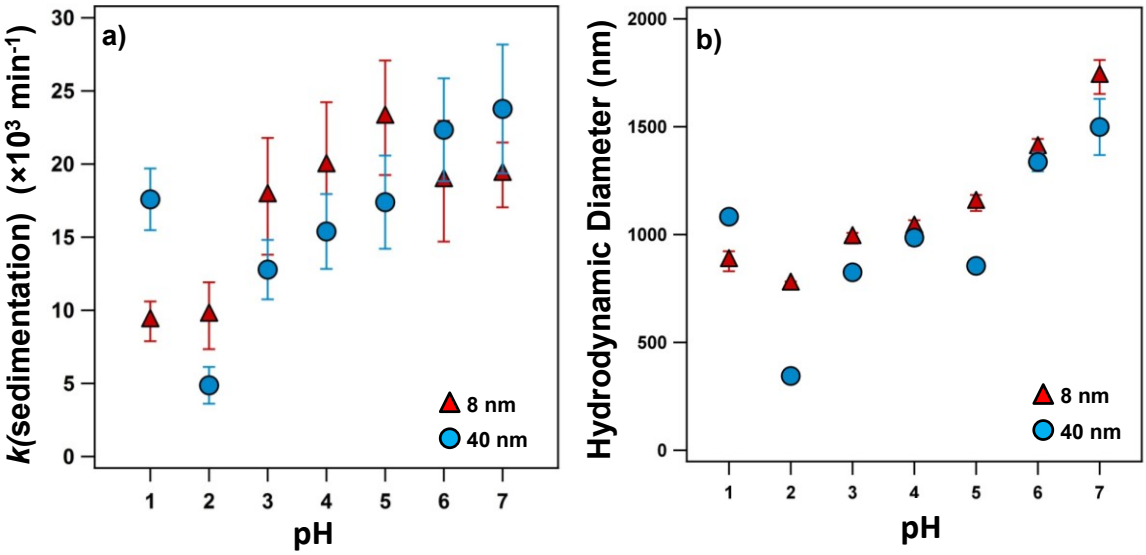

Figure 2-4 Sedimentation rate constants and hydrodynamic diameters based on pH. (a) Initial coefficients for settling [*k*(sedimentation) values] and (b) hydrodynamic diameters from DLS analysis as a function of pH for suspensions of 8 nm and 40 nm hematite (α-Fe_2O_3). Suspensions contained 0.5 g/L α-Fe_2O_3 and 25 mM NaCl (as noted in the text, ionic strength was slightly higher from pH 1-2 due to the HCl concentration necessary to achieve these low pH values). All suspensions were made at least 12 hours in advance and allowed to equilibrate before analysis. Sedimentation coefficients were determined by modeling the initial change (for data $t \leq 15$ min) in light transmittance ($\lambda_{incident}$ = 510 nm) through hematite suspensions as a first-order process (i.e., exponential decay). Uncertainty associated with *k*(sedimentation) values represents 95% confidence levels associated with the linear regression analysis used in their quantification from semi-log plots of absorbance versus time. Uncertainties in hydrodynamic diameters represent standard deviations from triplicate analyses.

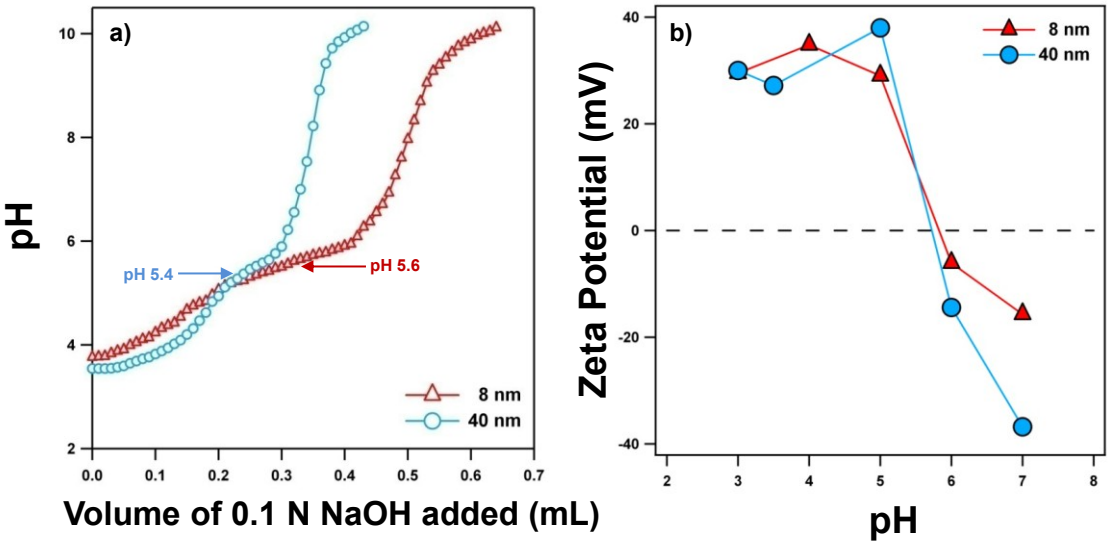

Figure 2-5 Alkalimetric titrations curves and zeta potential (a) Alkalimetric titration performed on 4 g/L suspensions of 8 and 40 nm hematite. Initially near pH 4.0, suspensions were autotitrated with 0.1 N NaOH until reaching a final pH of 10. Titrations clearly reveal that a larger volume of base was necessary to raise the 8 nm hematite suspension to pH 10, thus indicating its greater base-neutralizing capacity for these particles. (b) Zeta potential measurements as a function of pH for 8 and 40 nm hematite suspensions. Suspensions of 0.5 g/L were prepared in 25 mM NaCl, adjusted to the appropriate pH with dilute acid or base, and subsequently diluted to an absorbance of 0.3-0.35 at λ of 246 nm for zeta potential analysis.

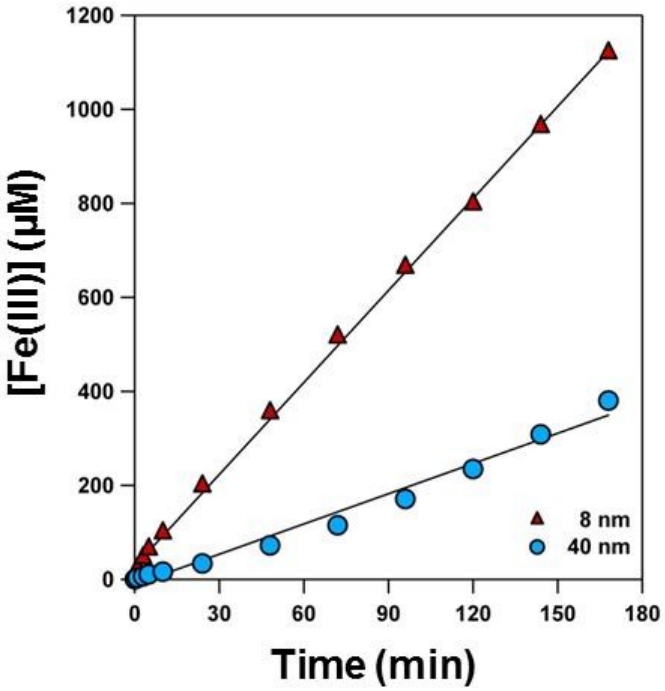

Figure 2-6 Representative Fe(III) dissolution curves for proton-promoted dissolution of 8 and 40 nm hematite suspensions Suspensions consist of 0.5 g/L at pH 1. Also shown are the results of best fit linear regression analyses, from which the rate of Fe(III) dissolution was quantified using the resulting slope. For all dissolution mechanisms considered (i.e., proton-promoted, oxalate-promoted, reductive dissolution via ascorbic acid, photoreductive dissolution in irradiated oxalate suspensions), Fe(III) or Fe(II) concentration profiles over time were of comparable quality and all experiments were conducted in triplicate to account for uncertainty.

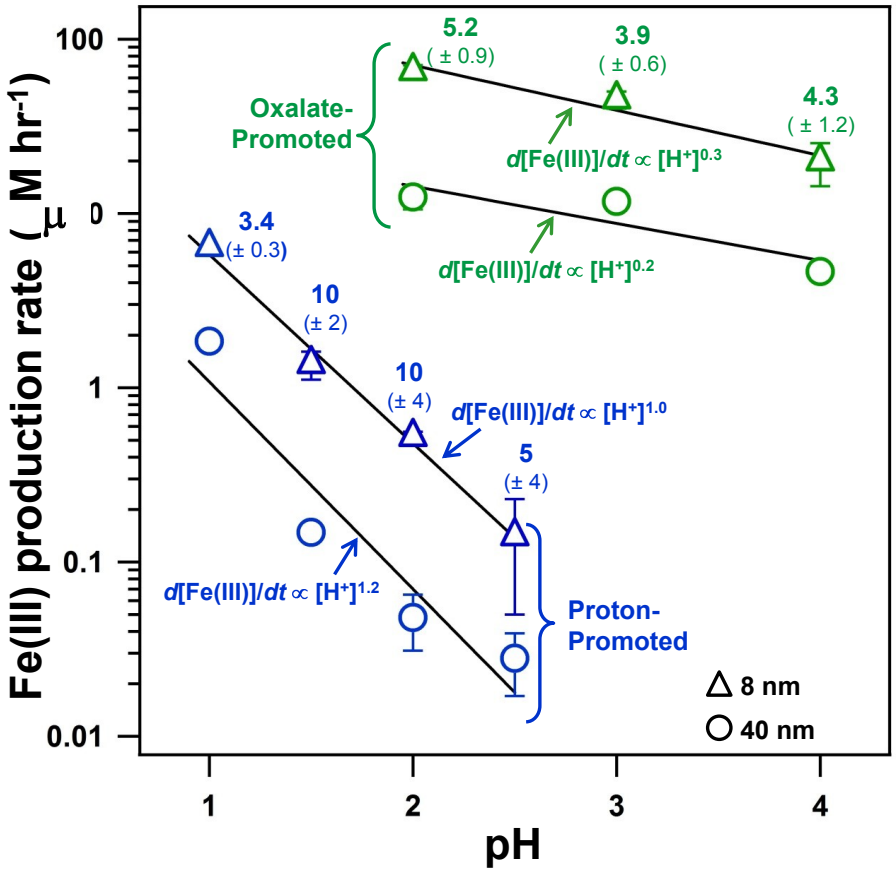

Figure 2-7. Rates of proton-promoted dissolution (blue) and oxalate (1 mM) promoted dissolution (green) for 8 and 40 nm hematite suspensions as a function of pH. Numbers adjacent to 8 nm data points (triangles) indicate their magnitude of rate enhancement (including 95% confidence intervals) relative to 40 nm particles (circles). Lines represent results of best-fit linear regression analyses to determine the empirical relationship between dissolution rate and $[H^+]$, results of which are provided. All suspensions contained 0.5 g/L α-Fe_2O_3 and 25 mM NaCl (as noted in the text, ionic strength was slightly higher from pH 1-2 due to the HCl concentration necessary to achieve these low pH values). Uncertainties represent one standard deviation from at triplicate dissolution experiments. Dissolution rates were quantified from the initially linear increase in soluble Fe(III) concentration over time as described in the text. Uncertainties associated with rate data represent the 95% confidence interval for the slope of this linear-regression analysis.

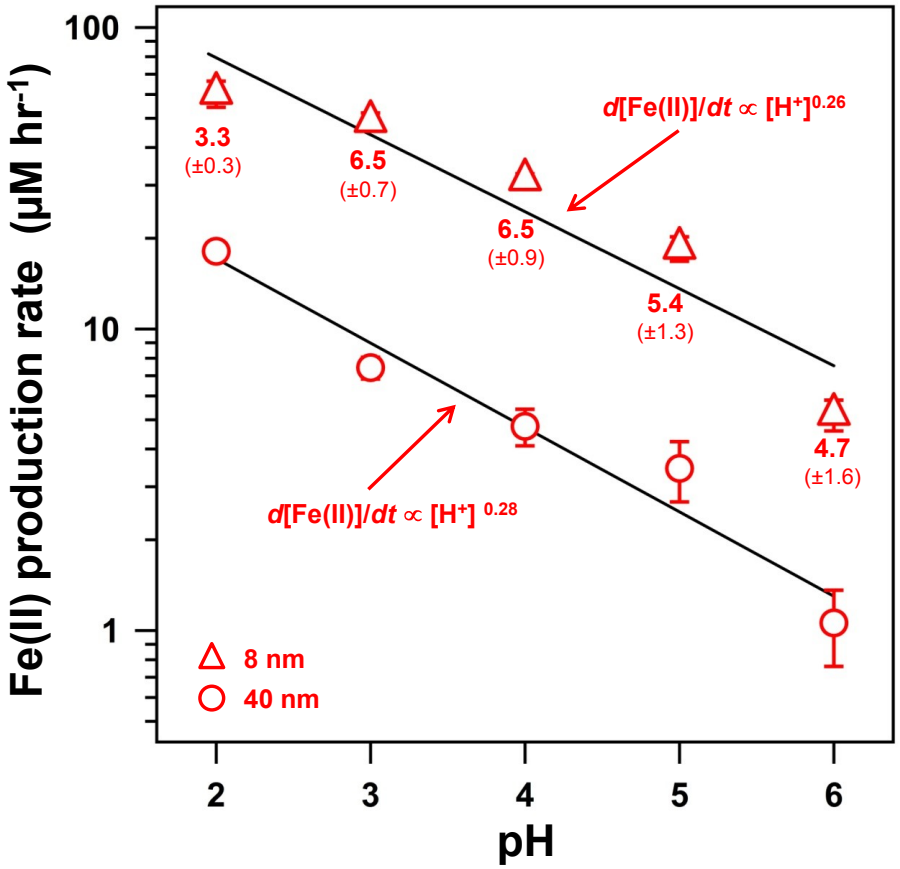

Figure 2-8 Rate of reductive dissolution via reaction of ascorbic acid (10 mM) with 8 or 40 nm hematite suspensions as a function of pH. Numbers adjacent to 8 nm data points (triangles) indicate their magnitude of rate enhancement (including 95% confidence intervals) relative to 40 nm particles (circles). Lines represent results of best-fit linear regression analyses to determine the empirical relationship between dissolution rate and $[H^+]$, results of which are provided. All suspensions contained 0.5 g/L α-Fe_2O_3 and 25 mM NaCl (as noted in the text, ionic strength was slightly higher at pH 2 due to the HCl concentration necessary to achieve this low pH values). Dissolution rates were quantified from the initially linear increase in soluble Fe(III) concentration over time as described in the text. Uncertainties associated with rate data represent the 95% confidence interval for the slope of this linear-regression analysis.

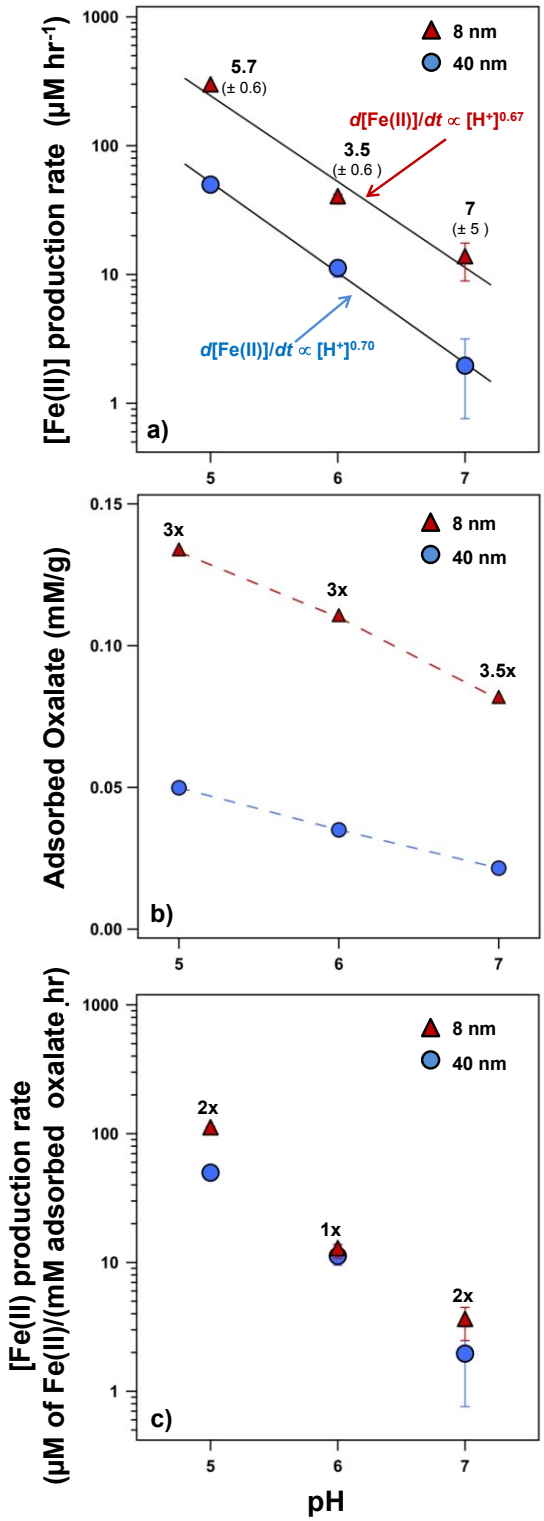

Figure 2-9 Photoreductive dissolution rates, oxalate absorption, and oxalate nomalized photoredutive dissolution rates (a) Rates photoreductive dissolution as a function of pH in hematite suspensions containing 0.5 g/L of 8 and 40 nm α-Fe_2O_3 and 1 mM oxalate. Lines represent results of best-fit linear regression analyses to determine the empirical relationship between dissolution rate and $[H^+]$, results of which (*continued on page 54*)

are provided. Reactions were conducted in the absence of O_2, and suspensions also contained 25 mM NaCl. Dissolution rates were quantified from the initially linear increase in soluble Fe(III) concentration over time as described in the text. Uncertainties associated with rate data represent the 95% confidence interval for the slope of this linear-regression analysis. (b) Adsorbed oxalate concentration determined from dark control experiments. Adsorbed oxalate concentrations are shown as a function of pH per unit mass of 8 and 40 nm α-Fe_2O_3. (c) Rates of photoreductive hematite dissolution normalized to the concentration of adsorbed oxalate. In all instances, numbers adjacent to 8 nm data points (triangles) indicate their magnitude of rate enhancement (including 95% confidence intervals) relative to 40 nm particles (circles).

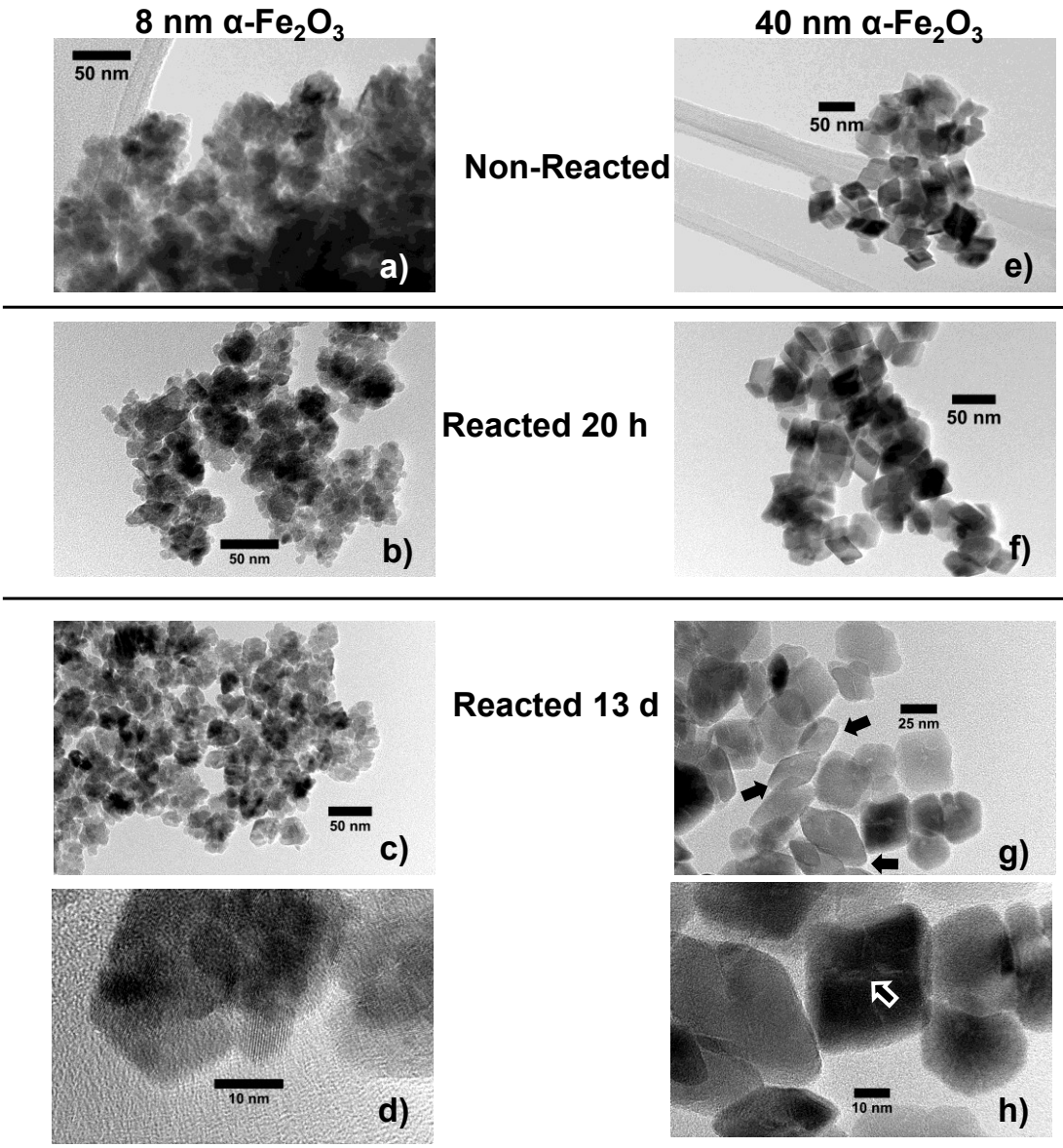

Figure 2-10 TEM images before and after reductive dissolution. TEM images of 8 and 40 nm hematite before (a and e, respectively) and after reaction with 10 mM ascorbic acid at pH 2 for 20 hours (b and f, respectively) and 13 days (c, d and g, h, respectively). For images of 40 nm hematite, evidence of dissolution along edges (indicated by black arrows) and internal defects (indicated by white outline arrow) is highlighted.

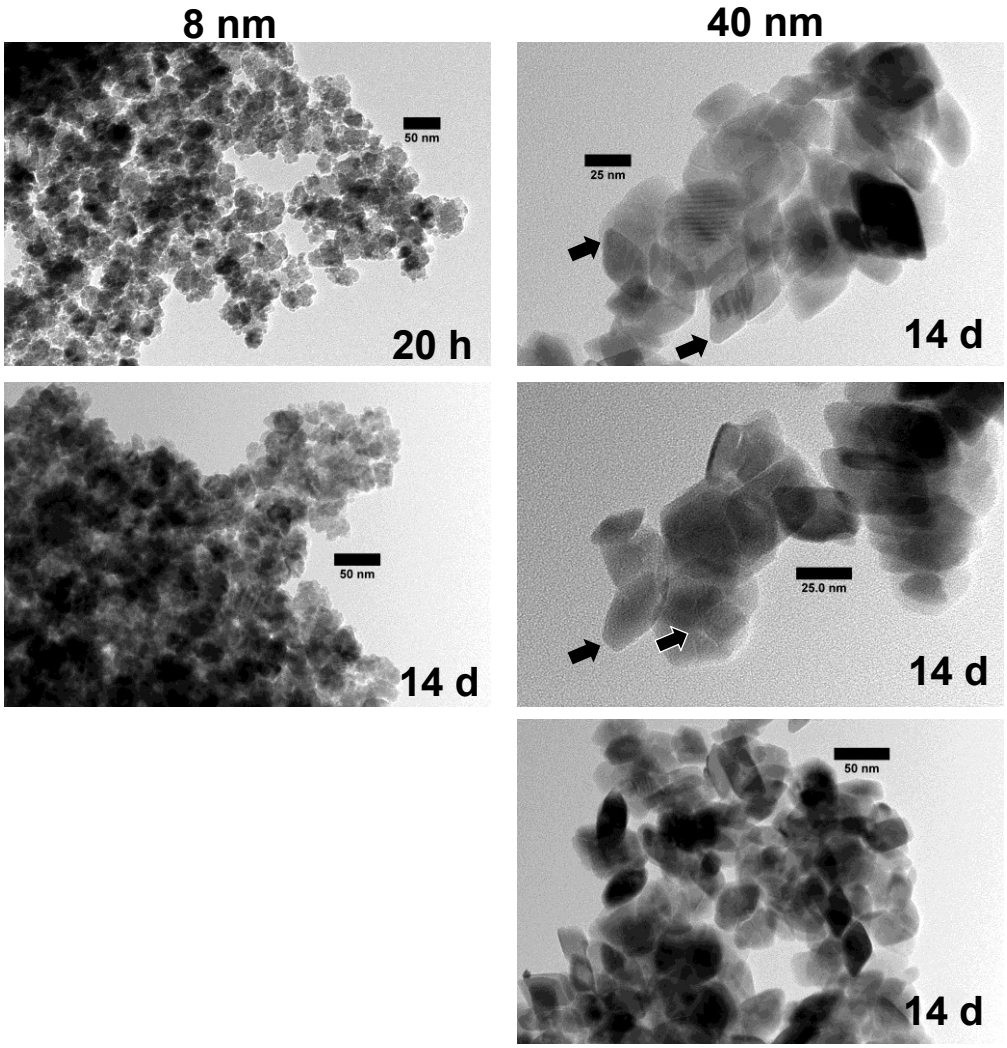

Figure 2-11 TEM images before and after oxalate promoted dissolution.TEM images of aggregates of 8 nm hematite (on left) and 40 nm hematite (on right) as a function of reaction time (either 20 h or 14 d) with 1 mM oxalate at pH 2. While TEM images of 8 nm aggregates show little discernible change in the morphology of primary particles comprising the aggregate, 40 nm particles within aggregates exhibit rounding, indicative of preferential etching at their sharpest edges (indicted by black arrows). Also over 14 d, evidence develops for dissolution via internal defects within the hematite (indicated by the white outlined arrow). Similar changes in particle morphology were also observed for aggregates of 8 and 40 nm hematite after reaction with 10 mM ascorbic acid at pH 2 (see Figure 2-10).

CHAPTER 3
INFLUENCE OF AGGREGATE SIZE ON THE REDUCTIVE DISSOLUTION OF NANOSCALE HEMATITE

3.1 Abstract

Naturally produced nanomaterials such as iron oxides are expected to be extensively aggregated in aquatic systems, a process that is expected to limit primary particle reactivity because of the reactive surface consumed when they coalesce into larger aggregates. Here, we show that aggregation has little to no effect on mass normalized rates of reductive dissolution (r_M values) for several types of iron oxides. Working most extensively with two sizes of nanohematite (8 and 40 nm) gravity fractionation was used to produce hematite suspensions with a range of aggregate sizes. In complement to microscopic (e.g., cryo-TEM) characterization of suspensions, the reactivity of these fractions was then assessed in reductive dissolution experiments with ascorbic acid. Generally, values of r_M were essentially constant for all aggregates in suspensions prepared from 8 and 40 nm hematite powders, in turn causing the roughly 5-fold greater reactivity of 8 nm suspensions relative to 40 nm suspensions to be independent of aggregate size. Only a 4-fold greater r_M value was observed for the lightest 5% of hematite mass in these 8 nm suspensions, an increase that is rather small considering that aggregates in this lightest fraction (on the order of 50-200 nm) were considerably smaller than those present in the heavier fractions (at times exceeding 1 μm). Further, a negligible influence of aggregation on r_M was also observed for other forms of iron oxides investigated including nanoferrihydrite and two sizes of goethite (i.e., microrods and nanorods). Additional experiments revealed that different mechanisms of aggregation (e.g., induced by drying or increasing ionic strength) also exerted little to no impact on reductive dissolution rates of hematite and these other oxides. Interestingly, during oxalate promoted and proton promoted dissolution of hematite, a decrease in the rate and extent of dissolution was observed at high ionic

strength, suggesting that aggregation effects on nanomaterial reactivity may be process dependent.

3.2 Introduction

Consensus is growing that nanoscale iron (oxyhydr)oxide (hereafter iron oxides) are ubiquitous [19-21] in the environment, exhibit unique size-dependent reactivity relative to larger analogs [57-61, 63-65, 99, 103, 107, 115, 128, 135, 136], and as such play a disproportionate role in iron redox cycling, among other processes, in natural systems [137-140]. However, while primary particle size is often assumed to influence reactivity, truly monodispersed nanoparticles will rarely be observed in natural aquatic systems. Instead, natural iron oxide nanomaterials are near certain to coalesce into large aggregates assembled from numerous primary particles, which may exhibit reactivity vastly different from the primary particles from which they are constructed and thereby confound our ability to assess the role of natural nanoparticles in the hydrosphere, lithosphere and atmosphere.

Several environmental factors are known to induce iron oxide aggregation, and thus are also expected to indirectly influence nanoparticle reactivity in natural systems. Primarily, iron oxide nanoparticle aggregation is a function of surface charge arising from the pH-dependent character of their surface hydroxyl groups [141], as described by DLVO (Deraguin, Landau, Verwey and Overbeek) theory [142]. Accordingly, the pH and ionic strength of the surrounding aqueous environment are key factors controlling the rate and extent of nanoparticle aggregation in suspensions [24, 143, 144]. Nanoparticle concentration in suspension can also affect aggregation, where higher concentrations generally produce larger aggregates under otherwise equivalent solution conditions [145, 146], presumably from the increased probability of particle collision by Brownian motion and/or shear induced forces (e.g., mixing) [147]. Iron oxide suspension stability will also be influenced by dissolved constituents including natural organic matter (NOM) [80, 146] or anthropogenic organic material such as synthetic polymers [148], and ionic surfactants

[149]. Finally, physical changes to nanoparticle suspensions, such as drying or freezing, can induce aggregation. For example, Gilbert et al. [78] determined that freezing and drying ferric iron oxyhydroxide particle suspensions produced aggregates that were more compact and exhibited less internal porosity than those generated via solution changes (i.e., pH and ionic strength). Similar results with freezing and freeze-drying were obtained by Raiswell et al. [77] on 2-line ferrihydrite.

All of the aforementioned system variables may influence iron oxide nanoparticle reactivity because they alter the size, structure and morphology of their aggregates. Because the rate of interfacial processes typically scale with available surface area (i.e., surface active sites), it is widely accepted that aggregation will ultimately limit reactivity by restricting access to reactive sites embedded within the aggregate. Indeed, several recent studies [64, 77, 78, 82, 103, 108, 115] have demonstrated the inhibitory effect of aggregation on the reactivity of nanomaterials toward various interfacial processes. For iron oxides, Rubasinghege et al. [64] observed complete quenching of proton-promoted dissolution in nanorod goethite suspensions at high ionic strength (or low pH), which they attributed to aggregation. Gilbert et al. [78] found that highly compact aggregates of ferric iron oxyhydroxide nanoparticles generated via drying had significantly reduced Cu(II) uptake compared to alternative, solution-based aggregation mechanisms (i.e., pH and ionic strength). Similarly, metal release from ferric iron oxyhydroxide nanoparticle aggregates produced via different mechanisms (e.g., drying, pH and ionic strength) exhibited different rates of release, illustrating the influence of aggregation mechanism and aggregate structure on suspension reactivity.

Nevertheless, we contend that questions about the influence of aggregation and aggregate size on interfacial reactivity merit closer scrutiny. First, there are reports in which aggregation exerts little to no impact on nanoparticle suspension reactivity. For example, Cwiertny et al. [84] observed the same extent of Fe(II) sorption per gram of nanogoethite in suspensions prepared across a wide range of particle concentrations,

where the greater extent of aggregation at high solid loadings would be anticipated to result in smaller mass-normalized capacity for Fe(II). Although such observations remain largely unexplained, it may reflect that the impact on reactivity is specific to particular aggregation mechanisms or interfacial processes. Second, it is not clear whether size-dependent nanoparticle reactivity is conserved in aggregates constructed from those nanoparticles. We previously [136] observed suspensions of 8 nm hematite to be generally 5-fold more prone to dissolution than suspensions of 40 nm hematite, but notably found that both sizes of nanoparticles aggregated significantly and to comparable extents in our solutions. As such, our prior results best reflect the average of aggregate reactivity and provide no real indicator as to the relative reactivity of the smallest aggregates or primary particles of 8 and 40 nm hematite, which would be of greatest environmental relevance due to their stability in the water column. Inherently, the distribution of aggregate sizes in a single suspension makes it difficult to accurately quantify size-dependent nanoparticle reactivity. In fact, Echigo et al. [61] concluded that differential reactivity exhibited by the most reactive, monodisperse nanoparticles could explain the greater reductive dissolution rates observed in suspensions of 7 nm hematite relative to those of 40 nm.

Here, we seek to understand how aggregation influences interfacial reactivity of iron oxide nanoparticles. Specifically, we focus our efforts on hematite nanoparticles and the influence of aggregate size, morphology, and aggregation mechanisms on established trends in hematite dissolution [61, 136], including reductive dissolution via ascorbic acid, proton-promoted dissolution at low, and ligand-promoted dissolution using oxalate. Aggregate size was controlled experimentally through suspensions fractionation via gravitational settling. Complementary characterization and dissolution studies thereby allowed comparison of mass-normalized reactivity for different sizes of aggregates under otherwise identical experimental conditions. Characterization of aggregates included suspension stability measurements via sedimentation rates, as well as *in situ*

characterization of aggregate size and morphology using cryogenic transmission electron microscopy and atomic force microscopy. In addition to experimentally varying aggregate size, reactivity was also examined as a function of aggregation mechanisms. Nanohematite aggregation was induced by increasing ionic strength (i.e., larger aggregates), while also comparing non-dried suspensions (i.e., smaller aggregates) to those generated from dispersion of dry hematite powders. Finally, to explore the generality of results obtained here, the relationship between aggregation and interfacial reactivity (i.e., reductive dissolution) was also explored for several other iron oxides including nanoparticulate ferrihydrite, as well as goethite nanorods and microrods.

3.3 Experimental methods

3.3.1 Reagents. All experiments utilized ACS grade reagents or better. Iron oxide syntheses were performed using ferric nitrate nonahydrate (Fisher; 100%). Background electrolytes were comprised of sodium chloride (Fisher;100%) or sodium perchlorate (Fisher; 97%). L-ascorbic acid (Sigma Aldrich; ≥99%) was used for reductive dissolution, sodium oxalate (Fisher; 99%) was utilized in ligand-promoted dissolution, and hydrochloric acid (Fisher; 37%, trace metal grade) was used for proton-promoted dissolution. Hydrochloric acid was also utilized for complete acid digestion of suspension samples. Colorimetric analysis of total dissolved iron (FeTOT) and dissolved ferrous iron (Fe(II)) used hydrochloric hydroxylamine (Sigma Aldrich, 99%), ammonium fluoride (Fischer; 99.5%), a buffer prepared from ammonium acetate (Sigma Aldirch; ≥98%) and glacial acetic acid (Sigma Aldrich; ≥99%) and 1,10-phenanthroline (Sigma Aldrich; ≥99%).

3.3.2 Iron oxide synthesis. Two sizes of hematite (8 and 40 nm) were synthesized according to the procedures described in Lanzl et al. [136]. In our earlier work, we employed dried powders of each nanoscale hematite (i.e., air-dried 8 nm particles and freeze-dried 40 nm particles). Here, we also prepared a batch of each size without drying [(i.e., “non-air-dried” (NAD 8 nm) and “non-freeze dried” (NFD 40 nm)]

in an analogous manner. Briefly, after hematite suspensions were synthesized, they were subsequently cooled and placed into dialysis bags for purification (3-4 d, water changed 3 times daily), and then stored as a suspension for use in subsequent reactivity experiments.Samples of non-dried suspensions of hematite were acid digested to determine the total iron concentration in each suspension, and the suspensions were subsequently diluted as needed for dissolution.

Three other iron oxides were also synthesized for established methods. Ferrihydrite was synthesized according to Anschutz and Penn [60], which produces 6-line ferrihydrite roughly 6 nm in diameter. Goethite nanorods were synthesized according to Burleson and Penn [150], and the material characteristics have been previously reported in our earlier work [59, 84]. Larger goethite microrods were also produced following the procedure of Schwertmann and Cornell [118], which involved combining 90 mL of 5 M KOH and 50 mL of 1 M $Fe(NO_3)_3$ in a polyethylene Nalgene bottle, diluting with DI water to a total volume of 1 L, and then baking the solution mixture at 70°C for 60 h. The sediment was then centrifuged, washed three times, and dried.

3.3.3 Characterization of iron oxide powders. Iron oxides were characterized by X-ray diffraction (RigakuMiniFlex II X-ray with Co Kα source). Specific surface areas of all powders were measured with N_2 BET adsorption isotherm (Quantachrome BET Nova 4200e). Powder samples were outgassed overnight at 110 °C preceding N_2 gas adsorption. Transmission electron microscopy (JEOL 2100F TEM) was used to examine the size and morphology of synthesis products. TEM grids (holey carbon, Ted Pella Inc.,CA) were dipped into 0.5 g/L iron oxide suspensions, dried, and imaged. Average particle sizes were determined from measurements of 100-200 particles for each hematite, using the program Image J.

3.3.4 Size fractionation of iron oxide aggregates via gravitational settling. Iron oxide suspensions (0.5 g/L) were prepared by adding 17.5 mg of dry iron oxide powder to35 mL of 25 mM NaCl. The suspension, prepared in an amber, screw-cap vial

(40 mL nominal volume), was then adjusted to pH 3 with 5 M HCl. Suspensions were mixed (Cole Parmer Roto-Torque) end-over-end (60 rpm) for at least 2 h prior to fractionation to allow aggregation to achieve a steady state. Prior to gravitational settling, 1 mL of well-mixed suspension was removed and subsequently digested in strong acid to quantify the total amount of iron (as oxide) initially present in suspension.

To initiate size fractionation, vials were vigorously shaken by hand to ensure sufficient suspension dispersion and then promptly placed on a bench top without perturbation to allow for gravitation settling. Periodically (typically after 1, 10, 15, 40 or 90 minutes of settling time), the top-half of the suspension (by volume; 17 mL) was removed carefully from the vial via volumetric pipet. This "light fraction" of the suspension (i.e., the most stable aggregates least prone to settling) was then placed in a separate vial for use in subsequent reactivity studies. Accordingly, the remaining, lower half of the suspension was labeled as the "heavy fraction", corresponding to the least stable aggregates in suspension that settled out more quickly. Samples (0.5 mL) of each suspension fraction were then removed for digestion and total iron analysis.

In a limited number of instances, the extent of iron oxide aggregation was altered by varying ionic strength. Suspensions (0.5 g/L) were prepared in 1 M $NaClO_4$ to induce aggregation and subsequently used in reactivity studies without any further fractionation via gravitational settling. For high ionic strength suspensions, an increase in aggregation was inferred from greater rates of suspension settling during sedimentation studies for high ionic strength suspensions relative to lower ionic strength (the standard 25 mM NaCl used in all fractionated suspensions).

3.3.5 Aggregate characterization. *In situ* analysis of aggregates was conducted most extensively with hematite nanoparticles obtained from suspension fractions collected after extensive (40 minutes) gravitational settling. The light fractions of these hematite suspensions were analyzed via cryogenic-TEM (cryo-TEM; JEOL JEM 1230 with Gatan626 cryo-transfer system). Briefly, a drop of well-mixed suspension was

placed on a TEM grid and immediately immersed into liquid ethane to freeze aggregates in their native state and form amorphous (TEM penetrable) ice. The sample grid was then placed into a cryogenic TEM sample holder (-150 °C) for imaging. For comparison, diluted (e.g.,~0.05 g/L) suspensions of non-air dried (NAD) 8 nm and non-freeze dried (NFD) 40 nm hematite were also analyzed with cryo-TEM, as these suspensions exhibited comparable stability (via sedimentation studies) to that of the most stable hematite suspension fractions.

The heavy fraction of the 40 minute gravitational settling could not be imaged via cryo-TEM due to the extensive aggregation. To overcome the these challenges posed by their large aggregate size, we employed an approach in which scanning electron microscopy (Hitachi S-3400N SEM) images were collected on suspension samples that were prepared via freeze-drying. To eliminate salt effects suspensions were prepped in DI water (controls indicated rates of gravitational settling were equivalent in DI water and 25 mM NaCl). After fractionation, several small (~10 μL) droplets of suspensions were placed on an SEM stub. The stubs were immediately transferred into a -80 °C freezer for ~15 minutes. The frozen droplets on the SEM stub were then quickly transferred to a freeze-dryer, and the sample chamber was placed on a bed of dry ice during freeze drying to keep the suspension droplets frozen. After the ice was sublimated away (~0.5- 1 h) the samples were removed from the freeze-dryer and imaged.

3.3.6 Reductive dissolution studies with fractionated suspensions of iron oxide aggregates. Suspension fractions (i.e., time resolved light and heavy fractions) were reacted with excess ascorbic acid (10 mM) in reactors covered in aluminum foil to omit light. Use of excess concentrations of ascorbic acid ensure that dissolution rates are independent of reductant concentration and reflect mineral surface reactivity [40, 124] to ensure dissolution rates were independent of mass loadings effects.

After gravitational fractionation and prior to addition of ascorbic acid, 1 mL sample was collected to measure any initial background level of total dissolved iron

(TOTFe) and dissolved ferrous iron (Fe(II)), both of which were operationally defined to include all material passing through a0.2 µm Nylon filter (Tisch Scientific). A small amount (0.5 mL) of a concentrated ascorbic acid stock (0.3 M prepared daily), was then added to each of the reactors. Reactors were mixed end-over-end and suspensions samples were removed periodically over the course of 3 h for analysis of dissolved FeTOT and Fe(II) via standard colorimetric techniques [121, 122], as described below.

Experiments were conducted in triplicate for each suspension fraction. For comparison, reductive dissolution experiments with L-ascorbic acid were also performed in triplicate on a non-fractionated (0.5 g/L) suspension prepared from dry powder of all iron oxides, as well as suspensions of NAD 8 nm hematite, NFD 40 nm hematite, and select iron oxide suspensions where aggregation was induced via increasing ionic strength. For non-dried oxide, stock suspensions were diluted in appropriate buffer and electrolyte solution to obtain an equivalent amount of total iron (0.5 g/L as oxide) as that in suspensions prepared from powder.

3.3.7 Non-reductive dissolution studies with non-fractionated suspensions of iron oxide aggregates. Non-reductive dissolution mechanisms (i.e., ligand-promoted and proton-promoted) were also explored. Non-fractionated suspensions of 0.5 g/L 8 nm hematite powder were suspended in 25 mM NaCl and 1 M $NaClO_4$. Sedimentation tests (described in Chapter 2 [136]) were performed on each suspension to verify ionic strength induced aggregation in 1M $NaClO_4$compared to 25 mM NaCl. Proton promoted dissolution was performed at pH 2 by addition of HCl to each reactor. Ligand-promoted dissolution experiments utilized 1 mM sodium oxalate with reactors adjusted to pH 3. Samples were removed periodically over 4h for oxalate-promoted dissolution and 7d for proton-promoted dissolution.

3.3.8 Analysis of dissolved iron concentrations. Colorimetric analysis of total dissolved iron (FeTOT) concentrations involved initially reducing samples with hydrochloric hydroxylamine. For dissolved ferrous iron (Fe(II)) analysis, ammonium

fluoride was added to samples to minimize analytical interference from Fe(III). An buffer of ammonium acetate and glacial acetic acid was then added to both FeTOT and Fe(II) samples, followed by 1,10-phenanthroline to produce visible color in the presence of ferrous iron [121, 122]. Additional analytical details can be found in our earlier work [136].

3.3.9 Quantification of dissolution rates. Linear regression analyses were performed on dissolved Fe(II) concentrations measured over time, representative data for which is shown in Figure 3-1 for both a light and heavy suspension fractions (after 10 min of settling) prepared from 8 nm hematite. Accordingly, the slope of the best fit linear regression line represents the Fe(II) dissolution rate (d[Fe(II)]/dt) arising from reduction with Fe(II) detachment from the surface as the rate limiting (i.e.; slowest) step in the dissolution process [141]. To allow for comparison between suspension fractions, these dissolution rates were then normalized by the total amount of iron mass present in suspensions, which was determined via acid digestion and subsequent colorimetric analysis of TOTFe [121, 122]. Hereafter, we refer to these mass normalized dissolution rates as r_M values.

We note that in all dissolution experiments, a small, initially rapid release of Fe(II) was consistently observed upon addition of ascorbic acid (best seen from the non-zero y-intercept of dissolution curves in Figure 3-1). In all suspensions and suspension fractions, the amount of iron in this initial release equated to ~0.5% of the total mass in suspension. We attribute this to a small fraction of amorphous or highly reactive sites (e.g., defects) on the hematite that was rapidly reduced by ascorbic acid. As such, this initially rapid dissolution rate was excluded when calculating the r_M values we report below.

3.4 Results and discussion

3.4.1 Iron oxide powder characterization. Characterization of all powders was consistent with expectations from prior reports [59, 60, 84, 136]. For hematite, as we described previously [136], smaller hematite nanoparticles have an average diameter of 8.1 (±) nm and the larger hematite particles have diagonal length of 39.5 (± 7.9) and 29.2 (± 5.4) nm; henceforth referred to as 8 nm and 40 nm, respectively. Surface area analysis for 8 and 40 nm hematite indicated a total surface area (from dry powder) to be approximately 80 m^2/g and 40 m^2/g, respectively. While not as extensively characterized, goethite nanorods (roughly 100 nm by 10 nm; 110 m^2/g from BET) and microrods (roughly 700 nm by 400 nm; 40 m^2/g from BET) were consistent with earlier reports [84]. In agreement with Anschutz and Penn [60], 6-line ferrihydrite was roughly spherical, approximately 5 nm in diameter, with a BET specific surface area of 250 m^2/g.

3.4.2 Hematite suspension fractionation via gravitational settling. Figure 3-2 shows results of gravitational settling experiments for 8 and 40 nm hematite aggregates. Specifically, it shows how the fraction of total hematite mass changes as a function of time in the light and heavy fractions derived via gravitational settling. For each time point in Figure 3-2, there are corresponding fractions of mass for both the light (bottom curves) and heavy (top curves) aggregate fractions, with the sum of the mass from both fractions equaling unity. As expected, with increasing duration of settling, the mass remaining in the light fraction diminishes (to minima of 2-5% of total mass after 40 min), while the majority of mass concentrates in the heavy fraction (to maxima near 95-98% after 40 min) as more aggregates settle out of suspension. Notably, and consistent with our prior work [136], suspensions of 8 and 40 nm nanohematite settled, and fractionated on the basis of mass, almost equivalently. Such similarities in sedimentation rates and fractionation imply that aggregates generated from powders of 8 and 40 nm nanohematite form similar aggregates under the given conditions (pH 7, 25 mM NaCl). Aggregation is

extensive in both suspensions, as 90% of total hematite mass settles out of solution within ~5 minutes for both particle sizes.

3.4.3 Characterization of hematite aggregates in suspension fractions.

Aggregate settling is a net product of opposite forces, buoyancy and gravity, acting on one another, where forces can be affected by size, shape, and porosity of aggregates [151, 152]. Initial attempts to characterize the relative size of aggregates in suspension fractions via dynamic light scattering were limited by the extensive degree of aggregation and rapid rate of settling in suspensions prepared from dry nanohematite powders. Typical hydrodynamic diameters obtained from DLS were invariant with degree of suspension fraction, presumably because the analysis failed to capture the largest of aggregates in heavier fractions because their rates of settling were on the order of the timescale necessary for analysis.

Imaging proved best for obtaining semi-quantitative information on aggregate size as a function of suspension stability [151]. Representative cryo-TEM images of aggregates suspended in the lightest hematite fractions (the remaining 5% of hematite mass stable after 40 min of settling) of 8 and 40 nm hematite are presented in Figure 3-3. Even in these most stable suspension fractions, for which rates of sedimentation were essentially negligible, both 8 and 40 nm hematite particles existed as aggregates on the order of 50 to 200 nm in size exhibiting a range of aggregates structure, density and morphology. In fact, monodisperse hematite nanoparticles of 8 and 40 nm were not observed during this analysis. Thus, in suspensions prepared from hematite powders, it appears the amount of truly monodispersed hematite nanoparticles will be limited, if not nonexistent.

Imaging of the corresponding heavy fraction (the more than 95% of total hematite mass that had deposited out of solution after 40 min of settling) proved more challenging due to the high concentration and large size of particles, which rendered analysis with cryo-TEM ineffective. Instead, we collected SEM images of suspension droplets that

were immediately frozen (T = -80 C) and subsequently freeze-dried to minimize the impact of drying on aggregate morphology (Figure 3-4). The heavy fraction 8 nm (Figure 3- 4a) and 40 nm (Figure 3-4b) suspensions after 40 minutes of settling exhibited a polydisperse mixture of aggregates. This included rather large aggregates, frequently exhibiting dimensions between 1.5 to 5μm. Indeed, in both 8 and 40 nm hematite suspensions, a considerable fraction of the total mass is tied up in aggregates that are often times several orders of magnitude greater than the characteristic dimensions of primary particles. Further, our assumptions regarding the primary mode of fractionation via gravitational settling (i.e., that greater rates of settling generally correlate to larger aggregate sizes, and vice versa) appear valid.

3.4.4 Influence of aggregate size on reductive dissolution of hematite. Trends in mass normalized rates of Fe(II) dissolution [r_M values (μM Fe(II) h^{-1} μM $TOTFe^{-1}$)] are shown in Figure 3-5a for different light and heavy suspension fractions (collected after 1, 5 and 40 min of settling) for 8 and 40 nm hematite suspensions. In Figure 3-5a, r_M values are plotted as a function of the fraction of the initial hematite mass present in each fraction (the corresponding duration of gravitational settling is noted). Data represent averages (with standard deviation) of at least triplicate experiments at each settling duration used to isolate and measure the dissolution activity of different sizes of hematite aggregates present in each fraction. For comparison, Figure 3-5b presents all r_M values (without averaging) measured for light and heavy fractions of 8 and 40 nm hematite suspensions after 1, 5 and 40 min of settling.

Dissolution rate data in Figure 3-5a and 3-5b reveal that the reactivity of aggregates generated from 8 nm hematite is remarkably constant for approximately the heaviest 95% of suspension mass. Only the smallest of aggregates comprising the lightest 5% of hematite mass exhibited an r_M value statistically greater (roughly four-fold) than that measured for other, heavier suspension fractions consisting of much larger aggregates. This slight increase in r_M with decreasing aggregate size is most easily

observed in Figure 3-5b for the entirety of our dataset. Thus, aggregation of 8 nm hematite particles appears to only modestly decrease reactivity per unit mass when monodispersed primary particles and the smallest of aggregates (<100 nm) coalesce into larger aggregates. It is also important to note that as aggregates continue to grow in size, even to the extremes observed via SEM characterization (see Figure 3-4), further inhibition of their mass-normalized dissolution rates is not observed. In fact, the suspension fraction with the largest aggregates (i.e., the heavy fraction collected after 1 min of settling) exhibited reactivity that was statistically indistinguishable from the light fraction collected at 5 min of settling, which consisted of considerably more stable and smaller aggregate sizes.

The same behavior was observed in suspensions of 40 nm hematite, yielding near constant mass normalized dissolution activity across all sizes of suspension fractions. Although it is tempting to suggest that the r_M value for the smallest suspension fraction is greatest, this difference in rate is increases are not statistically significant. Thus, for both 8 and 40 nm hematite, aggregation generally exerts little to no influence on the reactivity for the overwhelming majority of particles in suspension. This result is counter to conventional wisdom, which commonly assumes aggregation consumes reactive surface area. Even the four-fold greater reactivity observed for the lightest 8 nm suspension fraction is much less than would be expected from the difference in aggregate size determined from suspension characterization. For example, assuming spherical geometry, an increase in aggregate size from 100 nm to 1 μm, which reasonably approximates the range from light to heavy fractions, produces more than an order of magnitude decrease in specific surface area. While such a spherical approximation for aggregate morphology is certainly oversimplified, it emphasizes that even the instances where aggregate size influences reactivity defy expectations.

We note that results from two types of control experiments ensured that trends in reactivity in Figure 3-5 truly reflect the influence, or lack thereof, of aggregate size. First,

doubling ascorbic acid concentration (20 mM) in both the heavy and light suspension fractions had no bearing on Fe(II) production rates. Thus, all experiments were conducted in a regime of excess ascorbic acid where dissolution rates were essentially independent of reductant concentration and controlled by the rate of surface reduction (i.e., all surfaces in suspensions were saturated with adsorbed ascorbate). Further, a series of complementary studies were conducted using suspensions prepared from hematite powders across the range of mass loadings encompassing those achieved through gravitational settling (from 0.05 to 0.95 g/L). For all mass loadings, reaction with 10 mM ascorbic acid yielded equivalent mass normalized rates of Fe(II) production, suggesting that differences in the ratio of hematite-to-ascorbic acid across different suspensions exerted little influence on r_M values [153].

3.4.5 Influence of aggregation on trends in size-dependent hematite nanoparticle reactivity. In previous work [61, 136], 8 nm hematite suspensions have consistently exhibited greater reactivity than 40 nm hematite suspensions (by roughly a factor of 5) during reductive dissolution by ascorbic acid. Here, we find this degree of reactivity enhancement is maintained across all aggregate sizes, with all sizes of aggregates formed in 8 nm hematite suspensions being consistently 6-fold more reactive toward reductive dissolution than the corresponding suspension fraction for 40 nm hematite. Due to the near identical matter in which their suspensions fractionate, the consistent magnitude of rate enhancement across aggregates of 8 nm and 40 nm particles perhaps should be expected.

The near uniform reactivity for aggregates of all sizes in 8 and 40 nm hematite suspensions is best illustrated in Figures 3-5c and 3-5d, in which mass normalized rates measured for each suspension fraction [r_M(fraction)] are divided by the mass normalized dissolution rate measured for a non-fractionated suspension (r_M(bulk); i.e.,0.5 g/L of 8 or 40 nm hematite prepared from powder). From this analysis, nearly 95% of the mass in aggregated 8 and 40 nm hematite suspensions exhibits the same reactivity as the bulk

suspension, (i.e., a value of r_M(fraction)/r_M(bulk) equal to unity, which is shown as the dashed line in Figures 3-5c and 3-5d)

Finally, for 8 nm suspensions, we note that the four-fold enhanced reactivity of the smallest aggregates is not significant enough to alter bulk suspension reactivity. Specifically, in experiments with non-fractionated hematite suspensions, the four-fold enhanced reactivity of the lightest 5% of mass is overwhelmed by the slightly slower dissolution activity of the remaining 95% of the hematite mass. This observation runs counter to hypotheses put forth by Echigo et al. [61], who stated that the greater reactivity of their 7 nm hematite relative to their larger particle analogue (30 nm hematite) resulted from preferential dissolution of monodisperse nanoparticles in the 7 nm hematite suspension. Based on our findings, it appears that the greater, mass-normalized reactivity of smaller hematite nanoparticles can be achieved in extensively aggregated suspensions.

3.4.6 Influence of aggregate size on the reductive dissolution of ferrihydrite, nanorod goethite and microrod goethite. Similar gravitational fractionation (Figure 3-6) and reductive dissolution (10 mM ascorbic acid) experiments were performed with suspensions prepared from powders of nanoparticulate ferrihydrite and two sizes (i.e., nanorods and microrods) of goethite. Mass-normalized Fe(II) dissolution rates as a function of suspension mass fraction are shown in Figure 3-7 for all iron oxides (data for 8 and 40 nm hematite are included for comparison). Data are shown for all oxides in order from greatest (top; ferrihydrite) to least (bottom; 40 nm hematite) dissolution activity. Dashed horizontal lines represent the mass-normalized reactivity of the non-fractionated bulk suspension for each oxide phase, provided for comparison. Although not as rigorously explored for ferrihydrite and goethite suspensions, it was assumed that gravitational settling yielded larger aggregates in heavy suspension fractions relative to the corresponding light fractions.

As expected, ferrihydrite was the phase most prone to reductive dissolution, behavior often attributed to its amorphous structure [24, 40], while microrod and nanorod

goethite were slightly less reactive than 8 nm hematite. As observed for hematite, unexpectedly all suspension fractions exhibited near equivalent r_M values, regardless of aggregate size. Thus, independence of mass-normalized dissolution rates with respect to aggregation state appears generally applicable for most iron oxides during reductive dissolution via ascorbic acid.

3.4.7 Influence of aggregation via drying on hematite stability and reactivity. Additional reactivity studies were conducted to assess the influence of aggregation when induced by mechanism other than drying. Specifically, the extent of hematite aggregation was manipulated by considering the behavior of non-dried stock suspensions of 8 and 40 nm hematite, as well as by using high ionic strength to further increase the extent of aggregation in suspensions prepared from nanopowders.

Sedimentation tests confirmed that suspensions of non-air-dried (NAD) 8 nm hematite and non-freeze-dried (NFD) 40 nm hematite were incredibly stable, remaining well suspended for several days in 25 mM NaCl at pH 3 (shown in Figure 3-8). Due to their stability, gravitational settling was not used to further size-fractionate these suspensions. Even though well suspended, cryo-TEM images reveal aggregates of NAD 8 nm (Figure 3-9) hematite anywhere between 20 to 400 nm in size, which is on the order of those encountered in the lightest suspension fraction of the 8 nm powder (50- 200 nm). Dispersed nanoparticles and small aggregates (up to ~600 nm) are also observed in the NFD 40 nm suspension (Figure 3-9). It is important to note that aggregates of both NAD 8 nm and NFD 40 nm hematite appear to be more loosely packed, with a fractal structure that may expose greater amounts of their surface area.

Mass-normalized reductive dissolution rates (10 mM ascorbic acid, pH 3) are included in Figure 3-7 for NAD 8 nm and NFD 40 nm hematite, allowing direct reactivity comparison of dried powders and non-dried stock suspensions. Although suspensions of NAD 8 nm hematite were about 1.8 times more reactive on average than the bulk 8 nm suspension prepared from powders (production rates of 6.0 (±1.5) $\times 10^{-3}$ and 3.3 (±0.7)

$\times 10^{-3}$μM Fe(II) hr^{-1} μM $FeTOT^{-1}$, respectively), the NAD 8 nm suspension is less reactive per unit mass than the smallest aggregates prepared from powders. Furthermore, the nearly 2-fold increase in reactivity for NAD 8 nm suspensions relative to the suspensions prepared from 8 nm powder is also far less than would be expected for such a disparity in aggregate size between these systems (i.e., an order of magnitude greater surface area for 100 nm aggregates compared to 1 μm aggregates).

Results with NFD 40 nm hematite further imply that the extent of aggregation has little to no impact on rates of reductive dissolution mediated by ascorbic acid. Reactivity of NFD 40 nm hematite was equivalent to non-fractionated 40 nm hematite powder with mass normalized Fe(II) productions rates of 6.6 (±1.5) $\times 10^{-4}$ and 6.6 (±3.2) $\times 10^{-4}$ μM Fe(II) h^{-1} μM $TOTFe^{-1}$, respectively. This behavior is entirely consistent with that observed for size-fractioned hematite suspensions shown in Figure 3-5.

3.4.8 Influence of aggregation via ionic strength on hematite stability and reactivity. Aggregation was also induced by increasing ionic strength in suspensions with 1 M $NaClO_4$ for 8 nm hematite powder, NAD 8 nm, ferrihydrite, and goethite nanorods. Sedimentation tests with each oxide phase confirmed faster settling times for suspensions in 1 M $NaClO_4$ relative to those prepared in 25 mM NaCl (Figure 3-8), consistent with larger aggregates induced by high ionic strength settling out of suspension faster. We note that the high concentration of salt limited ability to image particles in situ with microscopy. Further, ionic strength was varied using 1 M $NaClO_4$ because high concentrations of Cl^- are thought to increase dissolution rates.[123] Additional experiments conducted with suspensions in 25 mM $NaClO_4$ exhibited equivalent reactivity to dissolution experiments with 25 mM NaCl, thereby allowing comparison between the different electrolyte systems.

Results from these aggregated suspensions at high ionic strength are included in Figure 3-7, data represented by open symbols indicate results collected in suspensions with 1 M $NaClO_4$. Despite increasing ionic strength inducing aggregation, the mass

normalized dissolution rates from suspensions of ferrihydrite, 8 nm hematite powder, and NAD 8 nm hematite in 1 M $NaClO_4$ were statistically equivalent to their lower ionic strength (25 mM NaCl) counterparts. Once again, evidence suggests that aggregation has little impact on the reduction of iron oxides by ascorbic acid, a result that may be more broadly generalizable for other redox processes.

Nanorod goethite was the only iron oxide that showed a statistically significant decrease in reactivity with increasing ionic strength. Although nanorod goethite reductive dissolution decreased by a factor of 1.7 (±0.1) in 1 M $NaClO_4$, this decrease is considerably less than that observed by Rubasinghege et al. [64], which reported complete quenching of proton-promoted dissolution for nanorod goethite at pH 1 and at high ionic strength ($0.1NHNO_3$). Accordingly, they attributed the inhibition of dissolution to the loss of reactive surface area resulting from the dense aggregates formed at high ionic strength. The contrast in our results to those of Rubasinghege et al. [64] may indicate that the magnitude of inhibition exerted by nanoparticle aggregation may be a function of the interfacial processes, specifically in our case the mode of iron oxide dissolution.

Indeed, we believe the modest to negligible influence of aggregation on r_M values, which runs counter to conventional wisdoms, may be specific to reductive dissolution, and more generally redox processes, on hematite and other iron oxides. We explored this hypothesis through a limited number of complementary studies on non-reductive dissolution processes. Recall, that for suspensions prepared from 8 nm hematite powder, r_M values for ascorbic acid mediated reductive dissolution were equal at 25 mM NaCl and 1 M $NaClO_4$. However, rates of oxalate- and proton-promoted dissolution (pH 2), both of which are non-redox processes, were roughly 1.5-fold greater in 25 mM NaCl relative to 1 M $NaClO_4$ (Figure 3-10) for suspensions of 8 nm hematite powder.While this magnitude of rate decrease may seem small, we emphasize that the oxalate and proton-promoted dissolutions systems represent the only instances in which dissolution

rate and extent (see Figure 3-10) decreased in response to aggregation induced by ionic strength. This decrease in dissolution rate is also reasonable for the degree of believed aggregation induced by increasing ionic strength. Recall that suspensions prepared from 8 nm hematite powder were already rather extensively aggregated, and sedimentation rates (Figure 3-8) only increased by roughly a factor of 2 in systems with 1 M NaO4Cl. Thus, while further work is most certainly needed, all evidence herein supports non-reductive dissolution processes being more sensitive to aggregation than reductive dissolution processes.

There are many possible explanations for this behavior, including the possibility that reductive and non-reductive dissolution processes initiate at different sites on the hematite surface, and these sites may be affected uniquely by aggregation. Alternatively, we propose that this behavior may relate to the semiconductive nature of hematite [26, 85]. Yanina and Rosso [85] demonstrated that potential gradients across a hematite are great enough for electrons to flow from one crystal plane to another via bulk crystal conduction. Furthermore, it has been suggested that electron transfer between semiconductive particles (e.g., TiO_2) within an aggregate can occur, a process commonly referred to as the "antenna effect" [154]. Finally, it has been extensively demonstrated [26, 86, 87, 155] that surface-associated Fe(II), which represents the product of ascorbic acid prior to release into solution, can reduce lattice Fe(III) via interfacial electron transfer, initiating the bulk conduction process. Given these observations, it is plausible that extensively aggregated hematite nanoparticles may undergo inter-particle electron shuttling, thereby allowing primary particles deep within the aggregate to still participate in the redox process. Thus, processes such as reductive dissolution would have greater "access" to these particles trapped within the aggregate, while non-redox active processes would be limited primarily to those reactive sites available on the external surface area of the aggregate.

3.5 Conclusion

This work provides a definitive example where nanoparticle aggregation exhibits no influence on the reactivity of nanoparticle suspensions. Indeed, and somewhat surprisingly, despite clear changes in the overall size of aggregates and across a range of aggregation mechanisms, rather large aggregates of 8 and 40 nm hematite (in excess of 1 μm) are as reactive per unit mass as smaller aggregates (on the order of 100 nm) and presumably even the monodispersed primary nanoparticles comprising the aggregates. We can conclude, therefore, that at least for the reductive dissolution of hematite and other iron oxides, the size-dependent reactivity most commonly associated with monodisperse nanoparticles is conserved during aggregation (i.e., aggregates reflect the reactive properties of the primary nanoparticles from which they are constructed).

There are broad and wide-ranging implications associated with this observation. In natural systems, for example, even when aggregated, iron oxide nanoparticles may still contribute disproportionately to a range of processes including surface-associated Fe(II) mediated pollutant transformation in the subsurface, photochemical ROS generation [93] in sunlit surface waters, and iron solubilization during atmospheric redox cycling [156]. Similarly, in the field of nanotoxicology, the observation that aggregation may not suppress dissolution may help better predict the contribution of metallic and metal oxide nanoparticles as sources of potentially toxic dissolved metals in the environment. Finally for engineering applications, there may be some engineered nanomaterials that are substantially better than others for processes reliant on their interfacial reactivity. Indeed, it would likely be advantageous to integrate nanomaterials less prone to the inhibitory effects of aggregation into devices and applications

From a more fundamental perspective, additional work regarding aggregate bulk reactivity in redox processes is merited. However, evidence presented herein suggests that interfacial redox processes on iron oxide nanoparticles are less susceptible to aggregation than other surface-promoted processes (e.g., dissolution by non-reductive

mechanisms). One scenario that could potentially explain such behavior is particle-to-particle charge transfer in densely packed aggregates. Such a phenomenon would allow hematite trapped deep in the interstices of aggregates to still participate in the charge transfer process initiating on the aggregate surface. As such, reactive surface area may be less critical to system reactivity, and in turn explain the limited influence of aggregation on these processes. Additional work is merited to distinguish such a possibility from other scenarios. For example, we cannot rule out that aggregates considered herein are nanoporous, and thus allow access to internal surface area in the aggregates via pore diffusion. We note, however, that mass transfer would likely limit reactivity in this case, which we do not believe is a limiting factor in the dissolution results presented herein.

Perhaps most importantly, this work illustrates that not all nanoparticles and nanoparticle aggregate are created equally. Thus, generalizations as to the impact of aggregation on nanoparticle reactivity may not be possible. Rather, it seems most appropriate that the influence of aggregation on reactivity be considered on a case-by-case basis, not only for different nanoparticles but also for different interfacial processes and different mechanisms for particle aggregation. Given the exceedingly large matrix of engineered and natural nanomaterials, as well as interfacial processes (e.g., adsorption, dissolution, electron transfer), these efforts will likely need to be prioritized for those nanomaterials of greatest practical importance with respect to their toxicity and possible use in commercial or industrial applications.

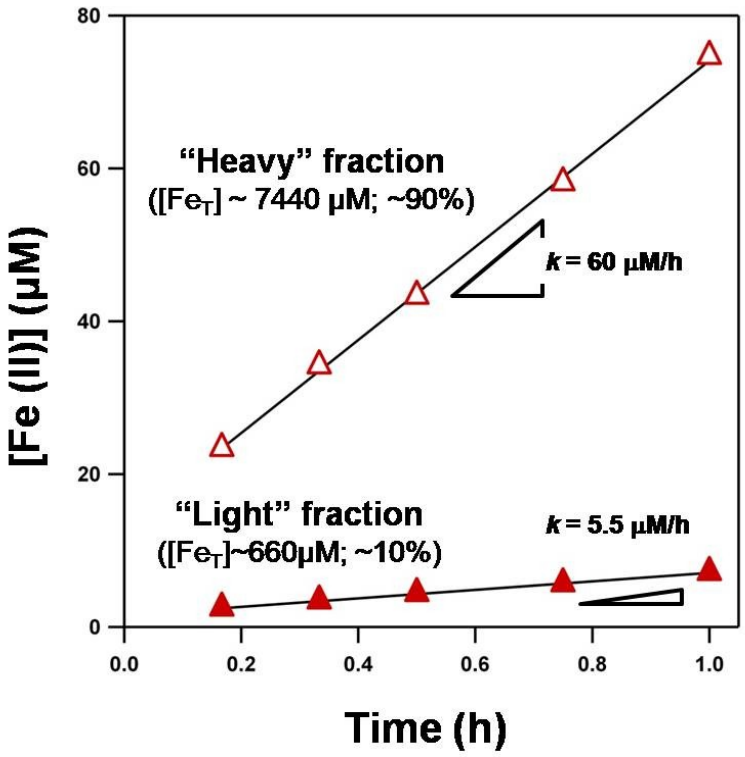

Figure 3-1. Examples of Fe(II) dissolution curves and dissolution rate analysis for 8 nm hematite. Data are shown for the heavy fraction (~ 7440 µM Fe_T) and light fraction (~ 660 µM Fe_T) obtained after 10 minutes of gravitational settling of a 0.5 g/L suspension. Dissolution rates were determined from the slope obtained via linear regression analysis (shown as solid lines) and then normalized by the total amount of iron measured in each fraction.

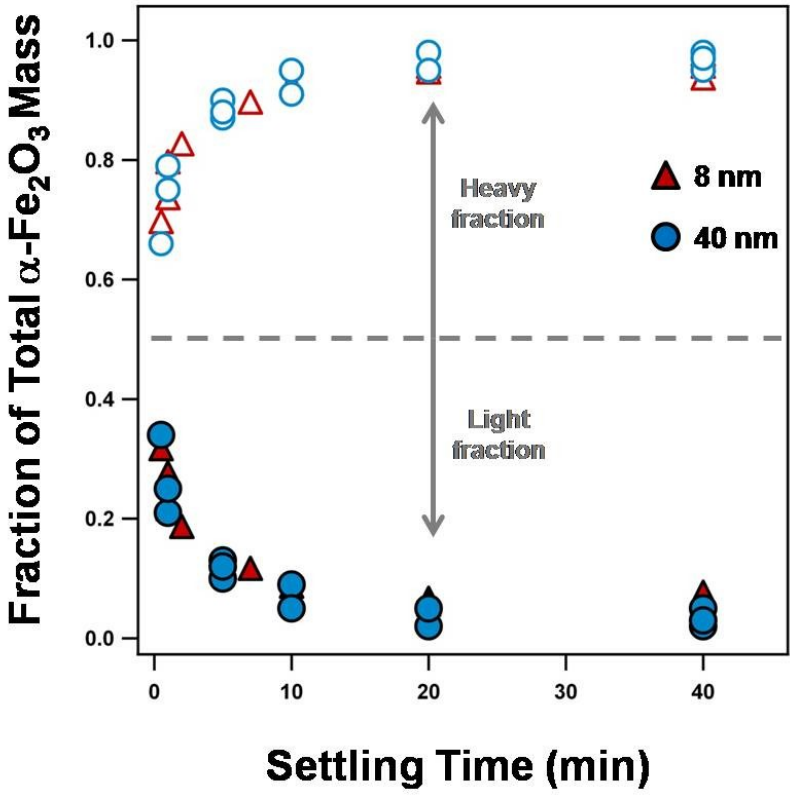

Figure 3-2. Fraction of total hematite mass present in light and heavy sediment fractions generated as a function of increasing settling time. Data are shown for initial suspensions (0.5 g/L, pH 3, 25 mM NaCl) prepared from powders of both 8 nm (red) and 40 nm (blue) hematite. For each settling time there is a representative point for both the heavy fraction (open markers) and light fraction (closed markers). The lightest fraction generated (with ≤ 5 % total hematite mass) was obtained after 40 min settling time, while the heaviest fraction (with 65-70 % total hematite mass) corresponded to the heavy fraction generated at the shortest duration of settling (1 min settling time).

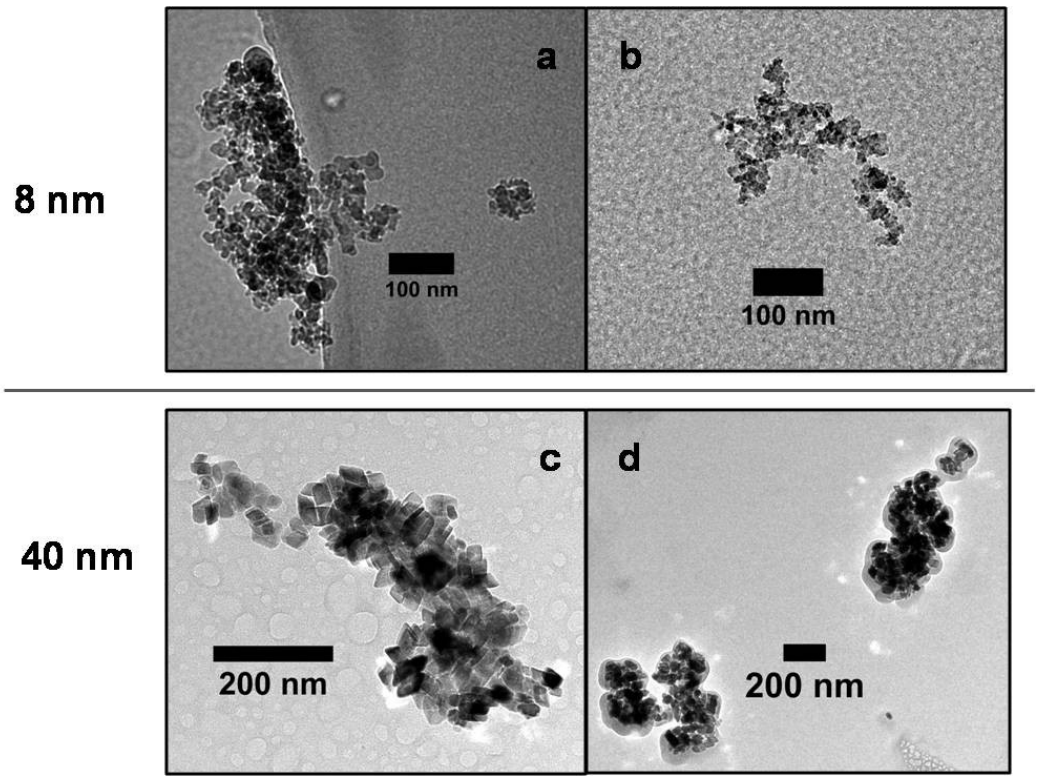

Figure 3-3. Cryo-TEM images of representative particles in the lightest fraction (stable after 40 min of settling) of 8 nm (a,b) and 40 nm (c,d) hematite suspensions. These particles comprise the lightest 5% of hematite mass present in suspension mass for each light fraction. Details of image collection and sample preparation are provided in the text.

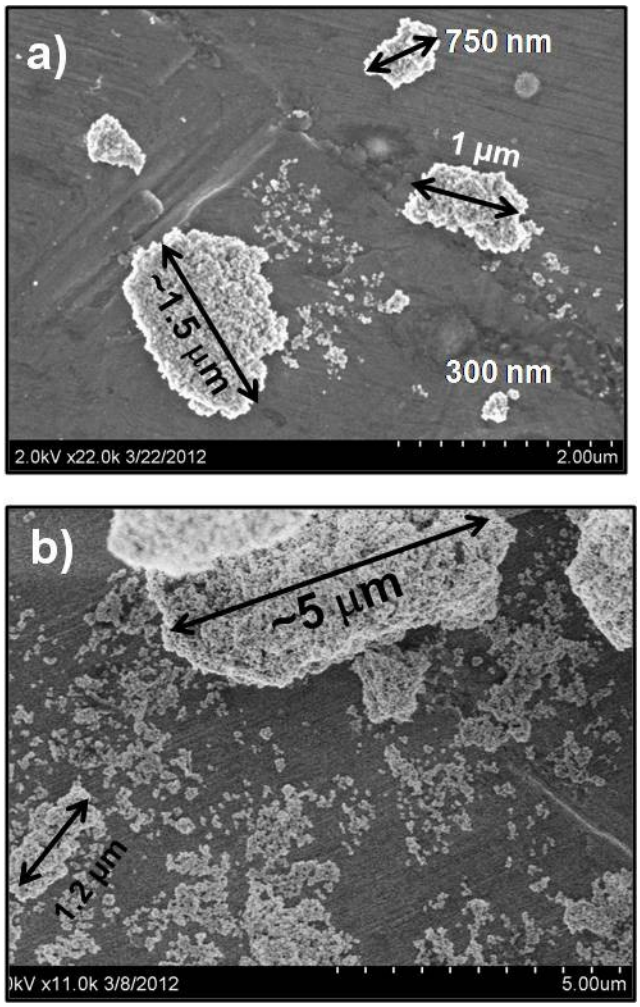

Figure 3-4. SEM images of aggregates present in the heavy fractions of (a) 8 nm and (b) 40 nm hematite suspensions, respectively. Particles represent those deposited out of solution after 40 minutes of settling, corresponding to the ~95% of the total hematite mass initially present in suspensions (0.5 g/L, pH 3, 25 mM NaCl). Details of image collection and sample preparation are provided in the text.

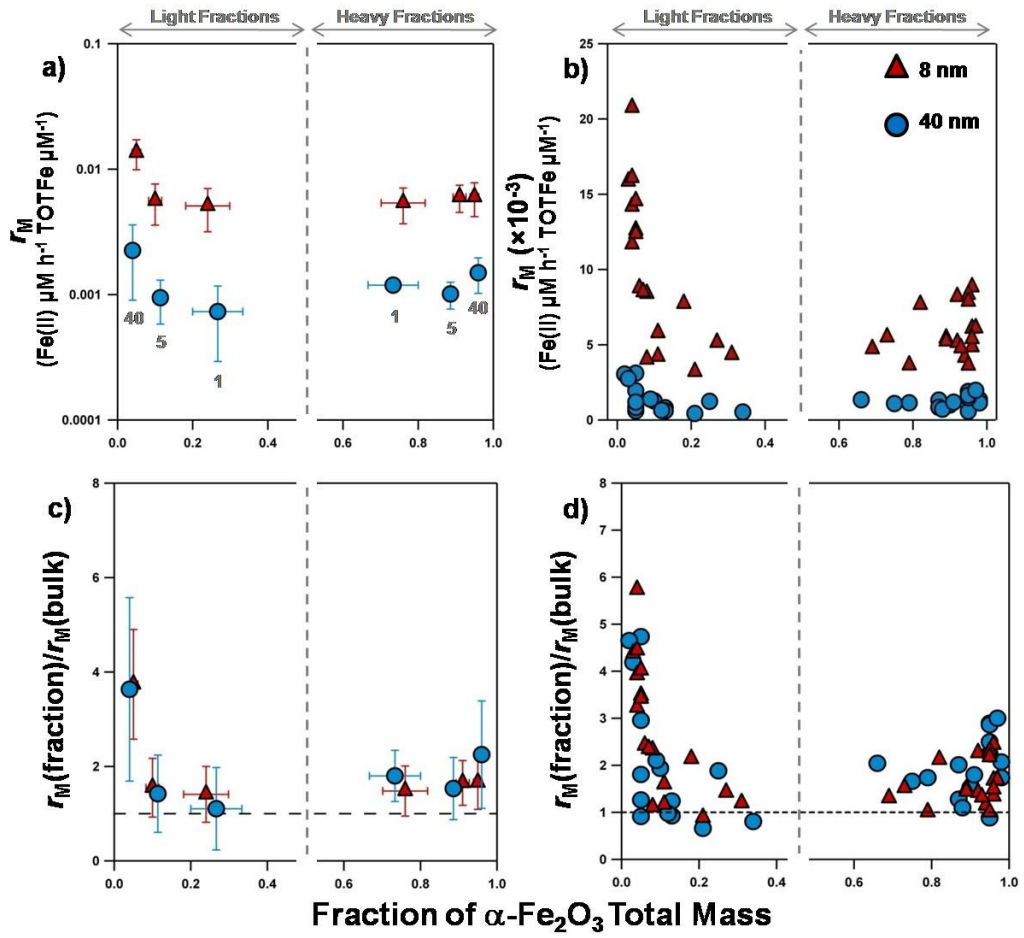

Figure 3-5. (a) Average r_M values as a fraction of mass available in gravity-separated fractions of 8 and 40 nm hematite. The numbers below each set of fractions corresponds to the settling time used to generate "light" (shown on the left) and "heavy" (shown on the right) fractions. (b) All r_M values measured for fractions of 8 and 40 nm suspensions. Data in (b) represent those values averaged in (a) at each settling time. (c) Average r_M values for suspension fractions [r_M (fraction)] normalized to r_M value measured for the bulk (i.e., non-fractionated) suspension [r_M (bulk)]. The horizontal dashed line represents a ratio of unity, indicating the reactivity of the suspension fraction is identical to that of the bulk 0.5 g/L suspension. (d) All data points shown for mass normalized rates of each fraction normalized to the rate of the bulk suspension

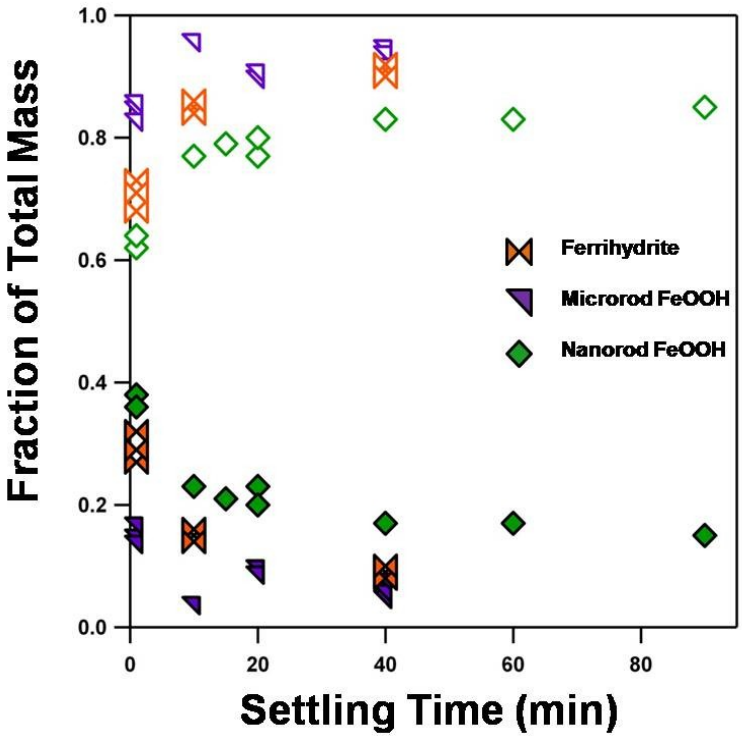

Figure 3-6. Fraction of total iron oxide mass present in light and heavy sediment fractions generated as a function of increasing settling time for goethtite microrods, goethite nanorods, and ferrihydrite. Data is shown for initial suspensions (0.5 g/L, pH 3, 25 mM NaCl) prepared from powders of both goethtite microrods (purple), nanorods (green) and ferrihydrite (orange). For each settling time there is a representative point for both the heavy fraction (open markers) and light fraction (closed markers)

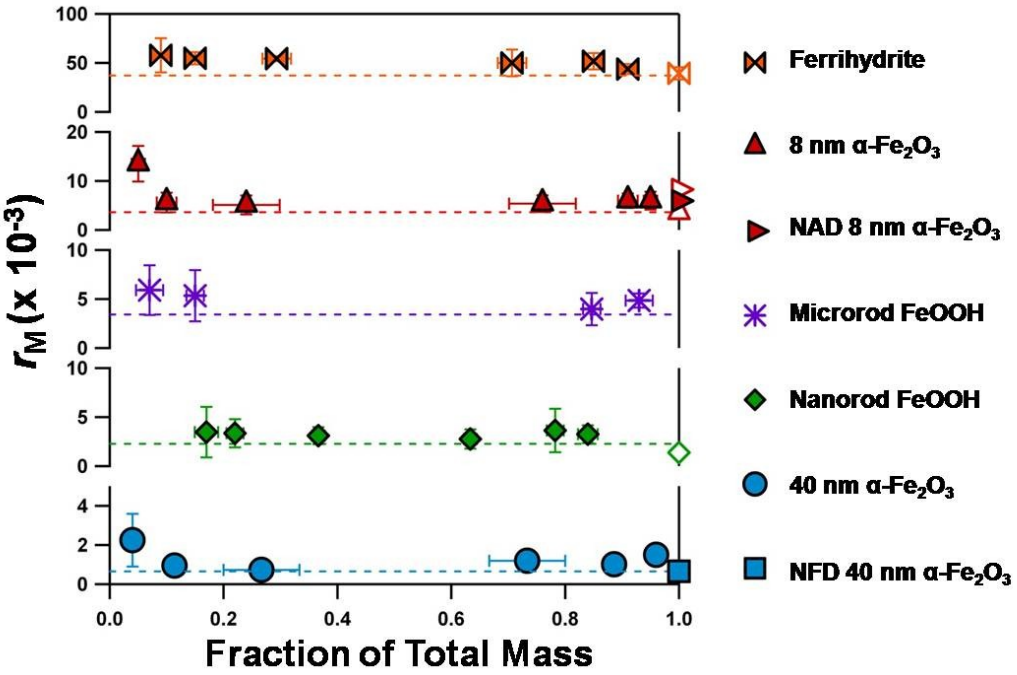

Figure 3-7. Average r_M values as a fraction of mass available in gravity-separated fractions the iron oxides considered herein (see key). Solid data points represent experiments conducted with10 mM ascorbic acid at pH 3 low ionic strength (25 mM NaCl) suspensions. Also shown are data collected in high ionic strength (1 M $NaClO_4$) suspensions (open symbols). For each oxide, the dashed horizontal line represents the r_M value measured in a bulk (i.e., non-fractionated) suspensions of each oxide. Uncertainties represent one standard deviation obtained from at least triplicate experiments.

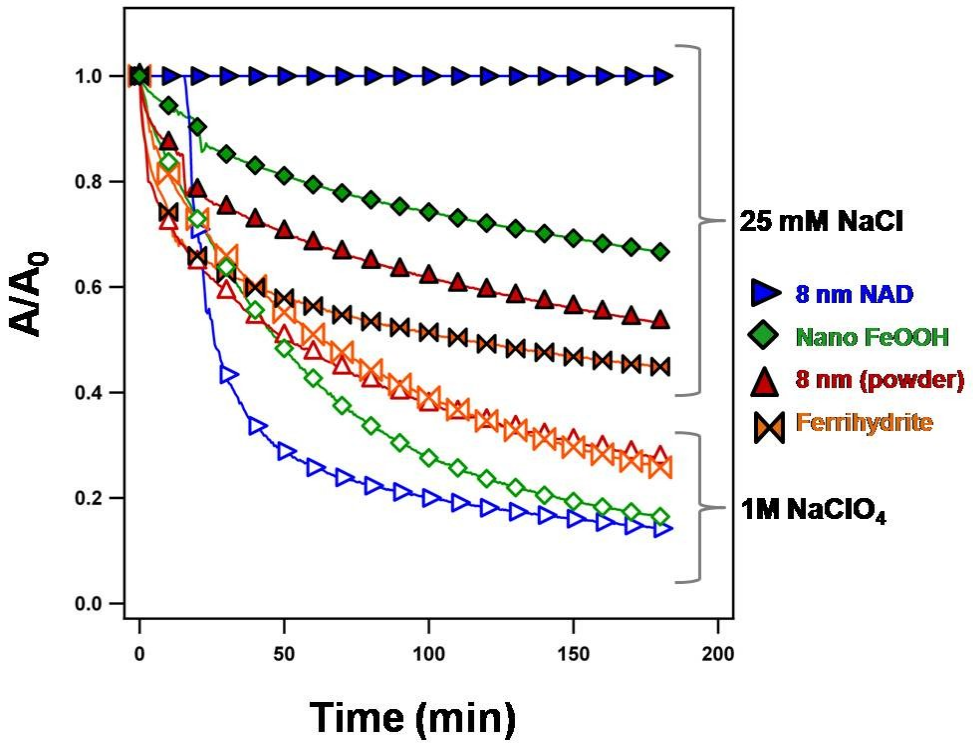

Figure 3-8. Sedimentation curves of normalized absorbance (A/A_0) at λ 510 nm for 0.5 g/L (or equivalent) suspensions of iron oxides at pH 3. Solid markers represent data for suspensions in 25 mM NaCl and open markers are data obtained at 1 M $NaClO_4$.

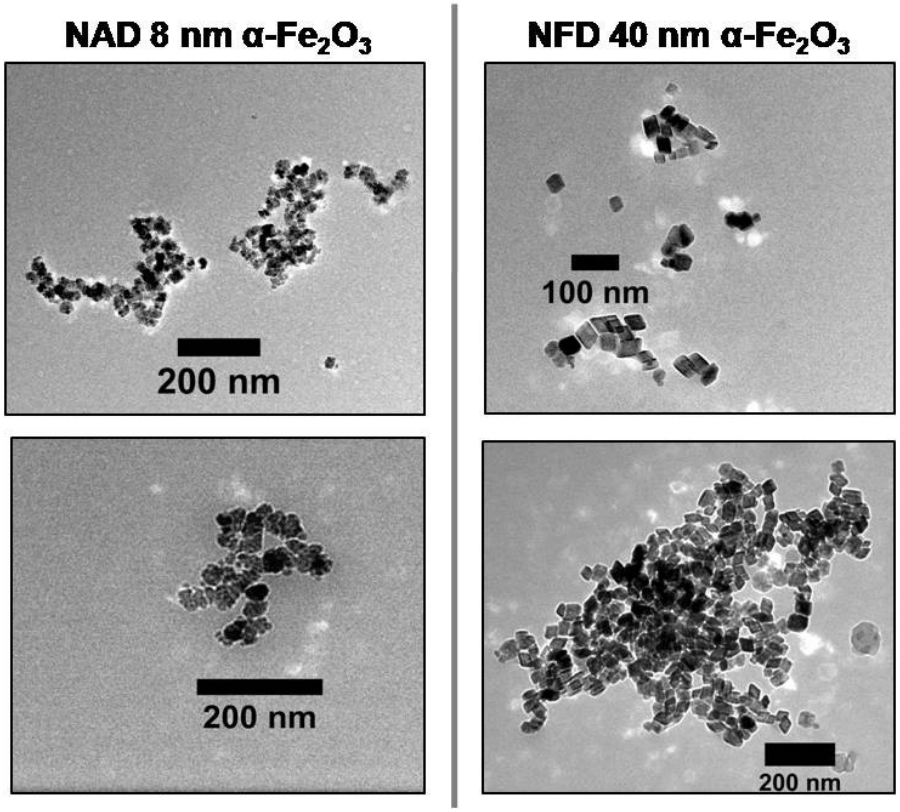

Figure 3-9. Representative cryo-TEM images of non-dried suspensions of 8 nm hematite (NAD 8 nm α-Fe_2O_3; left) and 40 nm hematite (NFD 40 nm α-Fe_2O_3; right).

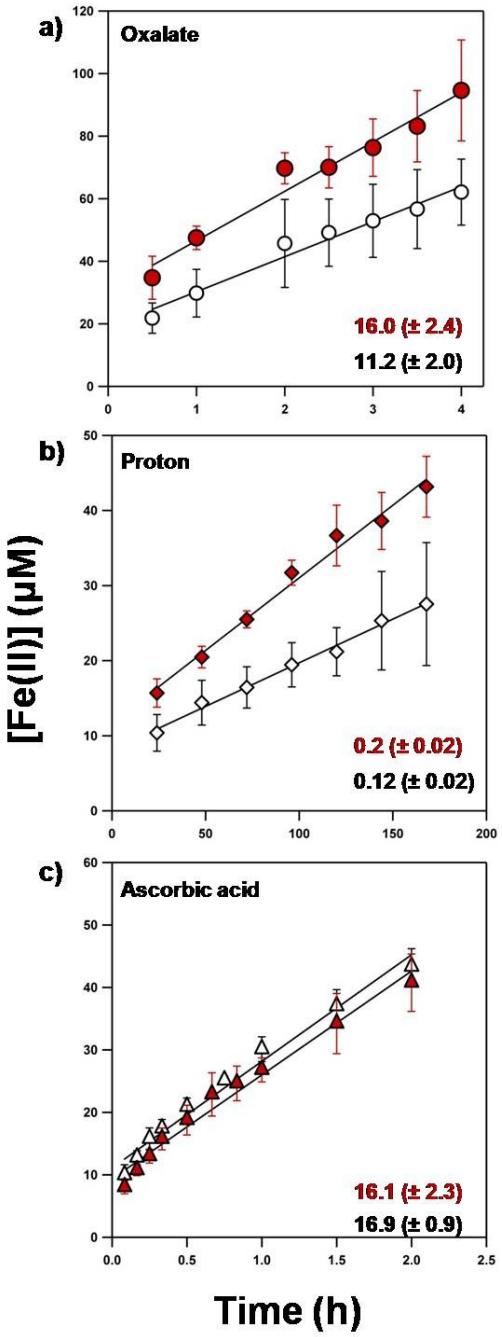

Figure 3-10. Dissolved Fe(II) production as a function of time for (a) oxalate-promoted dissolution, (b) proton-promoted dissolution and (c) reductive dissolution with ascorbic acid for suspensions (0.5 g/L) prepared from 8 nm hematite powder. Data represent average and standard deviations from triplicate experiments in 25mM NaCl (red solid symbols) and 1 M $NaClO_4$ (open symbols). Lines represent results of best-fit linear regression analyses from which r_M values were determined from the slope. These r_M values are provided. Oxalate (1 mM) and ascorbic acid (10 mM) mediated dissolution were conducted at pH 3.0, whereas proton promoted dissolution was conducted at pH 2.0.

CHAPTER 4
INFLUENCE OF HEMATITE PRIMARY PARTICLE SIZE ON DOM MEDIATED PHOTOREDUCTIVE DISSOLUTION: IMPLICATIONS FOR THE FENTON REACTION

4.1 Abstract

Primary particle size can influence the interfacial reactivity of iron oxides, yet most studies demonstrating such enhanced nanoparticle reactivity have focused on relatively simple systems and a single chemical process (e.g., adsorption, dissolution or electron transfer). However, the significance of such size-dependent activity remains unclear in more complex aquatic systems representative of nature where multi-step heterogeneous reactions are more likely to occur. Here, we examine the influence of iron oxide primary particle size on the generation of reactive oxygen species (ROS) via the heterogeneous photochemical Fenton reaction. The ability of two sizes of nanoscale hematite (8 and 40 nm α-Fe_2O_3) to generate hydroxyl radical (•OH) was studied in irradiated suspensions of Suwanee River Humic Acid (SRHA) as a function of pH (pH 3-5). At both pH values, suspensions of 8 nm hematite consistently outperformed 40 nm suspensions in all processes believed to be critical in •OH formation including sorption capacity for SRHA and rates of Fe(II) production via SRHA-mediated photoreductive dissolution. Accordingly, during irradiation with simulated sunlight ($\lambda > 305$ nm), 8 nm suspensions produced roughly 4-fold greater concentrations of steady-state •OH as determined by the decay of phenol, an organic probe for •OH. At higher pH values (pH 5), •OH generation was only measurable in 8 nm suspensions. Notably, these trends in •OH formation scaled closely with rates of Fe(II) dissolution measured in deoxygenated systems, consistent with hematite photoreduction and Fe(II) release into solution being a limiting step in •OH formation. Collectively, these results suggest that nanoparticulate

and colloidal iron oxides, as a result of their size-dependent reactivity and propensity to stay suspended in the water column over longer timescales, will produce more •OH than larger analogs, which has implications for the persistence of organic pollutants in sunlit surface waters.

4.2 Introduction

In surface waters, it is widely believed that soluble complexes and suspended forms of particulate iron (e.g., oxides) can impact pollutant fate via their participation in the photo-Fenton reaction. The Fenton reaction (Eq. 4-1) produces hydroxyl radical (•OH) [157], a reactive oxygen species, via the reduction of hydrogen peroxide (H_2O_2) by ferrous iron (Fe(II)).

$$Fe(II) + H_2O_2 \rightarrow Fe(III) + \bullet OH + OH^- \qquad (4\text{-}1)$$

Hydroxyl radical is believed to be the most powerful oxidant naturally generated in water, and it will tend to react non-specifically and at near diffusion limited rates with dissolved constituents in surface waters, including organic micropollutants and microbial pathogens.

In iron-containing surface waters, there are several processes involved in the formation of •OH via the Fenton reaction, many of which are photochemically driven. Generally, because the dominant form of iron in most surface waters is particulate or colloidal ferric iron, photoreductive formation of Fe(II) is critical. Rates of direct photoreduction of lattice Fe(III) is often too slow in oxic conditions at pH 6 or above [158], such that it is not likely to be a major route to Fe(II) formation in the environment. Instead, photochemical reduction of iron oxides mediated by surface associated organic ligands represents the most plausible pathway to labile Fe(II) production in surface waters, and as such, this process has been extensively studied [55, 141, 159].

The sequential steps leading to the generation of labile Fe(II) have been summarized by Sulzberger and Laubsher [56], initiating when a chromophoric organic

ligand (*L*, for example dissolved forms of organic matter) adsorbs to the mineral surface (Eq. 4-2).

$$\equiv\text{Fe(III)OH} + L \leftrightarrow \equiv\text{Fe(III)-}L + \text{H}_2\text{O} \qquad (4\text{-}2)$$

In sunlight, the Fe(III)-ligand surface complex represents an effective chromophore, capable of absorbing a photon and then transferring this energy to surface Fe(III) (i.e., so-called ligand-to-metal charge transfer). The net effect of this process is the generation of a surface-bound ferrous iron (Fe(II)), coupled to the oxidation of the organic ligand (Eq. 4-3).

$$\equiv\text{Fe(III)-}L \xrightarrow{\lambda} \equiv\text{Fe(II)-}L^{+} \qquad (4\text{-}3)$$

Subsequent dissolution of the ligand complex occurs, and the final, presumed rate-determining step, detachment of Fe(II) from the surface to yield dissolved Fe(II). Notably, release of Fe(II) from the oxide surface is preferred relative to Fe(III) because of its bulkier atomic size [24]. Additionally, protons in solution can help to destabilize the Fe(II)-O bond through attachment, finally leading to solubilzed Fe(II) and accordingly, greater rates of Fe(II) dissolution at lower pH. This dissolved, labile Fe(II) is then available react in the Fenton reaction or other iron-dependent surface water processes. We note that in addition to these heterogeneous reactions to Fe(II) production, soluble complexes of Fe(III) are photoactive. Thus, ligand-promoted dissolution of Fe(III) followed by soluble complex photoreduction also represents another viable source of Fe(II) to participate in the Fenton reaction (Eq. 4-4).

$$\text{Fe(III)-}L(aq) \xrightarrow{\lambda} \text{Fe(II)-}L^{+}(\text{aq}) \qquad (4\text{-}4)$$

In parallel to these surface specific steps to yield Fe(II), the Fenton reaction requires H_2O_2 must be generated simultaneously. In sunlit surface waters, this occurs via the photolysis of dissolved organic matter (DOM) (Eq. 4-5) [48], which can absorb light energy to form a excited state DOM species (DOM*). The DOM* in turn reduces molecular oxygen to superoxide ($O_2^{\cdot-}$), which subsequently undergoes disproportionation to produce H_2O_2 [91, 160].

$$DOM^* + O_2 \rightarrow 2O_2^{\cdot-} + 2H^+ \rightarrow H_2O_2 + O_2 \qquad (4\text{-}5)$$

Thus, the ensuing reduction of photogenerated H_2O_2 by surface or soluble forms of Fe(II) would allow for •OH formation via the Fenton reaction.

While complicated, this sequence of reactions, often referred to as the heterogeneous photochemical Fenton reaction, is believed to be an important source of •OH in surface waters. An as yet unexplored variable in this entire process is iron oxide particle size. In fact, most work to date has focused on amorphous phases (ferrihydrite and amorphous ferric hydroxide) while assuming that more crystalline phases such as goethite and hematite are too unreactive to contribute to this process in surface waters. However, nanoscale phases of these more crystalline phases may exhibit unique, size-dependent activity that makes them contributors to hydroxyl radical formation in sunlit waters. For example, recent evidence [59-61, 63, 99, 136] has suggested that iron oxides including goethite and hematite exhibit size dependent interfacial reactivity for process such as adsorption and dissolution, both of which are necessary steps in the reaction sequence for •OH formation. Generally, because nanoparticles can be more reactive per unit mass than their larger analogs, they may contribute disproportionately to the heterogeneous photochemical Fenton process in surface waters.

For example, Barton et al. [58] found that at circumneutral pH suspensions of nanohematite (< 10 nm) in the presence of siderophores exhibited a greater capacity to adsorb Pb(II) compared to a larger 40 nm hematite when normalized for surface area differences under otherwise identical conditions. Madden et al. [107] found that hematite particles with the average diameter of about 7 nm oxidized manganese about 1.5 times more than their larger analogue, which they argue was due to inherent irregular surface characteristics that lend to lower energy barriers related to surface-Mn association. In the context of the photochemical Fenton reaction, these previous results suggest it may be possible for nanoscale iron phases to generate a higher number of chromophoric surface

complexes via ligand uptake, ultimately enhancing the rate and extent of oxide photoreduction and •OH formation.

Enhanced reactivity of iron oxide nanoparticles has also been reported for dissolution processes. Cwiertny et al. [59] explored the size dependent dissolution of microrod goethite compared to nanorod goethtite and found that the nanoparticles exhibited up to 4 times greater surface-area-normalized dissolution over time. They attributed the observed dissolution enhancement to greater surface area and increased concentrations of functional groups on the surface of nanorods. Similarly, Echigo et al. [61] demonstrated that 7 nm hematite exhibited increased rates of reductive dissolution via ascorbic acid relative to large 30 nm hematite particles, which they attributed to a greater availability of highly reactive, monodisperse particles in 7 nm hematite suspensions. Earlier in this work we demonstrated the inherent size-dependent reactivity of hematite across most dissolution processes (i.e., proton promoted, ligand promoted, thermal reductive, and photoreductive dissolution), and that this influence of particle size is not affected by aggregation for select (i.e., reductive) dissolution processes. In particular, greater rates of Fe(II) formation via reductive dissolution implies that iron oxide nanoparticles may be a larger source of labile Fe(II) in surface waters, making them likely contributors to H_2O_2 reduction and •OH radical formation.

Collectively, we believe these observations of size-dependent reactivity imply that nanoscale phases of iron oxides may provide a larger than anticipated contribution to •OH formation in surface waters. It is now widely accepted that such nanoscale iron phases are ubiquitous in the environment [19, 20]. In particular for surface waters, nanoparticulate iron oxides are likely to be the phases most stable in the water column and photic zone as a result of their small size, thus they likely play a significant role in iron photochemistry in surface water. Finally, from reports of their greater activity in sorption and reductive dissolution reaction, it is reasonable to assume that the magnitude of reactivity enhancement will may be greater for multi-step reactions due to additive

size-dependent reactivity. For instance, 3-fold greater DOM uptake and 3-fold greater dissolution activity may produce a net rate enhancement far greater than either individual step in isolation, depending on the nature of the rate-limiting process. With respect to Fenton reaction, which requires sequential sorption, photoreduction and dissolution, such a scenario of additive reactivity could make nanoscale iron oxides the primary iron phase in surface water responsible for •OH formation.

In this study, we seek to quantify the impact of particle size on the production of hydroxyl radical in model surface water systems containing nanoparticulate iron oxides. Two sizes of nanophase hematite, 8 and 40 nm, were utilized in illuminated ($\lambda \geq 305$ nm) batch suspensions containing Suwannee River Humic Acid as a model for dissolved organic matter under both acidic pH (pH 3), and slightly acidic pH (pH 5 and 6) conditions. DOM-mediated rates of ferrous iron photoreductive dissolution were quantified for both sizes of hematite as a function of pH, while steady-state hydroxyl radical concentrations were also measured to determine if the heterogeneous photo-Fenton reaction exhibited size-dependent reactivity for nanoscale oxides.

4.3 Experimental methods

4.3.1 Reagents. Reagents were ACS grade or better, and all experiments, material syntheses, and solutions utilized Millipore Q-Grad2 deionized water. Hematite syntheses used ferric nitrate nonahydrate (Fisher; 100%) and nitric acid (Fisher; 70%). Phenol (Sigma Aldrich; ≥99%) was used as a probe compound for hydroxyl radical formation in photolysis experiments. Fe(II) sorption experiments utilized ferrous chloride (Sigma Aldrich; 98%). Colorimetric analysis of dissolved Fe(II) concentrations employed 1,10-phenanthroline (Sigma Aldrich; ≥99%), an buffer made from ammonium acetate (Fisher; ≥98%) and acetic acid (Sigma Aldrich; ≥99.7 %), as well as hydroxylamine hydrochloride as a reductant when measuring total dissolved iron concentrations. Measurements of Fe(II) also used ammonium fluoride (Fisher; 99.5%) to complex any Fe(III) in the system prior to ferrous iron measurement. Desferrioxamine mesylate salt

(DFOM) (Sigma Aldrich; ≥92.5%), an iron chelator, was used in control experiments. Two different batches of Suwannee river humic acid standard II were obtained from the International Humic Substance Society (IHSS) in July 2009 and January 2013, henceforth referred to as SRHA09 and SRHA13, respectively. Generally, batches of SRHA II contain approximately 52 % C(w/w), charge density 9.13 meq/gram carbon for carboxylic groups, and 3.72 meq/gram carbon charge density for phenolic groups [161, 162]. Unless otherwise noted, the majority of experiments were conducted with SRHA13. Two reagents, N,N-diethyl-1,4-phenylenediammonium sulfate (Sigma Aldrich; ≥98%) and peroxidase (Sigma Aldrich) were used for colorimetric detection of hydrogen peroxide.

4.3.2 Hematite synthesis and characterization. Methods of hematite preparation and characterization have been presented in previous chapters. Briefly, Sorum's method [117] was used to prepare smaller hematite particles, while the method of Schwertmann and Cornell [118] yielded larger hematite particles. Sorum's method calls for the drop-wise addition (0.5 ml/min) of ferric nitrate into boiling water, after which the cooled suspension was placed into dialysis bags and purified over several days, and ultimately placed in weigh boats to dry. The method of Schwertmann and Cornell involves baking 16.16 g ferric nitrate in 2 L of 0.002 M nitric acid for approximately 7 days at 98° C. The cooled sediment was then washed and centrifuged three times before freeze drying. Both iron oxide materials were stored as powders.

Characterization of each hematite powder was performed using standard techiques. Firstly, X-ray diffraction (XRD) (Rigaku MiniFlex II) with a Co source was used to confirm each iron oxide phase. Transmission electron microscopy (TEM) (JEOL 2100F) was used at 200 kV bright field mode to determine morphology and size of both nanohematites. Particle sizing was performed using the software Image J to measure approximate characteristic lengths of both nanohematite particles. Average sizes of 200 particles were used for particle sizing produced from the Sorum [117] method, and

averaged characteristic lengths of 100 particles were used to determine particle size from the Schwertmann and Cornell [118] synthesis method. Surface area characterization was performed on each powder using N_2 gas adsorption Brunauer-Emmett-Teller (BET) isotherm (Quantachrome BET Nova 4200e).

4.3.3 SRHA sorption onto hematite. Sorption isotherms were performed in batch suspensions (0.5 g/L) with both sizes of hematite exposed to a range of initial concentrations in SRHA (0-80 mg/L) at pH 3 and 5 (for SRHA13) or 6 (for SRHA09). Stock solutions of SRHA were prepared by dissolving 15 mg of dry SRHA material in 100 mL of DI water at pH ≥ 10 overnight. Stock pH was then lowered to ~7 for storage. These experiments were conducted in glass beakers that were mixed using a magnetic stir-plate and stir-bar. Preliminary experiments established relatively fast sorption kinetics. Thus, to ensure equilibrium was achieved in all systems, suspensions of hematite and SRHA were mixed for at least 3 hours prior to sampling. After equilibrium was established, 1 mL of suspension was removed and centrifuged at 14,000 RPM for 5 minutes. We note that controls were performed by measuring SRHA concentration (without iron oxide in suspensions) with and without centrifugation. It was determined that no measurable amount of SRHA was removed due to centrifugation. The supernatant was then transferred to a quartz cuvette and the remaining concentration of SRHA present in the supernatant was determined via absorbance at λ 254 nm. Measured absorbances were then converted to dissolved concentrations of SRHA based upon calibration curves developed with standards of known SRHA concentration.

4.3.4 Fe(II) dissolution in irradiated suspensions of hematite and SRHA. Rates of SRHA-mediated photoreductive dissolution of hematite were measured in reactors containing 5 mg/L SRHA and 0.5 g/L hematite in 25 mM NaCl. The reactor was illuminated with a 1000 W xenon arc lamp (Newport Coporation, Irvine ,CA) equipped with a 305 nm long-pass filter to allow for UV and visible light. Reactions were

conducted in a jacketed 50 mL beaker (Chemglass Life Sciences, Vineland, NJ), allowing temperature control at 25 °C via a circulating water bath.

Dissolution rates were measured at pH 3 and pH 5 (SRHA13) or 6 (SRHA09). Under acidic (pH 3) conditions, aerobic environments were sufficient for Fe(II) detection. A suspension sample was removed prior to irradiation to measure an initial value of total dissolved iron (FeTOT) and dissolved ferrous iron (Fe(II)) concentrations. During irradiation, samples were removed every hour to monitor how these concentrations changed over time. All samples were filtered through 0.22 µm Nylon filter (Tisch Scientific, North Bend, OH) prior to colorimetric analysis, such that dissolved iron is operationally defined as being able to pass through a 0.22 µm filter.

For dissolution experiments conducted at higher pH values (pH 5 or 6), a different approach was utilized to minimize oxidation of Fe(II) during sample collection and processing. These experiments utilized a specially designed photochemical reactor equipped with a quartz window screw-top, three sampling ports, and a submerged port for a pH probe. The quartz window allowed for near full transmission of incident irradiation into the cell while also allowing the system to be maintained under anaerobic conditions. Suspensions were prepared as previously described; however they were then purged with N_2 gas (1 h/L) before the experiment was started. After the solution was sparged, N_2 was delivered to the reactor headspace above to maintain a positive overpressure within the reactor at all times during irradiation, thus minimizing entry of O_2. Samples were removed with Teflon tubing attached to a 3 mL leur-lock syringe and filtered. Samples were immediately quenched in 40 µL of 5 M HCl to prevent Fe(II) oxidation. We note that buffers were not used to maintain system pH during reaction. Rather, pH was maintained via the addition of dilute acid and base (0.05 M HCl or NaOH, respectively) as needed, based upon real-time pH measurements with the reactor-integrated pH probe.

4.3.5 Measurement of hydroxyl radical in irradiated suspensions of hematite and SRHA. Batch reactors were also utilized for quantifying hydroxyl radical production in a hematite and SRHA suspension during irradiation from light source previously described. A background electrolyte of 25 mM NaCl, 5 mg/L SRHA and 0.5 g/L hematite (8 and 40 nm) were utilized for all experiments. Reactors were continuously mixed kept at 25 °C during experiments under aerobic conditions. The hydroxyl radical probe phenol (100 μM initial concentration) was used to measure steady-state hydroxyl radical concentrations ($[\bullet OH]_{ss}$) [163]. Initially, 1 ml aliquots were taken and filtered through a 0.22 μm Nylon syringe-tip filter into a 1.5 ml amber crimp-seal vial to measure the initial phenol in the reactor. Sampling was performed at least hourly over the duration of irradiation. Adjustments in pH were made with 0.05 M HCl or NaOH, though pH varied minimally (±0.1) during experiments, which were conducted in triplicate.

To assess the role of Fe(II) in phenol decomposition, control experiments utilizing DFOM were conducted to ensure phenol decay was the result of an iron dependent process. Reactors containing 0.5 g/L hematite, 5 mg/L SRHA, and 0.2 mg/mL DFOM were allowed to magnetically mix for 1 h. Phenol with an initial concentration of 100 μM was added 15 m before the suspension was irradiated ($\lambda \geq 305$ nm). Samples (1 mL) were removed at least hourly and filtered (0.22 μm Nylon) into an amber 1.5 ml crimp seal vial. All samples were analyzed for phenol.

4.3.6 Fe(II) sorption isotherms. Sorption and desorption experiments with Fe^{2+} in hematite suspensions were performed with 8 and 40 nm hematite particles. Suspensions contained 0.5 g/L hematite and vary concentrations (40 μM-700 μM) of $FeCl_2$ under anoxic conditions (i.e., conducted within an anaerobic chamber). Suspensions were prepared in 25mM NaCl and were buffered with 25mM HEPEs at pH 7. Specifics of reactor construction, as well as adsorption and desorption protocols, were adapted from Larese-Casanova and Scherer [86]. Briefly, each reactor consisted of a foil covered 40 mL screw cap vial. Initial solutions of buffer and $FeCl_2$ (30 mL) were allowed

to rotate for at least 10 hours to reach equilibrium and to allow formation of any precipitates from trace oxidation. All solutions were then filtered (0.2 μm) into new vials, to which hematite was subsequently added to initiate the sorption experiment. Ferrous iron and hematite were once again mixed for 10 hours before 1 mL aliquots were taken for iron analysis as described below.

4.3.7 Analytical methods. As previously described in earlier chapters, colorimetric analysis with 1,10-phenanthroline was used to determine FeTOT and Fe(II) [121, 122]. Measurement of photochemically generated hydrogen peroxide (H_2O_2) was performed in aerobic, illuminated batch reactors containing 5 mg/L SRHA. Colorimetric determination of H_2O_2 was performed according to Bader et al. [164] and compared to results from dark controls containing 5 mg/L SRHA in reactors covered in aluminum foil to omit light.

For experiment utilizing phenol as an •OH probe, samples were analyzed via HPLC equipped with photodiode array detector (DAD) (Agilent Technologies, Palo Alto, CA). An Eclipse XDB-C18 column (Agilent Technologies) was used to separate phenol from solution for measurement at λ 254 nm. A mobile phase of 65 % 1mM sodium acetate and 35 % acetonitrile was used and was adjusted with concentrated HCl to pH 3. A flowrate of 1 mL/min was used for the mobile phase.

4.3.8 Quantifying dissolution rates and steady-state •OH concentrations. Plots of FeTOT and Fe(II) versus time were prepared from all iron data collected. For hematite suspensions at all pH values, ferrous iron production rates were quantified via linear regression analyses of plots of Fe(II) versus time. Rates are presented with standard deviations from at least triplicate dissolution experiments. Hydroxyl radical production was quantified via the measured decay of the organic probe phenol. In irradiated suspensions with SRHA and hematite, phenol exhibited exponential decay. As such, semi-log plots of normalized phenol concentration ([P]) against time were linear (Figure 4-1), from which linear regression analyses furnished a pseudo-first order reaction rate

coefficient (or k_{obs} value) shown in Eq. 4-7. Integration of Eq. 4-7 yields Eq. 4-8, which may be plotted to determine the value of k_{obs} (i.e., slope). Assuming [•OH] remains constant throughout the experiment (i.e., at steady-state), the steady-state •OH concentration ($[•OH]_{ss}$) was calculated from Eq. 4-9 in which k_{phenol} is the known, second-order rate coefficient for the reaction between •OH and phenol ($1.4 \times 10^{10}\ M^{-1}s^{-1}$) [163].

$$d[P]/dt = -k_{obs}[P] \quad (4\text{-}7)$$

$$\ln([P]_t/[P]_0) = -k_{obs} \cdot t \quad (4\text{-}8)$$

$$k_{obs} / k_{phenol} = [•OH]_{ss} \quad (4\text{-}9)$$

4.4 Results and discussion

4.4.1 Characterization of hematite powders. Results of hematite characterization have been presented previously in Chapter 2. Briefly, XRD analysis confirmed that both material synthesis methods were indeed hematite (α-Fe_2O_3). Imagining analysis from TEM determined that each synthesis method produced particles of different sizes and morphologies. The smaller pseudo-hexagonal plate-like particles of hematite was approximately 8.1 (±1.6) nm the larger nanoparticle with a rhombohedra morphology as determined by TEM images was approximately 39.5 (±7.9) nm and 29.2 (±5.4) nm (diagonal lengths), hereafter referred to as the 8 and 40 nm particles, respectively. Surface area analysis of dry powders on both 8 and 40 nm hematite revealed a specific surface area of 80 m^2/g and 40 m^2/g with a standard deviation ± 6% from replicate measurements.

4.4.2 Sorption of SRHA isolates onto hematite. Sorption isotherms were conducted with SRHA on both 8 and 40 nm hematite suspensions at pH 3 and pH 5 (Figure 4-2 a and b). Equilibrium was rapid, being achieved on the order of 3 h at both pH values. At equilibrium in pH 3 suspensions, the majority of SRHA was adsorbed to the hematite surface. As such, the amount of SRHA adsorbed per unit hematite mass was near identical for 8 and 40 nm hematite below initial SRHA concentrations of 20 mg/L.

Evidence suggests, however, that the 8 nm suspensions exhibit a greater overall capacity for SRHA. At the highest initial solution phase SRHA concentration explored (40 mg/L) the 8 nm suspension adsorbed roughly 60% more SRHA per gram of hematite than 40 nm hematite.

As expected, uptake of SRHA on hematite decreased with increasing pH. In Chapter 2 we found that zero charge to be similar for both 8 and 40 nm hematite (~pH 5.5 in 25 mM NaCl), with the surface becoming more negatively charged at higher pH values. Thus, at pH 3, the more positively charged hematite surface is expected to adsorb more SRHA due to favorable coulumbic attraction between the negatively charged functional groups within the organic matter and the protonated, positively charged hydroxyl groups on the hematite [48, 165].

Despite a less extent of SRHA uptake, similar trends in size-dependent SRHA uptake were generally observed at the higher pH value. At pH 5 (Figure 4-2 b), the initial SRHA concentration (5 mg/L) resulted in essentially all mass being adsorbed to the surface in both 8 and 40 nm hematite suspensions at equilibrium. However, at all greater initial concentrations of SRHA ($\geq$ 10 mg/L) approximately 1.4 to 1.8 times more SRHA was adsorbed in 8 nm suspension.

This behavior is reminiscent of that observed in our earlier work with oxalate as a model compound for dissolved organic matter. In Chapter 2, the greater uptake of oxalate per unit mass of hematite in 8 nm suspensions was attributed to a presumed greater concentration of surface active sites on the smaller nanomaterial, as suggested by alkalimetric titrations. Accordingly, one would expect a comparable trend in SRHA uptake, as is observed in Figure 4-2a and 4-2b. However, we do note that magnitude of SRHA increase observed in 8 nm suspensions (~1.5-fold) is less than what we previously reported for oxalate (~3-fold). In fact, subsequent investigations conducted with another batch of SRHA (i.e, SRHA09) revealed essentially no difference in mass normalized uptake between 8 and 40 nm suspensions at pH 3 and pH 6 (Figure 4-2c and 4-2d). These

differences between oxalate and SRHA are not entirely understood, but can likely be explained by the differences in molecular size of the two sorbates, as well as potential differences in the mechanisms responsible for uptake.

We note that all subsequent reactivity studies including SRHA were conducted at an initial concentration of 5 mg/L, at which both 8 and 40 nm suspensions absorb essentially all organic matter from solution (see Figure 4-2). This value was chosen for several reasons. First, this SRHA concentration is relative to those often encountered in surface waters [48]. Second, with essentially all SRHA adsorbed to the hematite surface, it minimizes any contribution of solution phase organic photolysis on probe phenol degradation, thereby increasing the likelihood that decay is attributable to surface-mediated photochemical processes. We also note that in preliminary experiments conducted at higher SRHA concentrations, photoreactivity actually decreased, presumably as a result of light screening from the higher concentration of dissolved SRHA. Finally, by working under conditions where both 8 and 40 nm suspensions absorb the same amount of SRHA per unit mass, we are able to consider the photoactivity of both suspensions assuming a roughly equivalent number of chromophoric surface complexes. This may allow for the source of any reactivity differences between 8 and 40 nm suspensions to be more easily discerned.

4.4.3 SRHA-mediated photoreductive dissolution. Photoreductive dissolution experiments were conducted in 0.5 g/L hematite suspensions (8 and 40 nm) containing 5 mg/L SRHA at pH 3 and 5. During irradiation, nearly all iron that was solubilized was released from the surface as Fe(II), as expected (i.e., measured concentrations of FeTOT and Fe(II) were essentially equivalent within analytical uncertainty). Rates of photoreductive dissolution (Figure 4-3) were greater at pH 3 relative to pH 5, as is typically observed for (photo) reductive dissolution processes on iron oxides (see Chapter 2 and references therein). In both 8 and 40 nm hematite suspensions, rates of SRHA-mediated photoreductive dissolution decreased by roughly a factor of 2 and 1.5,

respectively, in response to increasing pH from 3 to 5. This rate of change in dissolution rate with increasing pH is on par with that previously noted in Chapter 2 for reductive dissolution with ascorbic acid mediated thermal (dark) reductive dissolution (~2 fold decrease from pH 3 to 6). However, SRHA-mediated photoreduction appears far less sensitive to pH than observed previously for oxalate-mediated photodissolution (~15-fold decrease from pH 5 to pH 7), although an explanation for such a difference is not yet understood.

At both pH values, suspensions of 8 nm hematite resulted in greater rates of iron dissolution than 40 nm suspensions. The magnitude of this difference was essentially consistent at both pH values, with Fe(II) production rates in 8 nm hematite suspension being roughly 2-to-3 fold greater than 40 nm suspensions at both pH 3 and 5, as shown in Figure 4-3. Generally, this result agrees with the trends in size-dependent reactivity previously reported by us (Chapter 2) and others [58, 61, 107, 136] for iron oxide nanoparticles. Specifically, consensus seems to be growing that under a given set of system conditions and for a specific reaction (i.e. sorption, reduction, dissolution,) nanoscale iron oxides, including hematite, consistently outperform their larger analogs on a per mass basis.

However, a closer evaluation of the trends observed in Figure 4-2 suggest a more complex picture for hematite size-dependent reactivity with SRHA relative to results more typically obtained with model compounds (e.g., oxalate, ascorbic acid). As previously noted, SRHA sorption capacity was equivalent for both 8 and 40 nm hematite at 5 mg/L for all pH values investigated. Thus, per unit SRHA adsorbed, 8 nm suspensions remain more reactive than 40 nm hematite. This is in contrast to our previous findings with oxalate (Chapter 2), in which differences in the amount of adsorbed oxalate concentrations between 8 and 40 nm hematite suspensions could reasonably account for observed differences in their rates of photoreductive dissolution.

One possible explanation could relate to the fate of Fe(II) on the surface of hematite after generation via photoreductive hematite dissolution. Figure 4-4 shows Fe(II) sorption isotherms conducted in suspensions of 8 and 40 nm hematite at pH 7, notably the lowest pH value at which appreciable Fe(II) uptake could be measured over the entire range of initial concentrations explored (0-1,500 μM). Consistent with results with SRHA and previously reported for other adsorbates on hematite, we see that 8 nm suspensions have a modestly greater capacity for Fe(II) uptake relative to 40 nm suspensions, which is most prominent at high concentrations of Fe(II). However, this greater degree of Fe(II) sorption would likely not be able to explain the difference in size-dependent reactivity observed for photoreductive dissolution rates between oxalate and SRHA in 8 and 40 nm suspensions.

Instead, we propose our results with SRHA are indicative that surface complexes between SRHA and hematite become more photoactive with decreasing particle size. For example, it has been previously suggested that nanoscale goethite possesses an increased density of hydroxyl groups [59], while our prior work with hematite and hematite aggregates suggest more surface sites per unit mass of 8 nm suspensions. The greater density of such sites may therefore allow unique complexes to be generated via binding to multiple functionalities simultaneously in the SRHA macromolecule, and such multi-dentate sites could exhibit unique reactivity that enhances the overall reactivity of 8 nm suspensions.

4.4.3 Size-dependent steady-state hydroxyl radical production. Figure 4-5 shows plots of normalized phenol concentration as a function of time in irradiated suspensions of 8 and 40 nm hematite suspensions containing 5 mg/L SRHA at pH 3 and 5. Unlike the aforementioned reductive dissolution experiments, phenol decay was measured in oxic systems to better simulate surface water processes, albeit at more acidic pH values than may be typically encountered.

Prior to evaluating size- and pH-dependent reactivity trends, initial control experiments were conducted to ensure phenol loss was truly attributable to the heterogeneous photochemical Fenton reaction. First, phenol decay was not observed to any extent in control experiments without hematite and SRHA (i.e., there was no direct photolysis of phenol) or in systems with only SRHA and phenol (i.e., there was no indirect, SRHA-mediated photolysis) over the timescales shown in Figure 4-6. Another common approach involves the use of an iron chelator, DFOM, which tightly binds surface and dissolved iron species [44], thus preventing Fe(II) from participating in the Fenton reaction. Results attempting to measure steady-state •OH concentrations with phenol in the presence of DFOM are shown in Figure 4-6. Clearly, the presence of DFOM iron shut down phenol decay at pH 3 in 8 nm suspensions, and similar behavior was observed for 40 nm hematite and in systems at higher pH.

Evidence in support of Fenton chemistry is also provided by studies exploring the production and fate of H_2O_2 in SRHA and hematite containing systems. Figure 4-7 shows results of experiments measuring H_2O_2 production in irradiated suspensions of 5 mg/L SRHA in the absence of hematite. From linear regression analysis (shown in Figure 4-7), the initial ($t < 3$ h) production rate of H_2O_2 was found to be roughly 2 μM/hr or 0.5 nM/s. Notably, this value agrees very well with recent work by Zhang et al. [166], who reported H_2O_2 production rates of 0.7 nM/s using 10 mg/L SRHA at similar illumination wavelengths (λ 302 nm) and power (1000 W Xe-Hg lamp) using a more sophisticated analytical method for H_2O_2 quantification [167, 168]. Moreover, consistent with the heterogeneous photo-Fenton reaction, addition of 0.5 g/L of hematite to irradiated SRHA suspensions limited H_2O_2 production (Figure 4-8). This decrease suggests that photoreduction of hematite leads to a net loss of H_2O_2, as would be expected for the reaction of H_2O_2 with photogenerated Fe(II). We note that control experiments conducted in the absence of light (dark) showed that H_2O_2 was stable upon exposure to hematite over the timescales shown in Figure 4-8. Thus, converging lines of

experimental evidence support that the phenol loss measured in our experimental systems and reported in Figure 4-5 is the direct result of a chemical process that is Fenton-like in nature.

With respect to reactivity trends, phenol decay was greatest at pH 3, which may be partially attributable to the greater stability of Fe(II) in the presence of molecular oxygen at lower pH values. The obvious phenol loss, which followed exponential decay and yielded half-lives of roughly 5 and 16 h for 8 and 40 nm suspensions, respectively, facilitated quantification of steady-state •OH concentrations. Based on the reported second-order rate constant for •OH reaction with phenol, as well as measured k_{obs} values at pH 3, we estimate steady-state •OH concentration of $3x10^{-15}$ M and $8x10^{-16}$ M in 8 and 40 nm hematite suspensions, respectively. Notably, this roughly 4-fold increase on •OH production for 8 nm hematite agrees reasonably well with the magnitude of Fe(II) production rate enhancement observed for these suspensions (see Figure 4-3).

At pH 5, phenol decay was only measurable in 8 nm hematite suspensions, corresponding to a steady-state hydroxyl radical concentration of ~$6 x10^{-16}$ M, nearly an order of magnitude decrease compared to pH 3. Indeed, as pH approaches circumneutral, hematite solubility decreases, rates of Fe(II) detachment from the surface slow, and rates of Fe(II) oxidation by dissolved O_2 increase [24]. The net result is a more limited release of Fe(II) into solution, which minimizes the probability of its reaction with H_2O_2 to generate •OH. Because phenol decay was not significant in 40 nm suspensions, it can be concluded that 8 nm suspensions remain more reactive per unit mass, although the exact magnitude cannot be quantified. Nevertheless, it appears that trends in $[•OH]_{ss}$ production reasonably follow and can be predicted from Fe(II) production.

It is worth noting that the slower rate of Fe(II) detachment from the mineral surface at higher pH values may actually increase the probability of heterogeneous Fenton-like reaction on or near the mineral surface rather than in bulk solution [169]. This is particularly true for systems such as ours where the majority if not all of the

SRHA is surface-bound. Thus, even in our 40 nm hematite suspensions, we cannot rule out the possibility that Fenton-like processes are occurring that may be more effective at reacting with probes other than phenol that better associate with the SRHA-coated hematite surface.

4.5 Conclusion

Consistent with our previous findings, this work demonstrates that hematite nanoparticles, per unit mass, display size-dependent reactivity that allow them to play a larger role in production of labile ferrous iron in model surface waters. The unique contribution of this study is that to date, all work demonstrating such size-dependent reactivity has been conducted in so-called model systems that may over-simplify the complexities anticipated in natural surface waters. Here, we demonstrate the existence of size-dependent reactivity under conditions that more closely mimic the complexity of natural waters containing humic substances and iron oxides including sunlit surface waters [170] and atmospheric waters [171]. Working with a representative natural organic matter, SRHA, we show that suspensions of 8 nm hematite exhibit enhanced photoreductive dissolution rates, which in turn leads to greater amounts of hydroxyl radical production in sunlit surface waters relative to production from larger (40 nm) hematite particles. This finding has implications for pollutant and pathogen fate in natural systems, where such contributions from nanoscale iron oxides must be accounted for when modeling natural system processes.

Generally, trends in steady-state hydroxyl radical production can be rationalized by trends in Fe(II) production, for which our previous studies (Chapter 2) and the current work with SRHA consistently find greater activity for 8 nm hematite suspensions. Furthermore, the body of work we have established for hematite convincingly shows that such trends in reactivity as a function of primary particle size are maintained regardless of pH, the mechanisms of dissolution, and even the aggregation state of the oxide. Thus, we can say with a high degree of confidence, that the observation of enhanced •OH

production with decreasing particle size presented herein can be reasonably extended to most natural waters, regardless of their pH.

From a more fundamental perspective, despite the generality of this result, there remain aspects of size-dependent hematite interfacial reactivity that merit further exploration. For example, including the current work and our previous studies, we have now established a fairly extensive database of uptake for a range of sorbates on hematite (e.g., oxalate, H^+ from alkalimetric titrations, SRHA, and Fe(II)). Consistently, in solutions of each adsorbate, 8 nm hematite suspensions demonstrate greater sorption capacity, yet the margin of enhancement relative to 40 nm suspensions is not constant. Thus, even though broad trends in size-dependent reactivity appear to be generalizable, there are specific surface chemical processes at play that also contribute to the degree of size-dependent interfacial reactivity. Such specific chemical interactions require closer examination to paint a more complete picture of nanoscale iron oxide reactivity.

Finally, this work adds to the existing body of literature on photochemical Fenton reactions by demonstrating the potential role for hematite, the most thermodynamically favorable iron oxide, in this process. For example, Vermilyea et al. [96] demonstrated photo-Fenton reactions occurring at circumneutral pH values, using natural organic matter and a more labile form of Fe(III). Specifically, they worked with ferrihydrite and amorphous iron oxyhydroxides, phases that are generally much more reactive than thermodynamically stable phases (e.g., hematite and goethite). In our study, we specifically chose hematite nanoparticles as the focus because it is generally believed that interfacial activity decreases with increasing crystallinity and thermodynamic stability. As such, the contribution of hematite to many interfacial processes of relevance to natural systems, including hydroxyl radical formation via photo-Fenton chemical process, is often discounted. However, the potential for unique, size-dependent reactivity provides an avenue where even hematite can be an important player in processes related to the

production of bioavailable iron, and iron redox processes with implications for pollutant fate in surface waters.

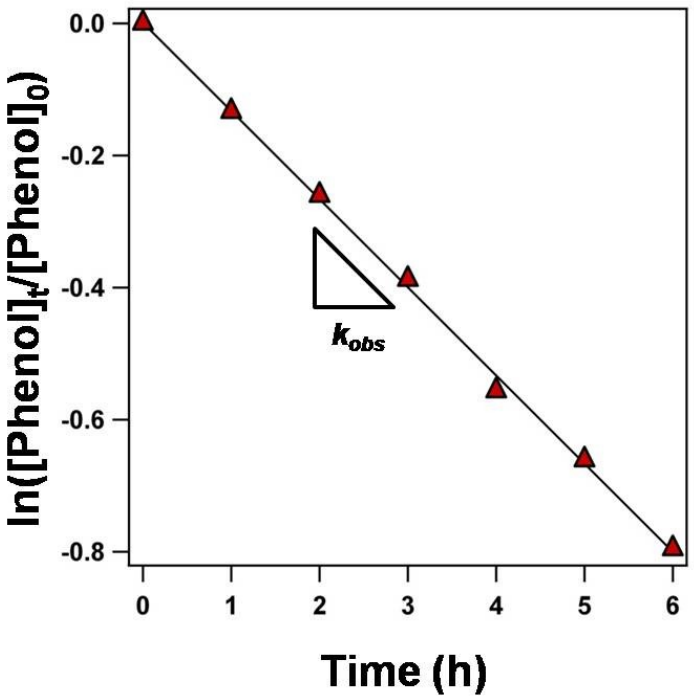

Figure 4-1. Semi-log plot of phenol decay over time in irradiated ($\lambda \geq 305$ nm) suspensions (0.5 g/L) of 8 nm hematite and 5 mg/L of SRHA at pH 3. The pseudo-first order rate constant, k_{obs}, from which steady-state •OH concentrations could be measured was determined from the slope of the best fit linear regression (shown).

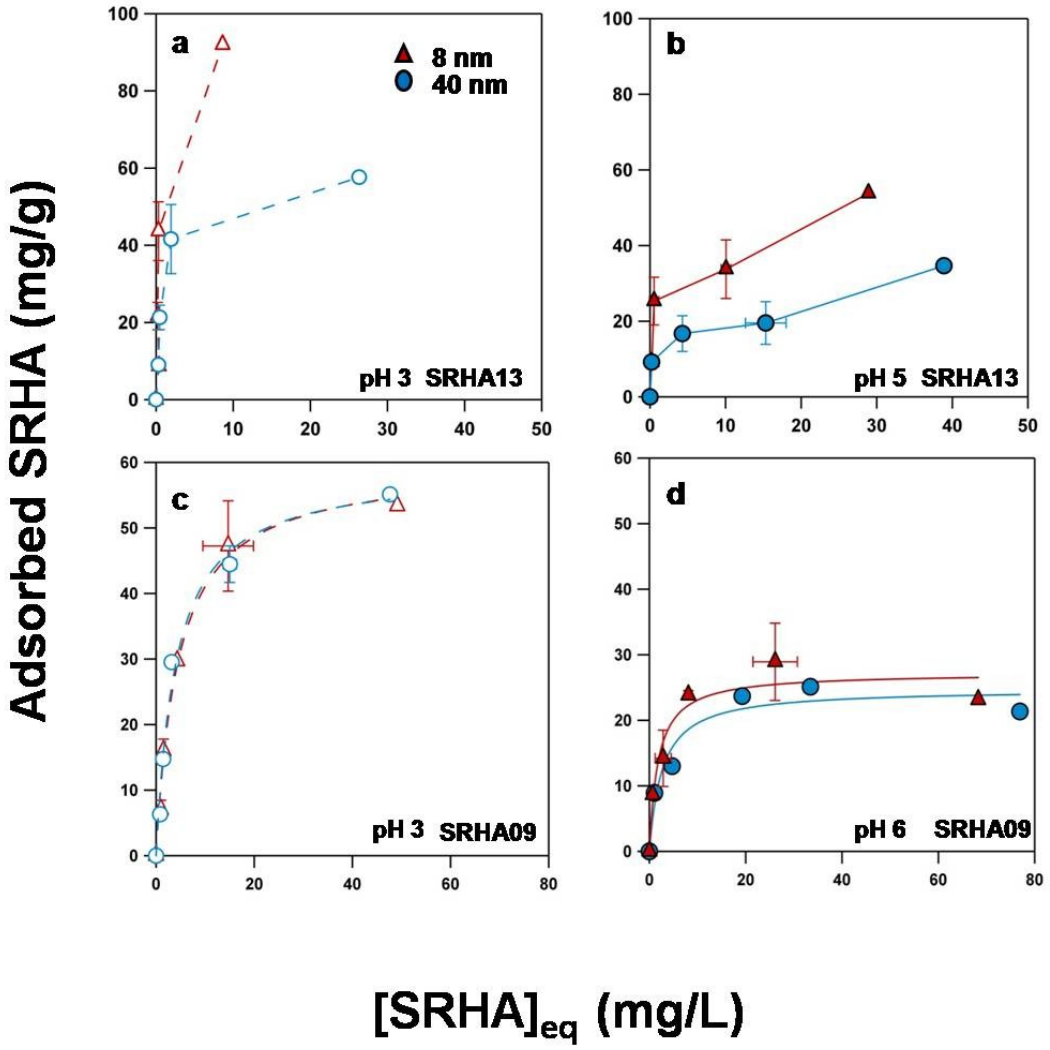

Figure 4-2. Sorption of SRHA onto 0.5 g/L suspensions of 8 and 40 nm in 25 mM NaCl. At pH 3 (a) sorption capacity of SRHA13 is about two fold greater than at pH 5 (b) for both sizes of hematite at SRHA concentrations greater than 5 mg/L. However all photo-experiments were run at 5 mg/L SRHA loading, for which both 8 and 40 absorb almost all SRHA. Additionally, a separate SRHA09 batch was tested, with sorption onto both sizes of hematite at pH 3 (c) and pH 6 (d). For this particular batch of SRHA sorption onto 8 and 40 nm was equivalent at both pH 3 and 6.

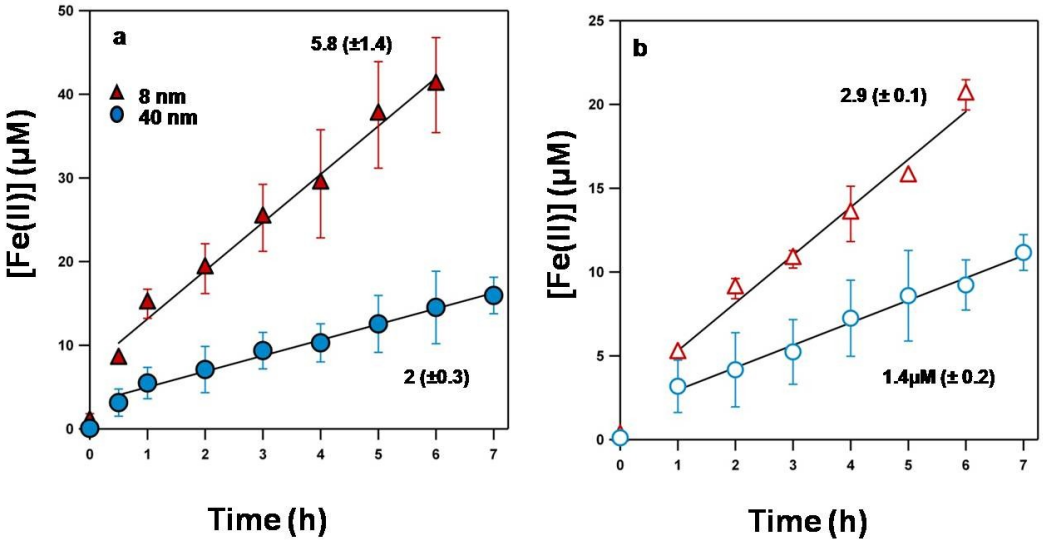

Figure 4- 3. Dissolution of Fe(II) in the presence of 5 mg/L SRHA ($\lambda \geq 305$nm) with 0.5g/L suspensions of 8 nm and 40 nm hematite at (a) pH 3 and (b) pH 5. At pH 3, 8 nm hematite produces approximately 3 fold more Fe(II) than its larger counterpart at 5.8 (±1.4) µM Fe(II) h^{-1} and 2 (±0.3) µM Fe(II) h^{-1}, respectively . At pH 5 the rates of production of iron are lower than at pH 3, 2.9 (±0.1) µM Fe(II) h^{-1} and 1.4 ±(0.2) µM Fe(II) h^{-1}, for 8 nm and 40 nm, respectively. Notably, a 2 fold increase in Fe(II) production is still observed for 8 nm hematite nanoparticle suspension compared to 40 nm.

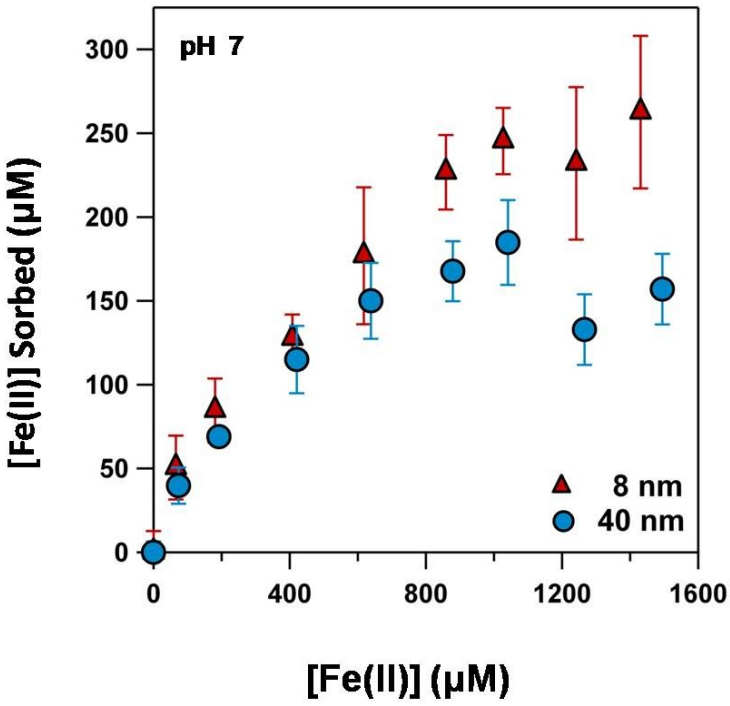

Figure 4-4. Sorption for Fe(II) onto the surface of 0.5 g/L 8 and 40 nm hematite buffered at pH 7 under anaerobic conditions. Initial concentrations of Fe(II) ranged from 0-1500 µM. Uptake of Fe(II) is slightly greater for 8 nm hematite and best observed at high concentrations of Fe(II) (> 800 µM). Error bars represent standard deviations based on replicate (at least 3 or more) experiments.

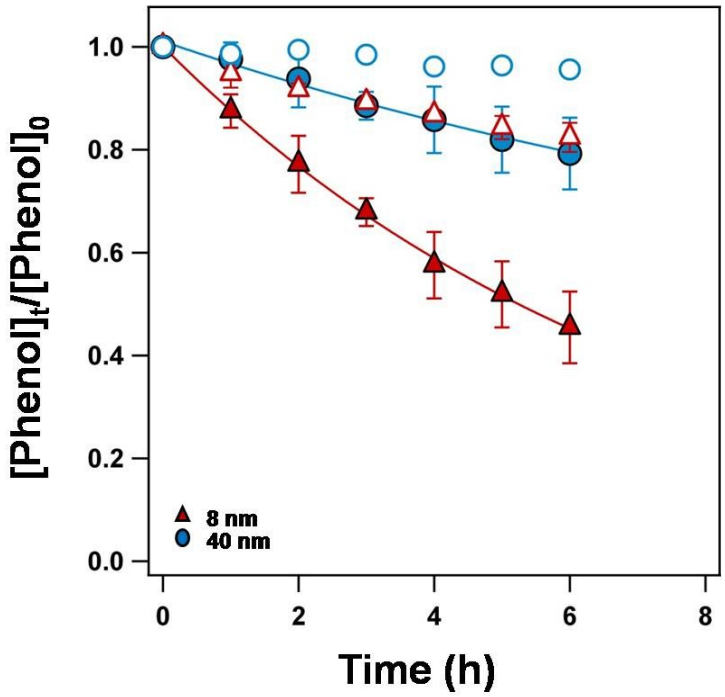

Figure 4- 5. Irradiated ($\lambda \geq 305$) suspensions of 0.5 g/L hematite suspensions with 5 mg/L SRHA. Initial concentrations of phenol were approximately 100 µM. Phenol decay was measured over time at both pH 3 (filled markers) and pH 5 (open markers). At pH 3 $[\bullet OH]_{ss}$ measurements were about 4 times greater for 8 nm suspension at 3 $x10^{-15}$ M compared to 8 $x10^{-16}$ for the 40 nm suspension. At pH 5 suspensions of 8 nm hematite produced about 6 $x10^{-16}$ M steady-state hydroxyl radical. At pH 5 suspensions of 40 nm showed insufficient phenol decay, thus accurate determination of $[\bullet OH]_{ss}$ was not possible.

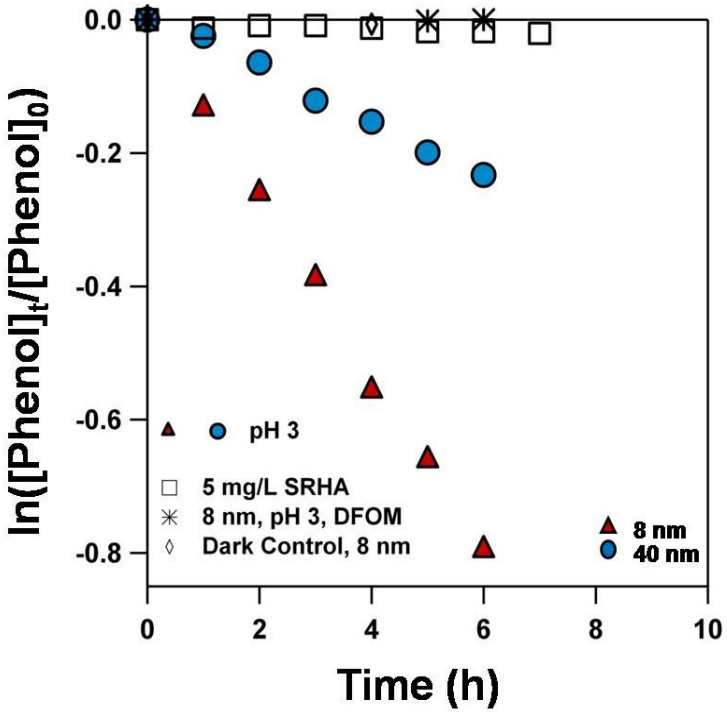

Figure 4-6. Control experiments to ensure phenol decay was an iron dependent process. Initial controls with only irradiated ($\lambda \geq 305$ nm) 5 mg/L SRHA showed no phenol decay. Irradiated reactors with 0.5 g/L 8 nm hemaitite, 5mg/L SRHA, and 0.2 mg/mL DFOM had no observable phenol decay. Finally, dark controls using 0.5 g/L 8 nm hematite and 5 mg/L SRHA showed no probe decay. Phenol decay at pH 3 is shown for reference.

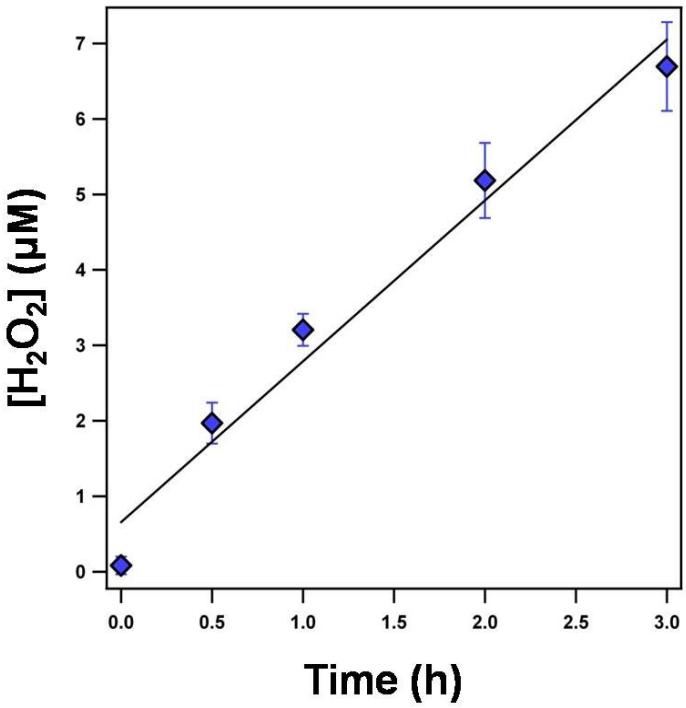

Figure 4-7. H_2O_2 production in 5 mg/L SRHA ($\lambda \geq 305$nm) at pH 3 with no iron oxide present. From a simple linear regression, H_2O_2 production rate was determined to be approximately 2 μM h^{-1}. Similar concentrations were observed at higher pH as well.

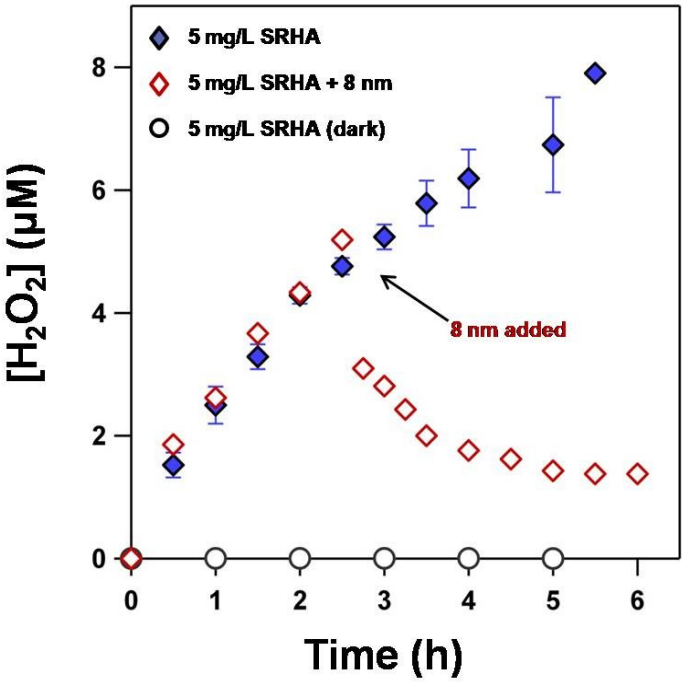

Figure 4-8. H_2O_2 production (solid diamonds) from 5 mg/ L SRHA ($\lambda \geq 305$ nm) with no iron oxide present at pH 3. At 2.5 hours 8 nm hematite (0.5g /L) was added to the irradiated reactor (open diamonds). After addition of the iron oxide decay of photo-generated H_2O_2 in solution was observed. Controls were performed using SRHA in the dark (open circles) in which no H_2O_2 was detected. Additional controls using reactors spiked with H_2O_2 (~ 10 μM) in 0.5 g/L suspensions of 8 nm and 40 nm hematite in the dark showed no measurable amount of H_2O_2 decay. This suggests that decay shown (open diamonds) in irradiated suspensions of 5 mg/L SRHA with the addition of 8 nm hematite was due to Fenton-like processes.

CHAPTER 5
CONCLUSIONS

Collectively, this work provides a more comprehensive understanding of nanomaterial reactivity, spanning from fundamental considerations of the origins of size-dependent reactivity to the practical consequences for pollutant fate in sunlit surface waters as a result of the photochemical reactivity of naturally occurring iron oxide nanoparticles. As discussed below, each Chapter fills gaps in our current knowledge regarding the environmental importance of size-dependent reactivity of natural nanomaterials, with specific focus on the abundant iron oxide, hematite (α-Fe_2O_3). Outcomes of this work should be applicable to the interfacial reactivity of iron oxide nanomaterials in a range of settings including sunlit surface waters, groundwater and a range of engineering applications in which iron oxides are currently utilized. As with most research, it also revealed questions that merit further consideration and eventual study.

5.1 Generality of size-dependent dissolution

The unique contribution of Chapter 2 is that it considers the generality of size-dependent nanoparticle reactivity. Work with hematite encompassed a broad range of dissolution processes across a wide pH range, making it among the first to consider whether size-dependent trends in hematite dissolution were a generally observable phenomenon or restricted to specific processes and conditions. Developing such understanding fills a critical void when attempting to predict the contribution of nanoparticle reactivity in different systems of environmental relevance.

The key outcome of Chapter 2 is that the dissolution activity for suspensions of 8 nm hematite were consistently greater than those of 40 nm hematite under all conditions considered. Moreover, the magnitude of the increase observed for 8 nm hematite was roughly constant (by a factor of 4-6) across all pH values and dissolution mechanisms, suggesting that size-dependent activity exhibited by hematite nanoparticles is not only

generally applicable across a broad range of solution conditions but also that the trends in reactivity with primary particle size are process independent.

Outcomes from Chapter 2 are both fundamental and practical in nature. Fundamentally, converging lines of evidence suggest that the difference in reactivity observed between 8 and 40 nm hematite relates not to inherent differences in particle reactivity but rather to the relative amount of reactive surface area available in aggregated suspensions of each primary particle. For example, while zeta potential measurements revealed similar point-of-zero-charge for both 8 and 40 nm hematite suspensions, alkalimetric titrations suggested that 8 nm suspensions exhibited a greater base-neutralizing capacity, consistent with a greater amount of ionizable surface groups (e.g., surface hydroxyl groups). Further, TEM imaging performed on non-reacted and reacted particles indicated selective dissolution was occurring on the larger rhombohedra particles (i.e., at edges, corners, and defects), while dissolution on the smaller plate-like particles showed no observable selectivity. Thus, it is evident that uniform dissolution across the entire particle is occurring, but only on the 8 nm particles. As is discussed below, further work into surface facets that may play a direct role in size-dependent reactivity is merited.

Practically, empirical relationships are presented in Chapter 2 that relate dissolution rates to pH for proton-promoted, ligand-promoted, and thermal reductive dissolution mechanisms. These empirical relationships will be useful in helping to better quantify the contribution of nanoparticles to iron dissolution process and iron cycling in a range of environments. For example, common components of dust aerosol include iron oxides, which will undergo redox cycling in anthropogenically derived acidic conditions (i.e., H_2SO_4) and via photochemical reactions [106, 126]. Notably, this work is also among the first to investigate and conclusively demonstrate hematite nanoparticle size-dependent reactivity into environmentally relevant neutral pH values. Thus, we provide evidence that such size-dependent reactivity, which most often is only examined in very

acidic conditions not representative of most aquatic environments, could be important in a larger number of aquatic systems (i.e., those near circumneutral pH) than is currently realized.

5.2 Influence of aggregation on reactivity

Chapter 2 revealed that suspensions of 8 and 40 nm hematite primary particles aggregate to similar extents and thus their reactivity could be compared reasonably accurately across dissolution mechanisms and the pH range considered. However, a more quantitative understanding of how aggregate size influences iron oxide interfacial reactivity remained elusive. Further, it was unclear whether size-dependent reactivity trends observed in Chapter 2 in aggregated suspensions were applicable over the entire distribution of particles sizes, including primary particles, encountered in suspensions.

To fill these voids, Chapter 3 established how aggregation plays a role, or lack thereof with simple reductive dissolution. This chapter demonstrated that, contrary to expectations, aggregate size does not play a factor in primary particle size-dependent reactivity for redox active processes. Specifically, small aggregates (e.g., 50-200 nm) compared to larger aggregates (e.g., ≥1000 nm) comprised of the same primary particle size (either 8 or 40 nm) of hematite showed essentially equivalent mass-normalized reactivity toward reductive dissolution with ascorbic acid. For reductive dissolution, this lack of an influence of aggregates size on per mass reactivity was also observed for other environmentally relevant iron oxides (i.e., ferrihydrite and goethite).

Evidence of aggregate-size independent reactivity for reductive dissolution processes runs counter to the widely held belief that aggregation limits interfacial reactivity by consuming reactive surface area as particles coalesce. Indeed, aggregation has been previously shown to limit nanomaterial reactivity, including iron oxides. However, most clear examples of iron oxide reactivity inhibition via induced aggregation involve non-redox processes such as proton-promoted dissolution [64] or adsorption [78].

In contrast, findings herein suggest that aggregation method and aggregate size have minimal to no detrimental bearing on hematite redox reactivity.

We propose that the semi-conductive nature of hematite may allow it to counter the inhibitory effect on reactivity most often noted for aggregation. Specifically, electron transfer through hematite has been shown to occur through bulk crystal conduction [85]. The ability of electrons to transfer across the hematite lattice may also facilitate particle-to-particles transfer, particularly when particles are tightly packed into a dense aggregate. Particle-to-particle electron transfer has been noted for similar semi-conductive materials such as photocatalytic TiO_2 [154] and thus may also be plausible in hematite. Such behavior would explain why per mass activity of hematite is independent of aggregate size for ascorbic acid dissolution, allowing a greater fraction of aggregate mass to participate in electron transfer relative to those hematite particles accessible at the solid-water interface. In contrast, rates of non-reductive dissolution processes (e.g., ligand or proton promoted dissolution) would be constrained by the reactive surface area available on aggregates, a variable that could change over several orders of magnitude give the range in aggregate sizes observed in our fractionated hematite suspensions.

The unique findings from Chapter 3 may establish a new precedent for understanding the reactivity of nanomaterials in both engineered and environmental systems. For example, under most environmentally relevant conditions natural nanomaterials, such as iron oxides, will also be extensively aggregated. It is in this aggregated state that they will participate in a wide range of abiotic and biologically mediated redox processes critical to pollutant fate and elemental cycling. Thus, findings in Chapter 3 may one day allow for more accurate modeling of such processes, providing guidance of how nanomaterial aggregation should be accounted for during model development.

5.3 Size-dependent reactivity and ROS production

Chapter 4 explored the implications of size-dependent reactivity on the photo-Fenton reaction, a chemical process in surface waters that is driven by available iron. This work is the first to demonstrate size-dependent reactivity for the DOM- mediated photoreductive dissolution of hematite and the corresponding generation of hydroxyl radical (•OH). Specifically, the 8 nm hematite suspension exhibited enhanced ferrous iron production rates compared to that of 40 nm hematite. These Fe(II) production rates in turn scaled with steady-state concentrations of hydroxyl radical ($[•OH]_{ss}$), where the 8 nm hematite showed enhanced $[•OH]_{ss}$ production at both acidic and more moderately acidic pH more representative of natural waters. Thus, work in Chapter 4 shows that size-dependent reactivity observed in relatively simple, single reaction-step systems can be preserved in more complex, multi-step reaction sequences where several size-dependent phenomena may be occurring in parallel. Notably, however, the magnitude of rate enhancement for the 8 nm hematite suspensions was on par with that measured in more simple, single-step reaction systems (roughly 3-5-fold more reactive).

To date, most work [59-61] with iron oxide nanomaterials has focused on relatively simple systems with reaction mechanisms governed by a single rate-determining step (e.g., sorption or dissolution). Thus, the primary motivation of Chapter 4 was to determine if size-dependent reactivity trends observed in these idealized model systems could be preserved in more complex, multi-step reaction sequences where several size-dependent phenomena may be occurring in parallel and at similar rates. Indeed, we find that fundamental insights regarding dissolution reactivity (Chapter 2) and aggregate size-dependent reactivity (Chapter 3) can be extended to these more complex, environmentally relevant processes. Based upon our earlier reports of aggregate size-dependent Fe(II) production, results in Chapter 4 coincide well with expectations derived from simplified model studies. Even the magnitude of $[•OH]_{ss}$ enhancement for the 8 nm

hematite suspensions was on par with that measured in more simple, single-step reaction systems (roughly 3-5-fold more reactive).

Our observation of greater $[\bullet OH]_{ss}$ production resulting from the greater propensity of iron oxide nanoparticles to undergo reductive dissolution Fe(II) improves our understanding of the phases present in sunlit waters that are most likely to participate in the photo-Fenton reaction. While the photo-Fenton reaction has been shown to occur in sunlit waters [170], where the resulting •OH subsequently impacts pollutant fate [93] and microbial kill [94], debate continues over the species most responsible for ROS generation. Based on the outcomes of Chapter 4, closer focus should be paid to nanoscale and colloidal iron oxides, which will exhibit greater photoreductive dissolution ability and a greater tendency to stay suspended in the water column relative to their larger analogs. These most reactive materials are likely to represent the phases capable of contributing to reactivity at circumneutral pH values, particularly for amorphous phases of nanoscale iron oxides such as ferric hydroxide.

5.4. Future research

This work has filled essential knowledge gaps in iron oxide size-dependent reactivity. For example, it demonstrated size-dependent hematite nanoparticle reactivity is observable across all dissolution mechanisms and extends into environmentally relevant pH values. Additionally, aggregation effects did not limit size-dependent reactivity. In fact, enhanced size-dependent reductive dissolution was consistent across all aggregate sizes, regardless of aggregation mechanisms. Size-dependent reactivity was further confirmed in model surface water systems, where labile iron production was a key factor to hydroxyl radical formation. Outcomes of this work have, therefore, significantly improved our understanding of size-dependent reactivity of naturally abundant iron oxide nanoparticles. However, there are also several, potentially fruitful avenues of future research on related topics stemming from knowledge gained in this work.

5.4.1 Facet-dependent reactivity of nanoscale iron oxides. The work in Chapter 2 revealed that 8 nm hematite nanoparticles had a consistently higher reactivity regardless of dissolution mechanism or solution pH. However, the exact cause of this enhancement is yet to be determined. Previous work [111, 112, 172-175] has extensively characterized reactive surfaces of hematite crystals. Structural facets such as kinks, edges, adatoms, and defects are often associated with reactivity. Maurice et al. [111] utilized simple acid dissolution to study changes along hematite planes, producing evidence that suggested the basal-plane was non-reactive to acid dissolution, while most reactivity occurred along step-edges and defects. Eggleston et al. [174] employed scanning tunneling microscopy to investigate non-periodic Fe atoms associated with 001 surface of hematite crystals. These surface Fe atoms can react markedly different from those Fe atoms within the periodic structure.

Within nanophase hematite there exists significant differences between particles less than 10 nm in size compared to those greater than 10 nm but less than 100 nm (i.e., technically defined as nanomaterial). At this point in time there has been little to no definitive studies investigating structural features of hematite nanoparticles that are less than 10 nm in size. In a noteworthy study, Echigo et al. [61, 62] presented reconstructed tomographical images of aggregates of 30 nm hematite before and after reaction with ascorbic acid and demonstrated that for particles larger than 10 nm selective dissolution occurred along grain boundaries and that defects within particles represented the initial points of dissolution. While informative for intermediate (30 nm) sized nanomaterials, such fundamental studies linking surface structure to reactivity of iron oxide particles less than 10 nm remains largely unexplored. Indeed, Chapter 2 demonstrated that BET determined surface area as well as geometric surface area analysis could not account for all the differences observed in size-dependent dissolution activity, suggesting that reactive faces of the smallest nanoparticles may be inherently more reactive and/or possess a greater density of surface sties than their larger analogues.

5.4.2 Aggregation effects on mechanisms and iron oxide phases. As mentioned in Chapter 3, the mechanism of dissolution may influence the impact that aggregation exerts on the size-dependent reactivity of nanoscale iron oxides. Specifically, aggregation was shown to have little to no effect on the rate of reductive dissolution of most iron oxides. However, complementary experiments exploring ligand-promoted dissolution with oxalate and acid-promoted dissolution at low pH showed that aggregation appears to significantly limit iron oxide reactivity. Further, previous studies have shown that aggregation inhibits non-reductive dissolution mechanisms (e.g., proton-promoted dissolution of nano and micron sized goethite) [64]. Additionally, uptake of non-redox active metals (e.g., Pb(II)) has also been shown to be limited by aggregation of iron oxides [78].

Evidence from previous work and work herein suggests that there is a broader, more complex story behind aggregation effects on iron oxides suspensions, particularly when interfacial redox activity is considered. Further research into whether aggregation effects are uniform across different reactivity mechanisms (i.e., sorption, reductive dissolution, and non-reductive dissolution) is worthwhile. Moreover, investigation into iron oxide phase and aggregation effects may be particularly. Larese-Casanova et al. [86] demonstrated that semi-conductive hematite can shuttle electrons through the bulk. This phenomenon may allow for redox active dissolution mechanisms to access a larger fraction of hematite mass available in aggregates (i.e.; particles on the inside of aggregates) via particle-to-particle electron transfer. As such, the inhibitory influence of aggregation would likely be minimized for redox processes, much as was observed in Chapter 3, relative to reactions that did not involve electron transfer.

On a related note, influence of aggregate size on iron oxide reactivity should be extended more rigorously to additional phases of iron oxides, as well as other metal oxides. For example, comparing the reactivity of size-fractionated suspensions of iron oxides to insulator materials, such as aluminum oxides, may reveal how much electron

shuttling into the bulk accounts for reactivity. As electron shuttling through the bulk is shut down, reactivity of aggregate sizes would be expected to scale with available reactive surface area. Similarly, it is recognized [154] that semi-conductive, photocatalytic TiO_2 can shuttle charge between particles, a process termed the "antenna effect". We believe this phenomenon is also occurring in aggregated suspensions of iron oxides, most notably hematite, during interfacial redox reactions (e.g., ascorbic acid reductive dissolution, sorption of Fe(II) and subsequent interfacial electron transfer). Future work should consider extending the phenomenon of the antenna effect from TiO_2 to hematite, It would have significant implications for engineered process currently investigating hematite as a photocatalyst for energy production [97].

5.4.3 Implications of size-dependent reactivity in engineered systems. Unique nanophase properties have implications for naturally occurring environmental processes as well as for the commercial application of iron oxide nanomaterials where they represent an inexpensive and versatile alternative in processes such as catalysis as a result of their natural abundance and simple preparatory methods. In semi-conductor photocatalysis, for example, hematite represents a promising alternative because it possesses favorable optical properties such as light absorption in the low energy visible spectrum, and can be tailored to enhance electronic properties via dopants such as, platinum or silver.

Recent ventures into maximizing energy efficiency have led to new ways of capitalizing on energy production from water splitting [97, 176, 177] using simulated solar energy. Reduction-oxidation potentials of nanophase iron oxides have been shown to be greater compared to their larger counterparts, which has been attributed to structural changes within the lattice that enhance proton binding [178]. Also, size-dependent band gaps of 0.3-0.6 eV arising from quantum confinement effects have been observed for bundled ultrafine nanorod hematite [179].

Nanohematite is an ideal material for use in photoelectrocatalysis because of its unique size dependent properties that can be easily tailored in syntheses. Further, hematite absorbs light over a much larger portion of the solar spectrum than other materials currently utilized as photoelectrocatalyst [180], and cation dopants can also be used to minimize electron/hole recombination [97, 181, 182] thereby promoting more efficient oxidation at the hematite surface. Thus, future work investigating the efficiency of size-dependent reactivity of nanoscale hematite, particularly with cation dopants (e.g., aluminum), for organic waste oxidation correlated with proton reduction to form H_2 gas is merited.

APPENDIX

INFLUENCE OF VARYING LEVELS OF EXTRACELLULAR POLYMERIC SUBSTANCES (EPS) ON HYDROXLY RADICAL MEDIATED DISINFECTION OF *Escherichia coli*

A.1 Abstract[1]

Photolysis of nitrate, a prevalent constituent in agriculturally impacted waters, may influence pathogen attenuation in such systems through production of hydroxyl radical (•OH). This study focuses on the efficacy of •OH generated during nitrate photolysis in promoting *E. coli* die-off as a function of extracellular polymeric substances (EPS) coverage. EPS levels of four *E. coli* isolates were systematically altered through a sonication extraction method and photochemical batch experiments with a solar simulator examined isolate viability loss as a function of time in nitrate solutions. *E. coli* viability loss over time exhibited two regimes; an initial induction time, t_s, with little decay was followed by rapid exponential decay characterized by a first-order disinfection rate constant, k. Increasing steady-state •OH concentrations enhanced *E. coli* viability loss, increasing values of k and decreasing t_s values, both of which were quantified with a multi-target bacterial disinfection model. Notably, at a given steady-state •OH concentration, values of t_s and k were independent of EPS levels, nor did they vary among the different *E. coli* strains considered. Results herein show that while •OH generated via nitrate photolysis enhances rates of disinfection in surface water, the mechanism by which •OH kills *E. coli* is relatively insensitive to common bacterial variables.

[1] An abbreviated version of this chapter has been published: Gong, A. S.; Lanzl, C. A.; Cwiertny, D. M.; Walker, S. L., Lack of Influence of Extracellular Polymeric Substances (EPS) Level on Hydroxyl Radical Mediated Disinfection of Escherichia coli. Environmental Science & Technology 2011, 46, (1), 241-249

A.2 Introduction

Photochemically generated reactive oxygen species (ROS) including hydroxyl radical (•OH) and singlet oxygen ($^1O_2$) occur naturally in sunlit waters, where they play important roles in pollutant degradation [183, 184] and pathogen attenuation [94, 185, 186]. Among ROS, •OH is often implicated as the primary entity responsible for bacterial disinfection in both natural [187, 188] and engineered [189-191] photochemical systems. While previous studies have often focused on the relative susceptibility of different pathogenic bacteria to ROS-mediated disinfection [188, 192], the influence of several biological variables in these systems remains poorly understood. Notably, a variable likely to influence •OH activity but not yet extensively explored is extracellular polymeric substances (EPS), a high molecular weight polymer exuded by bacteria that consists primarily of polysaccharides[193, 194] and proteins [195, 196], with some other components including nucleic acids [197]. To better predict the persistence of *Escherichia coli* (*E. coli*) in sunlit surface waters, a clearer understanding of the role of EPS in ROS-mediated disinfection is merited.

Bacterial disinfection in sunlit waters can occur by either direct or indirect photochemical processes. Direct photochemical disinfection is accomplished by UV light, especially in the UVB (280-320 nm) region of the solar spectrum, which is of sufficient energy to damage critical cellular components including DNA [198, 199]. In contrast, indirect photochemical disinfection involves the sensitized formation of extracellular ROS, whose bactericidal activity is typically attributed to reaction with cell outer membranes, causing decomposition of the membranes that leads to phospholipid peroxidation or even cell death [200]. Therefore, it is crucial in indirect photochemical disinfection processes that the transient ROS produced in bulk solution can be promptly transported to the cell surfaces [191, 192, 201-203].

While some EPS exuded by bacteria is dispersed as a soluble component in solution (i.e., soluble or free EPS), a portion stays in close proximity to the cells (i.e.,

bound EPS) [204] where it influences cell interactions with other particles and surfaces by bridging the cells to such substrates [205-207]. The physical presence of EPS around the cells also is known to protect cells from various environmental hazards [208]. Although not yet extensively investigated, it is anticipated that the bound EPS layer should provide some degree of protection from indirect photochemical disinfection by affecting the ability of ROS to react with and damage the cell outer membrane [209]. Specifically, highly reactive and non-specific •OH is likely to oxidize the lipids, proteins, and nucleic acids comprising EPS [210], in turn shielding more vital cell components from oxidative damage. Although soluble forms of EPS would likely function in a similar capacity, its influence on ROS activity is expected to be less than bound EPS that is more concentrated around the cell wall.

In a recent work with TiO_2 photocatalysts, Liu et al. [211] compared the bactericidal efficiency of •OH toward biofilm heterotrophic bacteria, the same biofilm heterotrophic bacteria after removing soluble EPS, and a native EPS-deficient *E. coli* strain. They observed faster disinfection rates when the soluble EPS was stripped off the biofilm heterotrophic bacteria via centrifugation than for biofilm heterotrophic bacteria with intact EPS. They proposed, therefore, that EPS may physically block or chemically quench the photocatalytically produced •OH. However, the influence of native EPS level in non-biofilm *E. coli* has yet to be explored, leaving questions over whether native EPS levels associated with cell surfaces are sufficient to inhibit ROS activity.

The main objective of this study was to quantitatively test and identify the role of EPS in photochemical disinfection of *E. coli* in the presence of •OH for four *E. coli* isolates with differing EPS levels, as well as systematically varied levels of bound EPS controlled by sonication. These model organisms were selected specifically to represent the type of species present in agricultural run-off waters in which photochemical disinfection processes may occur. Photochemical batch reactivity studies with each type of *E. coli* were conducted to determine the rate of viability loss over time using a

standard viability assay [212]. Rates of viability loss were then compared to trends in EPS levels, as well as the concentration of steady-state •OH present in each system. Trends in viability loss as a function of steady-state •OH and EPS levels were then used to test our initial hypothesis that bound EPS functions as a scavenger for •OH, thereby inhibiting its bactericidal activity.

As a model system for •OH generation, we employ nitrate photolysis, which is recognized as a route for •OH production in surface waters at levels with implications for pollutant fate [183], [213]. Average nitrate concentrations in surface waters are approximately 0-44 mg NO_3^-/L, and higher concentrations can occur in waters that are susceptible to agricultural runoff [214]. Thus, •OH production arising from nitrate photolysis is likely to be important in agriculturally impacted waters, although the implications of this process on bacterial pathogen fate are not yet established. A practical benefit of working with nitrate is that as a homogeneous system, it poses less complexity in bacterial studies relative to heterogeneity in ROS produced by other natural sensitizers such as dissolved organic matter (DOM) [215]. For example, recent studies with natural organic matter (NOM) have suggested formation of microenvironments in close proximity to NOM where multiple forms of ROS exist at concentrations that can be orders of magnitude above those existing in bulk solution [216, 217]. In these alternative sensitizer systems, therefore, it is difficult to accurately identify the nature and level of ROS to which the bacteria are exposed, which complicates efforts to clearly establish the role of EPS in ROS-mediated disinfection.

A.3 Experimental methods

A.3.1 Reagents. All solutions were made with reagent grade chemicals. Potassium phosphate monobasic (Fisher Scientific; 99.3%) was used to buffer pH. Potassium chloride (Fisher Scientific; 99.9%) was utilized to adjust ionic strength. Sodium nitrate (Fisher Scientific; 99.1%) was used to prepare nitrate solutions. Aqueous solutions of phenol (Sigma Aldrich; ≥ 99%) were used to measure steady-state •OH

concentrations. Sodium formate (Sigma Aldrich; ≥ 99%) was used as a radical quencher in selected experiments.

A.3.2 Measurement of steady-state •OH concentrations in photochemical batch systems. A 450 W O_3-free xenon arc lamp (Newport Corporation, Irvine, CA) was used to produce a collimated beam. Light was first passed through a water filter to remove infrared radiation and then a 305 nm long-pass filter to produce light in the UV and visible range. The incident photon flux of the lamp was measured using a ferrioxalate chemical actinometer [218]. Briefly, equal volumes of ammonium ferric sulfate (Sigma Aldrich; 99%) and potassium oxalate monohydrate (Riedel-De Haën; ACS reagent) were irradiated for several minutes, and the incident photon flux was found to be 2.2×10^{-5} einstein min^{-1}. The visible light range (≥400nm) was found to have a photon flux of 1.2×10^{-5} einstein min^{-1} All experiments were conducted in a 50 mL (37 mm ID) jacketed beaker at 25°C with 5 mM phosphate buffer at pH 7.0.

Steady-state concentrations of hydroxyl radical ($[\bullet OH]_{ss}$) were determined using phenol as a probe [163]. Batch reactors with varying concentrations of nitrate (50-500 mg/L as NO_3^-) and a known initial concentration of phenol (typically 100 μM) were exposed to light over several hours. Samples (1 mL) were taken hourly and transferred to a 2.5 mL crimp sealed amber vial for subsequent HPLC analysis. Samples were analyzed on an Agilent 1200 series HPLC (Agilent Technologies, Palo Alto, CA) equipped with a diode array detector. An Eclipse XDB-C18 column (Agilent Technologies) was used with a mobile phase of 35% acetonitrile with 65% 1 mM sodium acetate and acetonitrile at a flow rate of 0.75 mL/min and a detection wavelength of 254 nm.

Phenol decay was modeled as a pseudo-first-order reaction with respect to phenol. A semi-log plot of normalized phenol concentration versus time provided the pseudo-first-order rate constant, k_{obs}, from which values of $[\bullet OH]_{ss}$ were determined via normalization with the rate constant for phenol reaction with •OH ($k_{phenol} = 1.4 \times 10^{10}$ $M^{-1}s^{-1}$) [163].

A.3.4 Cell selection and preparation. Four wild type *E. coli* isolates from dairy cattle (DC1) [219], human (HU1) [219], swine (SP4) [220], and a pathogenic strain (O157:H7) [221] were investigated in photochemical batch studies. The strains were also chosen as they are documented as EPS-producing strains with different amount of EPS coverage.

The day before the experiment, a fresh pre-culture was prepared from the stock culture on a Luria-Bertani (LB) (Fisher Scientific, Fair Lawn, N. J.) agar petri-dish. *E. coli* cells were selected from the plate and inoculated into 5 mL of LB broth in 37°C overnight (14-16 h). The overnight pre-culture was then used to inoculate (1:100 v/v) a 200 mL LB broth. This culture was incubated in 37°C for four hours (DC1 and HU1) and three and half hours (SP4 and O157:H7) to reach mid-exponential phase. Cells were harvested by centrifugation (5804R; Eppendorf, Hamburg, Germany) with a fixed-angle rotor (F-34-6-38; Eppendorf) for 15 min at 4°C and 3700g to separate cells from growth media. To further rinse the cells, after the centrifugation the media was decanted and 10 mL of 10 mM KCl was added and the suspension was vortexed before a second centrifugation for 15 min at 4 °C and 3700 g. The rinsing steps, including decanting, adding electrolyte and vortexing were applied once more. After the third and final rinse cycle, 5 mL of 10 mM KCl was added to the pellet creating the stock solution to be used for further experimentation. The concentrations of each stock solution were quantified via a cell counting chamber (Buerker−Türk chamber, Marienfeld Laboratory Glassware, Lauda-Königshofen, Germany) and a light microscope (Fisher Scientific Micromaster). Typical cell stock solution concentrations in this study were between 2 to 10×10^{10} bacteria/mL. All cell media and electrolyte solutions were made by mixing deionized water (Millipore, Billerica, MA) and reagent grade salts (Fisher Scientific).

After the cell stock solution was prepared and the concentration was determined, the required volume of the cell stock solution was added either to 10 mL of 10 mM KCl for subsequent exposure to sonication, or directly added into 50 mL of nitrate solutions

(50-500 mg/L as NO^{3-}) or 50 mL of phosphate buffer (5 mM at pH 7) to achieve a final 50 mL suspension of 5×10^{8} cells/mL in the batch reactor.

A.3.5 Extraction and evaluation of EPS. In certain experiments the level of EPS was experimentally controlled via partial removal of EPS achieved using probe sonication (Omni-Ruptor 250, Omni International, Kennesaw, GA) and centrifugation (Eppendorf). This method was previously reported on in detail [222, 223]. Briefly, sonication was applied via a cell disruptor machine with a 5/32" Micro-Tip sonicating probe at 30% intensity (150 Watt maximum). The probe was placed directly in the solution and approximately 10 cm was immersed in the solution. The bacterial solution was kept in ice during the entire sonication process. Sonication was applied with fixed intensity (nominally 30%) and duration (20, 160, 300, 440, or 580 s total sonication time with a five second pause at every five second interval of sonication) to achieve the desired level of EPS removal. Afterwards, the sonicated solution was centrifuged at 4 °C and 4000 g for 20 min (Eppendorf) to separate the intact cells and the EPS that had been removed by sonication. After the centrifugation the supernatant was collected and passed through a 0.22 µm filter (Millipore, Fisher Scientific). The filtrate was collected as the EPS suspension for further compositional analysis. The pellet comprised of cells was re-suspended in 50 mL solutions composed of potassium nitrate and 5 mM phosphate buffer (pH 7) for later photochemical experiments.

The EPS composition, specifically the bulk sugar and protein amounts, were analyzed through established protocols. The sugar was quantified with Phenol-Sulfuric Acid (PSA) method [224], and the protein was evaluated by the Lowry method [225]. The PSA method was performed by adding 50 µL of 80% (w/w) phenol solution, and 5 mL of 95.5% sulfuric acid to 2 mL of the filtered supernatant containing the EPS. The reaction between sulfuric acid, phenol, and sugar molecules creates heat and a color change from clear to brownish. The solution is allowed to cool in room temperature for 10 min and this is followed by further incubation in a water bath (Lab-Line Instruments,

Inc., Melrose Park, IL) in 30°C for 20 min. Samples were put in a laminar flow hood for four hours at ambient temperature in order for the resulting color to stabilize. Subsequently, the absorbance was measured (Biospec-mini, Shimadzu Corp., Kyoto, Japan) at 480 nm with Xanthan gum (Sigma-Aldrich corporation, St. Louis, MO) as a standard. For analysis of the EPS protein level, 1.5 mL of alkaline copper reagent (made by adding 1 mL of 2% $Na_2C_4H_4O_6$, 1 mL of 1% $CuSO_4$, and 98 mL of 2% $NaCO_3$ in 0.1 M NaOH) was added into 0.3 mL of the EPS suspension. The mixture was next incubated at room temperature for 10 min before adding 75 µL of Folin reagent (Folin and Ciocalteu's Phenol Reagent, MP Biomedicals, LLC, Germany). The mixture required another 30 min of room temperature incubation. Subsequently, the solution absorbance was measured at 500 nm with bovine serum albumin (BSA, 1mg/mL) (Fisher BioReagents, Fisher Scientific) as the standard. The absorbance values obtained from the sugar and protein analyses were interpolated using Xanthum gum and BSA calibration curves to determine the sugar or protein concentration, respectively, in the EPS removed from cells via sonication. All salts and reagents (unless otherwise noted) were ACS or reagent grade (Fisher Scientific).

A.3.6 Exposure of model organisms to light. All photochemical experiments were conducted with the aforementioned 450 W O_3-free Xe arc lamp and a custom-made jacketed photo-reactor, whose contents were well-mixed via a stir bar and maintained at 25°C during all experiments via a circulating water bath (Thermo Scientific, Waltham, MA). Bacterial solutions containing a range of nitrate concentrations (0-500 mg/L as NO_3^-) were irradiated so as to vary the steady-state concentration of •OH generated in each system. Experiments were conducted with *E. coli* DC1 cells with various levels of EPS obtained by varying the duration of sonication (from 20-580 s), as described previously. Additional *E. coli* strains (HU1, SP4, and O157:H7) also were utilized to test the effect of cell strain at a fixed nitrate concentration (250 mg/L) and duration of sonication (300 s) for EPS removal.

During photochemical experiments, samples from the irradiated solution were withdrawn periodically over time and *E. coli* viability was measured. The percentage of viable *E. coli* was quantified using the Live/Dead BacLight kit (L-13152; Molecular Probes, Eugene, OR) and a fluorescent microscope (BX 51, Olympus, Japan) with a red/green fluorescence filter set (Chroma Technology Corp., Brattleboro, VT).

To identify the ROS type that is formed in irradiated nitrate solutions, a select number of photochemical experiments were conducted with bacteria in the presence of formate (50 mM) as a radical quencher. Control experiments were also conducted in which bacterial viability was measured in the presence of formate in both dark and irradiated batch systems without nitrate.

A.4 Results and discussion

A.4.1 Analysis of *E. coli* photochemical decay kinetics. During batch photochemical experiments (see Figure A-1), changes in *E. coli* viability over time showed two distinct regimes of reactivity. Region 1 was an initial period of little to no viability change, which we hereafter refer to as the "induction time" (t_s), and region 2 was characterized by more rapid viability loss over time that followed exponential decay.

A multi-target bacterial disinfection model (Eq. A-1) was applied to fit the experimental data taking account of the initial induction time (region 1) and the subsequent regime of exponential decay (region 2), which is typical of viability loss profiles observed in most pure culture bacterial disinfection processes [226]. The model takes the form of:

$$N = N_0[1-(1-\exp(-kt))^m] \qquad \text{(A-1)}$$

where N and N_0 are the number of viable bacteria in the reactor and initial population, respectively, t is the illumination time (min), and the two parameters, k and m are constants obtained through the process of fitting this equation to the experimental data. For these model-fit parameters, k (min^{-1}) is the inactivation rate constant indicating the rate at which disinfection occurred in region 2, whereas m is simply a fitting parameter

with no significant physical meaning [226]. Non-linear regression analyses were performed on $\ln(V/V_0)$ (V/V_0 means viability normalized by initial viability, both in percentage; when applying equation 1, $V/V_0=N/N_0$ in value) versus illumination time data using Origin 8.1 software (Origin Lab; Northampton, MA), providing best-fit parameters *k* and *m*. The initial induction time (region 1) at which population of cells begin to die-off is calculated using *k* and *m*, $t_s=\log(m)/[k*\log(e)]$ [226]. Values of *k* and t_s (region 1) were compared between different conditions. Fitted values for all experiments are reported in Table A1. To evaluate the significance of trends in model fit parameters for *E. coli* DC1 as a function of experimental variables (e.g., $[\bullet OH]_{ss}$, EPS level, presence or absence of radical scavengers), *k*, *m*, and t_s values were evaluated using analysis of variance (ANOVA).

A.4.2 Hydroxyl radical production in illuminated nitrate suspensions.

Values of $[\bullet OH]_{ss}$ (4.37×10^{-16}-1.70×10^{-15} M) determined from experiments with phenol are shown as a function of nitrate concentration (50-500 mg/L) in Figure A-2 Values of $[\bullet OH]_{ss}$ initially increased linearly with nitrate concentration, however, •OH concentrations began to plateau at higher concentrations (≥250 mg/L). This behavior is consistent with previous work, [183, 227] and attributable to the photolytic formation of nitrite, which can acts as a hydroxyl radical scavenger. For the majority of experiments, therefore, concentrations of nitrate were typically kept below 250 mg/L to avoid competition with nitrite for •OH. For experiments in which EPS levels were systematically varied via sonication, a nitrate concentration of 250 mg/L (corresponding to a value of $[\bullet OH]_{ss}=1.39\times10^{-15}$) was employed.

A.4.3 Effect of hydroxyl radical concentration on bacterial disinfection.

Results from photochemical batch experiments conducted with DC1 containing a natural level of EPS and exposed to different concentrations of $[\bullet OH]_{ss}$ and light at wavelengths (λ)≥305 nm are shown in Figure A-1. Direct photochemical disinfection occurred when $[\bullet OH]_{ss}=0$, resulting in the onset of complete viability loss after approximately 4 h

(Figure A-1a). Increasing values of $[\bullet OH]_{ss}$ shortens the time required to kill *E. coli* DC1 exposed to light at a wavelength≥305 nm. As the $[\bullet OH]_{ss}$ was increased incrementally, distinct patterns were observed. Faster rates of disinfection due to the presence of •OH were inferred by both the shortening of the induction time (t_s), and the increase in the rate constant for viability loss (k) relative to values obtained via direct photochemical disinfection. Over the range of $[\bullet OH]_{ss}$ concentrations investigated (Figure A-1b), the rate constant for viability loss (k) doubled compared to the value measured for direct photochemical disinfection. Meanwhile, the induction time t_s also decreased by a factor of two over the range of $[\bullet OH]_{ss}$ investigated.

In our batch photochemical systems, indirect disinfection accomplished by $[\bullet OH]_{ss}$ works in complement with direct photochemical disinfection, stimulating viability loss. Indeed, concurrent direct and indirect disinfection facilitates bacterial disinfection more effectively than direct disinfection accomplished by the available UV light alone. One-way ANOVA tests on k and t_s identified significant changes over different $[\bullet OH]_{ss}$ values.

To validate •OH as the primary entity responsible for the enhanced rates of die off in irradiated nitrate solutions, excess formate was added as a radical quencher (see Supporting Information Figure A-3). Resulting viability losses observed in the presence of formate were consistent with viability losses measured in systems free of nitrate (i.e., equivalent to viability losses from direct photochemical reaction), consistent with •OH as the active ROS responsible for enhanced *E. coli* viability loss in our systems. The result of reactions with formate are also consistent with trends reported in the literature [228].

A.4.5 Effect of EPS extraction on rates of photochemical disinfection. Figure A-4 (a) displays semi-log viability curves from photochemical batch experiments conducted with DC1 exposed to a fixed concentration of $[\bullet OH]_{ss}$ (1.39×10^{-15} M) and light of $\lambda \geq 305$ nm. Data are shown for DC1 with six different levels of EPS that were achieved by varying sonication time during extraction (data shown as dotted symbols in

(a)). For comparison, results are also presented from control experiments conducted in the absence of $[\bullet OH]_{ss}$ (i.e., 0 mg/L nitrate) for DC1 with three different EPS levels. In these controls, direct photochemical disinfection is the only mechanism involved in cell death (data shown as open symbols in (a)).

Figure A-4 (b) presents values of k (left y-axis) and t_s (right y-axis) obtained from non-linear regression analyses of data in Figure A-4 (a) from experiments with DC1 with six different EPS levels in the presence of 1.39×10^{-15} M $[\bullet OH]_{ss}$. Values of k and t_s are plotted as a function of sonication time (x-axis), where longer sonication times correspond to greater extents of EPS removal. For comparison, Figure A-4 (c) shows values of k (left y-axis) and t_s (right y-axis) as a function of sonication time (x-axis) from control experiments with DC1 conducted in the absence of $[\bullet OH]_{ss}$ (i.e., direct photochemical disinfection). Finally, for experiments conducted in the presence of 1.39×10^{-15} M $[\bullet OH]_{ss,}$ values of k (left y-axis) and t_s (right y-axis) are also presented with respect to total EPS (d), protein removed (e), and sugar removed (f) via the sonication process.

Similar patterns of disinfection were observed when EPS was removed from surfaces of bacteria, when applying sonication for varied times (20, 160, 300, 440, and 580 s). The greater sonication time removes an increasingly proteinaceous fraction of the EPS and retains lower total levels of EPS around the cells. However, all values of t_s observed were within the range of 110 to 150 min (see Figure A-4b) and no clear trend was exhibited with the application of longer sonication times (i.e., increasing amounts of EPS removal). Values of k also showed no clear trend with the extent of EPS removal (see Figure A-4b). This suggests no clear connection between the level of EPS on the *E. coli* surface and reactivity metrics for •OH-mediated disinfection (e.g., values of k or t_s) at the EPS level considered in this study.

Notably, our results also convincingly illustrate that extraction of EPS from *E. coli* DC1 does not affect the rate of direct photochemical disinfection when the cells are

exposed to light with $\lambda \geq 305$ nm (Figure A-4 (c)). Any differences in measured rates of direct photochemical disinfection over the range of variables considered are statistically insignificant.

The lack of an observable EPS effect for direct photochemical disinfection is justifiable; the organic functionalities present in EPS are not likely present in large enough quantities to effectively absorb higher energy UV-light so as to protect critical cellular components from sustaining direct photochemical damage. In contrast, the lack of an EPS effect on indirect disinfection is surprising and may seem counterintuitive. However, the trends may be attributed to the fact that not all EPS was removed by sonication. This is a limitation of the sonication method, as compared to others used for EPS extraction which can remove substantially more of the surface polymers [222]. However, this is the only method that leaves cells intact for subsequent disinfection studies. Hence, following sonication there is potentially a substantial EPS fraction remaining on the cell surface. Since previous work has suggested that it is the extracellular protein which reacts with •OH leading to disinfection [210], the subtle changes in the remaining proteinaceous EPS content may result in minor differences in indirect disinfection patterns.

A.4.6 Effect of EPS extraction on rates of photochemical disinfection in four wild type *E. coli* strains. To ensure that the observed lack of involvement of EPS in DC1 disinfection processes was not strain specific, EPS was extracted from four *E. coli* strain types (DC1, HU1, SP4, and O157:H7), results of extraction are shown in Table A-2. In these experiments a consistent length of sonication was applied (300 s), which resulted in different remaining levels of EPS bound to the cell surface. For DC1, the removed amount of sugar and protein was averaged to be 0.136 ± 0.001 and 1.545 ± 0.432 mg/10^{10} cells, respectively. For HU1, the removed amount of sugar and protein was 0.141 ± 0.002 and 1.167 ± 0.006 mg/10^{10} cells, respectively. The levels of sugar and protein removed for SP4 was 0.140 ± 0.007 and 1.289 ± 0.433 mg/10^{10} cells, respectively.

Finally, the EPS extraction for O157:H7 revealed sugar and protein levels removed of 0.156 ± 0.020 and 1.219 ± 0.324, mg/10^{10} cells, respectively.

After the EPS extraction step, the cells were exposed to light (wavelengths $\geq$ 305 nm) and an equal concentration of nitrate, producing an $[\bullet OH]_{ss}$ of 1.39×10^{-15} M and allowing for indirect disinfection processes to occur. All four strains were fully disinfected within an essentially identical 3-3.5 h time period (Figure A-5). A two-way ANOVA test on the rate of disinfection with factors 1) EPS level (full or partial remaining after the 300 s of sonication), and 2) *E. coli* strain also indicate a statistically insignificant relationship between the four *E. coli* isolates tested. These results clearly show that the insensitivity of •OH -mediated disinfection to bound EPS levels is a general phenomenon for *E. coli*, and not strain specific.

A.5 Conclusion

•OH generated during nitrate photolysis can enhance rates of viability loss in *E. coli* through indirect photochemical disinfection mechanisms. Counter to our original hypotheses, the extracellular polymer substances (EPS) bound to the cell surface has no observable impact on the rates of direct photochemical disinfection as well as •OH mediated indirect disinfection of *E. coli*. Notably, this study has also demonstrated that different agriculturally relevant isolates of *E. coli*, with full and partial EPS content on the cell surface, behave similarly in the presence of a fixed •OH concentration. Our initial intent was to demonstrate that EPS is an important biological variable that would impact photochemical disinfection rates; however, we found that not to be the case. Furthermore, there was remarkable consistency in rates of disinfection, regardless of native EPS levels or strain.

Although limit literature is available as to the influence of EPS on ROS mediated disinfection processes, the findings presented herein are contrary to previously reported trends. Liu et al. [211] previously reported that the presence of full EPS on cells in a biofilm decreased the disinfection efficiency than when soluble part of the biofilm EPS

had been removed. The rate of photocatalysis disinfection also was greater using intact *E. coli* cells than full EPS containing heterotrophic biofilm bacteria. They concluded EPS did have an impact of reducing rate of disinfection, and suggested a mechanism where EPS competes with bacterial cell wall for ROS [211]. The disparity between this study and ours is likely due to the levels of EPS encountered on the bacterium. The EPS levels are much less in planktonic *E. coli* as investigated here than EPS surrounding bacteria found in heterotrophic biofilms which accounts up to 90% of organic carbon [229].

These findings bode well for future efforts in modeling and prediction efforts for planktonic bacterial pathogen persistence in surface waters. Specifically, EPS levels appear to unimportant relative to other factors known to influence photochemical disinfection efficiency (e.g, presence of different endogenous sensitizers [230, 231], water chemistry [232, 233], etc.) and future model development must incorporate these known influencing parameters, but does not need to consider EPS level.

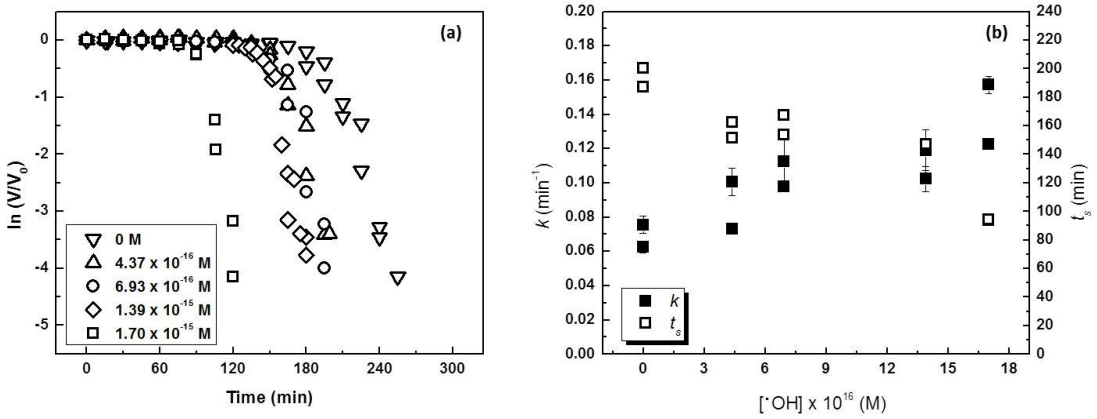

Figure A-1. Plots of *E. coli* DC1 exposed to light with wavelength ≥ 305 nm. a) Disinfection data presented as the natural log of cell viability normalized by initial viability versus the time of light exposure as a function of steady-state hydroxyl radical concentration ($[\bullet OH]_{ss}$). b) Results from non-linear regression analysis obtained from best-fit analyses of data presented in (a) with equation 1. The induction time (t_s) and viability loss rate constant (k) are shown as a function of steady-state hydroxyl radical concentration. Note that direct photochemical disinfection is the only process occurring when $[\bullet OH]_{ss}=0$.

Table A-1. Resulting data from photochemical disinfection: rate constant (k) and fitting parameter (m), reduced chi^2, adjusted R^2, and induction time (t_s)

Sample Name[1]	Strain[2]	Nitrate Conc. (mg/L).	Sonication[3] Time (s)	k[4] (min^{-1})	k error	m[5]	m error	Red. Chi^2	Adj. R^2	t_s[6] (min)
DC1 N0 0s-1	DC1	0	0	0.076	0.005	3.82E+06	4.43E+06	0.024	0.983	200
DC1 N0 0s-2	DC1	0	0	0.063	0.003	1.21E+05	8.58E+04	0.01	0.99	187
DC1 N0 20s-1	DC1	0	20	0.139	0.038	1.01E+13	8.98E+13	0.028	0.962	216
DC1 N0 20s-2	DC1	0	20	0.09	0.005	1.84E+07	2.04E+07	0.01	0.99	187
DC1 N0 160s-1	DC1	0	160	0.069	0.003	3.60E+05	2.02E+05	0.007	0.995	186
DC1 N0 160s-2	DC1	0	160	0.082	0.008	1.26E+07	2.19E+07	0.027	0.971	199
DC1 N0 0s-1	DC1	0	0	0.076	0.005	3.82E+06	4.43E+06	0.024	0.983	200
DC1 N0 0s-2	DC1	0	0	0.063	0.003	1.21E+05	8.58E+04	0.01	0.99	187
DC1 N50 0s-1	DC1	50	0	0.101	0.008	1.28E+07	1.90E+07	0.015	0.984	163
DC1 N50 0s-2	DC1	50	0	0.073	0.003	6.64E+04	4.00E+04	0.008	0.993	151
DC1 N100 0s-1	DC1	100	0	0.112	0.016	1.49E+08	4.38E+08	0.036	0.954	168
DC1 N100 0s-2	DC1	100	0	0.098	0.003	3.45E+06	1.59E+06	0.003	0.998	154
DC1 N250 0s-1	DC1	250	0	0.102	0.007	2.87E+06	3.52E+06	0.015	0.987	145
DC1 N250 0s-2	DC1	250	0	0.119	0.012	3.98E+07	7.81E+07	0.075	0.954	147
DC1 N500 0s-1	DC1	500	0	0.157	0.005	2.56E+06	1.46E+06	0.003	0.998	94
DC1 N500 0s-2	DC1	500	0	0.123	0.002	1.08E+05	2.61E+04	0.001	0.999	94
DC1 N250 0s-1	DC1	250	0	0.102	0.007	2.87E+06	3.52E+06	0.015	0.987	145
DC1 N250 0s-2	DC1	250	0	0.119	0.012	3.98E+07	7.81E+07	0.075	0.954	147
DC1 N250 20s-1	DC1	250	20	0.11	0.007	7.39E+06	9.02E+06	0.018	0.989	143
DC1 N250 20s-2	DC1	250	20	0.088	0.003	3.30E+05	1.78E+05	0.003	0.996	145
DC1 N250 160s-1	DC1	250	160	0.106	0.008	9.27E+05	1.09E+06	0.026	0.979	130
DC1 N250 160s-2	DC1	250	160	0.133	0.011	2.32E+07	3.61E+07	0.009	0.99	127
DC1 N250 300s-1	DC1	250	300	0.1	0.007	4.04E+06	4.91E+06	0.009	0.988	152
DC1 N250 300s-2	DC1	250	300	0.086	0.006	1.98E+05	1.96E+05	0.024	0.97	141
DC1 N250 440s-1	DC1	250	440	0.141	0.004	1.35E+08	8.73E+07	0.005	0.998	132
DC1 N250 440s-2	DC1	250	440	0.156	0.005	1.06E+08	6.87E+07	0.005	0.998	119
DC1 N250 580s-1	DC1	250	580	0.109	0.007	2.70E+05	2.73E+05	0.018	0.989	114
DC1 N250 580s-2	DC1	250	580	0.12	0.007	3.97E+07	4.75E+07	0.014	0.991	146
DC1 N250 0s-1	DC1	250	0	0.102	0.007	2.87E+06	3.52E+06	0.015	0.987	145

(*Table A-1 continued*)

DC1 N250 300s-1	DC1	250	300	0.1	0.007	4.04E+06	4.91E+06	0.009	0.988	152
DC1 N250 300s-2	DC1	250	300	0.086	0.006	1.98E+05	1.96E+05	0.024	0.97	141
HU1 N250 0s-1	HU1	250	0	0.096	0.005	1.59E+06	1.30E+06	0.023	0.984	150
HU1 N250 0s-2	HU1	250	0	0.117	0.006	1.38E+08	1.40E+08	0.012	0.989	160
HU1 N250 300s-1	HU1	250	300	0.136	0.007	1.10E+10	1.45E+10	0.018	0.988	170
HU1 N250 300s-2	HU1	250	300	0.096	0.006	3.24E+06	3.51E+06	0.044	0.976	156
SP4 N250 0s-1	SP4	250	0	0.079	0.004	9.59E+05	7.62E+05	0.011	0.984	175
SP4 N250 0s-2	SP4	250	0	0.095	0.007	7.97E+06	1.10E+07	0.027	0.968	168
SP4 N250 300s-1	SP4	250	300	0.095	0.008	1.44E+06	1.96E+06	0.031	0.964	149
SP4 N250 300s-2	SP4	250	300	0.102	0.016	2.48E+06	6.47E+06	0.171	0.878	145
O157:H7 N250 0s-1	O157:H7	250	0	0.1	0.007	9.85E+06	1.31E+07	0.02	0.973	161
O157:H7 N250 0s-2	O157:H7	250	0	0.066	0.004	3.75E+04	2.73E+04	0.017	0.975	160
O157:H7 N250 300s-1	O157:H7	250	300	0.097	0.005	4.73E+06	4.39E+06	0.013	0.984	159
O157:H7 N250 300s-2	O157:H7	250	300	0.074	0.005	3.42E+04	2.91E+04	0.028	0.967	141
Formate[7] DC1 N0 0s	DC1	0	0	0.069	0.006	1.22E+07	1.95E+07	0.025	0.972	236
Formate DC1 N50 0s	DC1	50	0	0.08	0.007	8.90E+07	1.58E+08	0.019	0.975	230
Formate DC1 N250 0s	DC1	250	0	0.08	0.003	1.95E+08	1.35E+08	0.004	0.996	239
Formate DC1 N500 0s	DC1	500	0	0.111	0.01	3.24E+11	8.04E+11	0.012	0.983	240

[1]Sample name contain four part including 1)"DC1" *E. coli* strain type, 2)"N250" as nitrate concentration (250 mg/L), 3)"300s" as total sonication time, and 4)"-1" or "-2" means duplicates.

[2] Different strain types of *E. coli,* DC1 stands for source dairy cattle, HU1 stands for source human, SP4 stands for source swine, and O157:H7 is a pathogenic strain also from swine.

[3]Probe sonication were applied by immerse 11 cm of probe into 10 ml of bacterial solution with 2.5×10^9 cells/ml using 30% (45 watt) intensity for varied lengths of total sonication break down in 5 second on and 5 second off cycles.

[4]k is photochemical disinfection rate constant calculated by fitting experimental curves with $N = N_0[1-(1-\exp(-kt))^m$, the larger the k indicate the faster the disinfection.

[5]m is also calculated through fitting the experimental curves with the equation mentioned above, however the value of m have no significant physical meaning.

[6]t_s=log(m)/[k*log(e)]) is the initial lag phase where no or very few viability loss have been observed due to bacterial self-repair during photochemical disinfection.

[7] Excess formate ($CHOO^-$, 50 mM) were added as hydroxyl radical quencher where the destruction ability of $^{\bullet}OH$ were quenched by reacting immediately with formate.

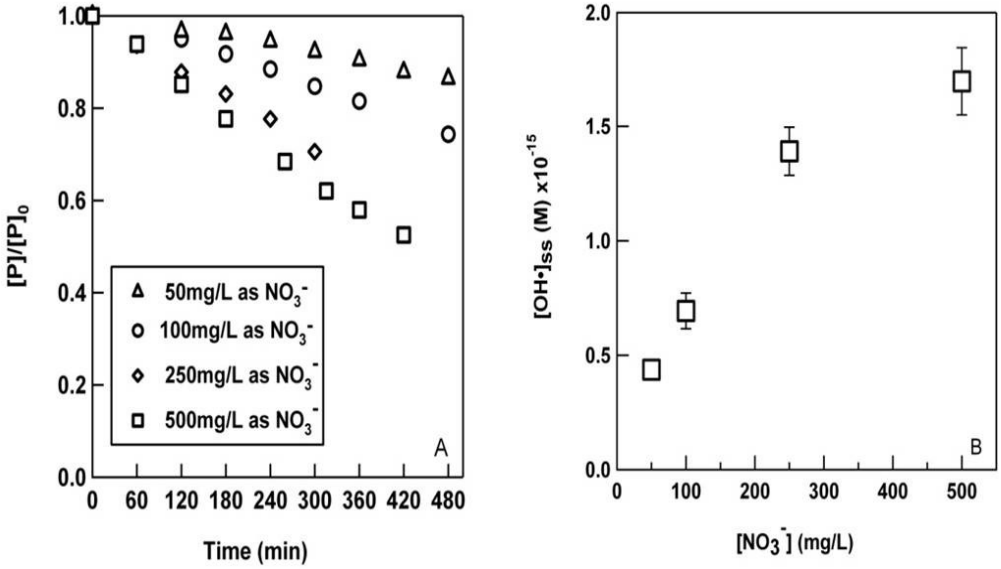

Figure A-2. (a) Normalized phenol decay ([P] = phenol concentration; $[P]_0$= initial phenol concentration) over time indicates the production of hydroxyl radical (•OH) by nitrate at wavelengths ≥ 305nm. (b) Calculated steady-state hydroxyl radical concentrations ($[•OH]_{ss}$) as a function of nitrate concentration (mg/L).These •OH concentrations (4.37×10^{-16} - 1.70×10^{-15} M) generated over the range of aqueous nitrate concentrations (50-500 mg/L) are slightly lower than other studies of •OH production from nitrate photolysis, most likely due to differences in our reactor setup and lamp power output.

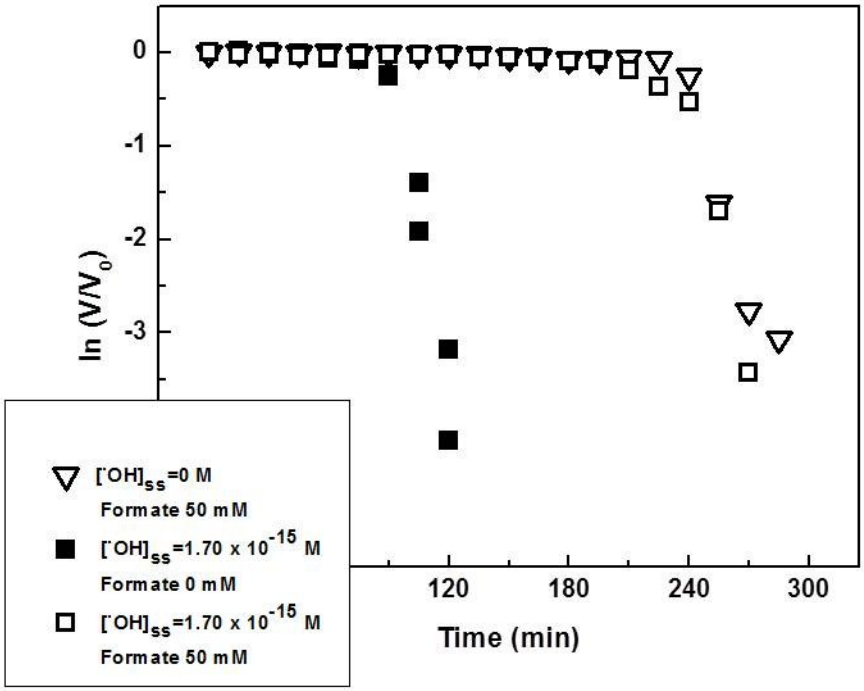

Figure A-3. Plots of *E. coli* DC1 exposed to light at wavelength ≥ 305 nm conducted at 0 and 1.7×10^{-15}M $[\bullet OH]_{ss}$ with or without the presence of excess formate ($CHOO^-$, 50 mM), a known •OH scavenger. Data presented as the natural log of cell viability normalized by initial viability versus the time of light exposure. Data is consistent •OH as the primary agent responsible for bacteria kill in all systems. Photochemical experiments with *E. coli* DC1 that were conducted with $[\bullet OH]_{ss}$ in the presence of excess formate revealed viability losses consistent with a direct photochemical reaction only.

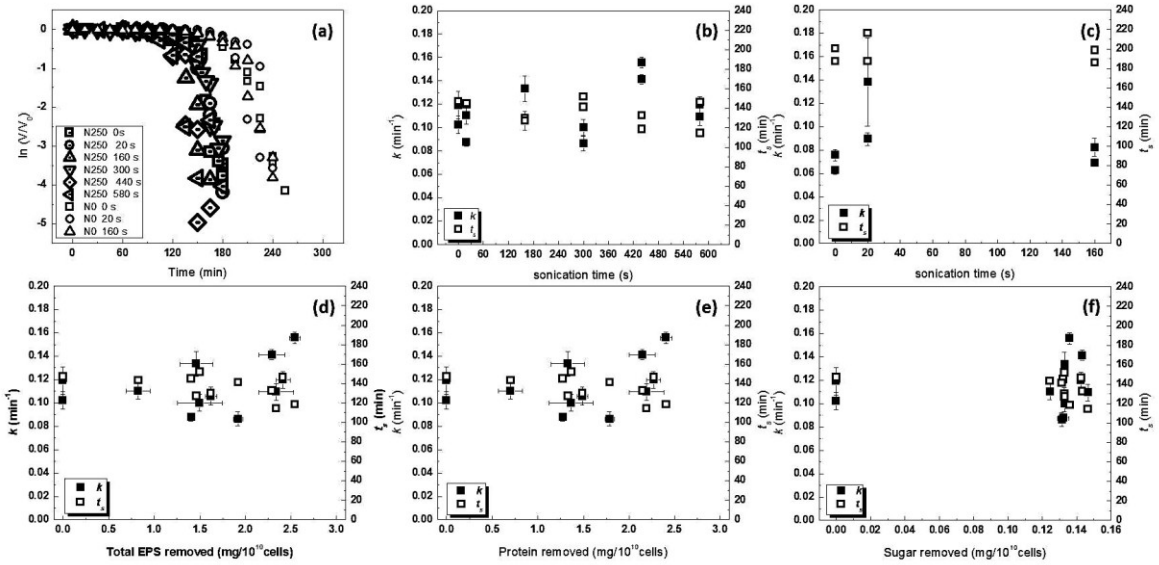

Figure A-4 *E. coli* was exposed to light ≥ 305 nm as a function of EPS level. (a) Changing viability in cell population due to *direct* (open symbols) and *indirect* (symbols with dot in center). Indirect disinfection experiments were conducted in the presence of 250 mg/L nitrate which generated $[\bullet OH]_{ss}=1.39 \times 10^{-15}$ M. Data are presented as the natural log of cell viability normalized by initial viability versus the time of light exposure. The remaining figures provide the rate constant, k (min^{-1}) and induction time, t_s (min) with respect to sonication times for experiments conducted (b) in the presence ($[\bullet OH]_{ss}=1.39\times10^{-15}$ M) and (c) absence ($[\bullet OH]_{ss}=0$) of photochemically generated hydroxyl radical. In panels (b) and (c), longer sonication times imply a greater extent of EPS removal. For systems conducted with $[\bullet OH]_{ss} = 1.39\times10^{-15}$ M, values of k and t_s are also shown with respect to (d) total EPS, (e) protein, and (f) sugar removed from cell surfaces.

Table A-2. Characterization of EPS content removed from bacterial surfaces by the sonication method.

Sample Name[1]	Total EPS Removed[2] (mg/per 10^{10} cells)	total EPS Stdev	Protein removed[3] (mg/per 10^{10} cells)	Protein Stdev	Sugar removed[4] (mg/per 10^{10} cells)	Sugar Stdev	SP ratio[5] (S/P)
DC1 30% 20s-1	0.825	0.132	0.701	0.132	0.124	0.001	0.178
DC1 30% 20s-2	1.405	0.021	1.273	0.022	0.132	0.003	0.104
DC1 30% 160s-1	1.622	0.061	1.489	0.061	0.133	0.000	0.089
DC1 30% 160s-2	1.463	0.182	1.330	0.182	0.133	0.000	0.100
DC1 30% 300s-1	1.500	0.243	1.367	0.243	0.133	0.000	0.097
DC1 30% 300s-2	1.920	0.052	1.788	0.051	0.131	0.001	0.074
DC1 30% 440s-1	2.291	0.143	2.148	0.143	0.143	0.000	0.067
DC1 30% 440s-2	2.543	0.062	2.407	0.063	0.136	0.001	0.057
DC1 30% 580s-1	2.340	0.192	2.193	0.192	0.147	0.001	0.067
DC1 30% 580s-2	2.413	0.078	2.271	0.078	0.143	0.001	0.063
DC1 30% 300s-1	1.981	0.077	1.850	0.078	0.131	0.001	0.071
DC1 30% 300s-2	1.379	0.120	1.239	0.119	0.140	0.002	0.114
HU1 30% 300s-1	1.312	0.072	1.172	0.070	0.140	0.002	0.120
HU1 30% 300s-2	1.306	0.112	1.163	0.110	0.143	0.003	0.123
SP4 30% 300s-1	1.741	0.070	1.595	0.071	0.145	0.001	0.091
SP4 30% 300s-2	1.118	0.091	0.982	0.091	0.136	0.001	0.139
O157:H7 30% 300s-1	1.590	0.109	1.448	0.108	0.142	0.000	0.098
O157:H7 30% 300s-2	1.160	0.164	0.990	0.162	0.170	0.001	0.175

[1]Sample name contain four part including 1)"DC1" *E. coli* strain type, 2)"30%" as sonication intensity, 3)"300s" as total sonication time, and 4)"-1" or "-2" means duplicates.

[2]Total EPS removed were calculated by adding sugar removed and protein removed together.

[3] Protein removed from bacterial surfaces by applying sonication in 30% intensity (45 watt) for varied lengths and analyzed with Lowry method.

[4] Sugar removed from bacterial surfaces by applying sonication in 30% intensity (45 watt) for varied lengths and analyzed with phenol-sulfuric acid method.

[5] SP ratios were calculated by dividing every sugar removed with according protein removed, the resulting value shows the relative characteristics of experimental condition.

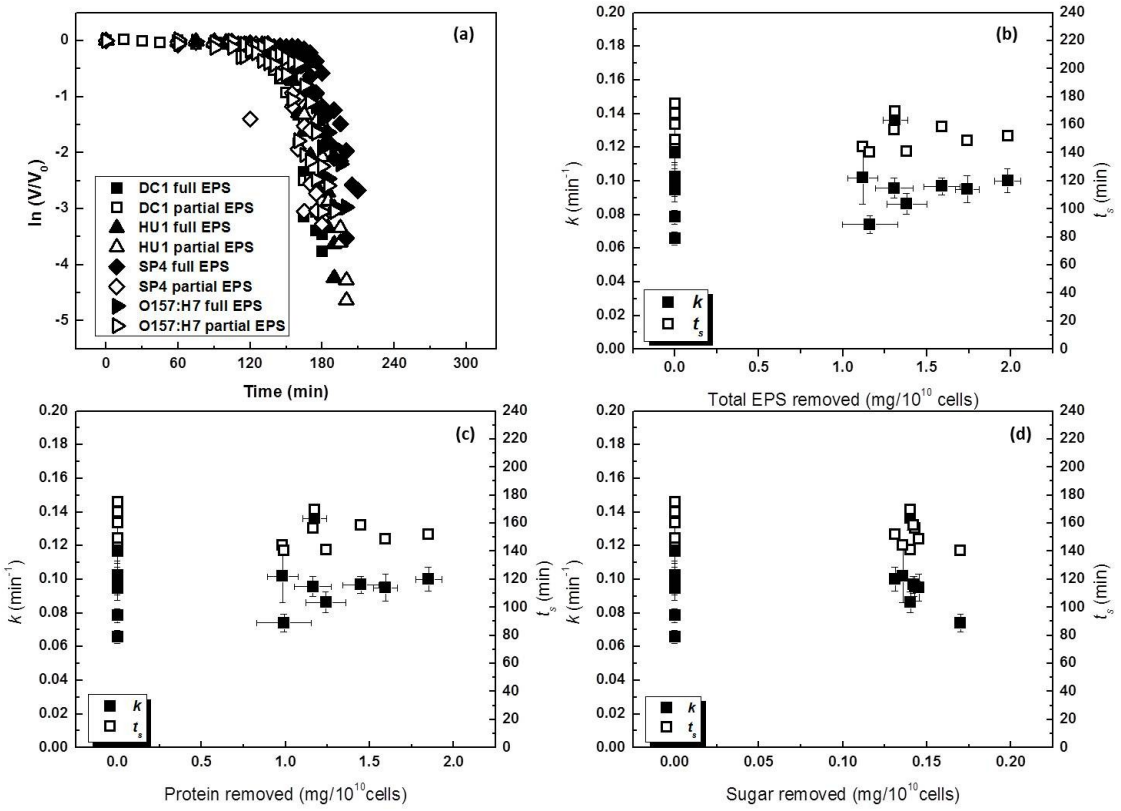

Figure A-5. Bacteria was exposed to light ≥305 nm as a function of EPS level. (a) Photochemical disinfection of *E. coli* strains DC1, HU1, SP4, and O157:H7 in the presence of a constant hydroxyl radical concentration ($[\bullet OH]_{ss}=1.39\times10^{-15}$ M). The EPS was removed via 300 s sonication and compared to full EPS presence. Data presented as the natural log of cell viability normalized by initial viability versus the time of light exposure. The remaining figures provide the rate constant, k (min^{-1}) and induction time, t_s (min) with respect to (b) total EPS, (c) protein, and (d) sugar removed from cell surfaces.

BIBLIOGRAPHY

1. Feyman, R.P. *There's Plenty of Room at the Bottom*. in *American Physical Society*. 1959. Pasadena, CA.

2. *The National Nanotechnology Initiative: Strategic Plan*, E. Nanoscale Science, and Technology Subcommittee, Editor 2011.

3. Turner, A., *Nanotechnology and Introduction*2008, Chandigrah, India: Global Media.

4. Hwang, Y.-N., S.-H. Park, and D. Kim, *Size-dependent surface phonon mode of CdSe quantum dots.* Physical Review B, 1999. 59(11): p. 7285-7288.

5. Wolf, E.L., *Nanophysics and Nanotechnology*2004, Weinheim, Germany: Wiley-VCH.

6. Lin, K.-F., et al., *Band gap variation of size-controlled ZnO quantum dots synthesized by sol–gel method.* Chemical Physics Letters, 2005. 409(4–6): p. 208-211.

7. Chernyshev, A.P., *Effect of nanoparticle size on the onset temperature of surface melting.* Materials Letters, 2009. 63(17): p. 1525-1527.

8. Li, H., et al., *Size-dependent melting point of nanoparticles based on bond number calculation.* Materials Chemistry and Physics, 2013. 137(3): p. 1007-1011.

9. Sun, J. and S.L. Simon, *The melting behavior of aluminum nanoparticles.* Thermochimica Acta, 2007. 463(1–2): p. 32-40.

10. Shetty, S., V.R. Palkar, and R. Pinto, *Size effect study in magnetoelectric BiFeO3 system.* Pramana, 2002. 58(5-6): p. 1027-1030.

11. Annapu Reddy, V., N.P. Pathak, and R. Nath, *Particle size dependent magnetic properties and phase transitions in multiferroic BiFeO3 nano-particles.* Journal of Alloys and Compounds, 2012. 543(0): p. 206-212.

12. Shong, C.W., S.C. Haur, and A.T. Wee, *Science At The Nanoscale*2010, Singapore: Pan Stanford Publishing Pte. Ltd.

13. Cui, C.-H. and S.-H. Yu, *Engineering Interface and Surface of Noble Metal Nanoparticle Nanotubes toward Enhanced Catalytic Activity for Fuel Cell Applications.* Accounts of Chemical Research, 2013.

14. Fan, C., et al., *Relationship between solubility and solubility product: The roles of crystal sizes and crystallographic directions.* Geochimica Et Cosmochimica Acta, 2006. 70(15): p. 3820-3829.

15. Auffan, M., et al., *Towards a definition of inorganic nanoparticles from an environmental, health and safety perspective.* Nature Nanotechnology, 2009. 4: p. 634-641.

16. Lindsay, W.L. and A.P. Schwab, *The chemistry of iron in soils and its availability to plants.* Journal of Plant Nutrition, 1982. 5(4-7): p. 821-840.

17. Boyd, P.W. and M.J. Ellwood, *The biogeochemical cycle of iron in the ocean.* Nature Geoscience, 2010. 3: p. 675-682.

18. Hochella, M.F., Jr., et al., *Nanominerals, Mineral Nanoparticles, and Earth Systems.* Science, 2008. 319(5870): p. 1631-1635.

19. Penn, R.L., et al., *Iron oxide coatings on sand grains from the Atlantic coastal plain: High-resolution transmission electron microscopy characterization.* Geology, 2001. 29(9): p. 843-846.

20. Raiswell, R., et al., *Contributions from glacially derived sediment to the global iron (oxyhydr)oxide cycle: Implications for iron delivery to the oceans.* Geochimica Et Cosmochimica Acta, 2006. 70(11): p. 2765-2780.

21. van der Zee, C., et al., *Nanogoethite is the dominant reactive oxyhydroxide phase in lake and marine sediments.* Geology, 2003. 31(11): p. 993-996.

22. Engelbrecht, J.P. and E. Derbyshire, *Airborne Mineral Dust.* ELEMENTS, 2010. 6(4): p. 241-246.

23. Raiswell, R., *Iron Transport from the Continents to the Open Ocean: The Aging–Rejuvenation Cycle.* ELEMENTS, 2011. 7(2): p. 101-106.

24. Cornell, R.M. and U. Schwertmann, *The Iron Oxides: Structure. Properties, Reactions, Occurences and Uses*. 2nd ed2003, Weinheim, Germany: Wiley-VCH.

25. Jambor, J.L. and D.W. Blowes, *The environmental geochemistry of sulfide mine wastes*1994, Nepean, Ont., Canada Mineralogical Association of Canada.

26. Rosso, K.M., et al., *Connecting Observations of Hematite (α-Fe_2O_3) Growth Catalyzed by Fe(II).* Environmental Science & Technology, 2009. 44(1): p. 61-67.

27. Kappler, A. and K.L. Straub, *Geomicrobiological Cycling of Iron.* Reviews in Mineralogy and Geochemistry, 2005. 59(1): p. 85-108.

28. Gupta, A.K. and M. Gupta, *Synthesis and surface engineering of iron oxide nanoparticles for biomedical applications.* Biomaterials, 2005. 26(18): p. 3995-4021.

29. Kaushik, A., et al., *Iron oxide nanoparticles–chitosan composite based glucose biosensor.* Biosensors and Bioelectronics, 2008. 24(4): p. 676-683.

30. Jang, J.S., et al., *Development of a Potential Fe2O3-Based Photocatalyst Thin Film for Water Oxidation by Scanning Electrochemical Microscopy: Effects of Ag−Fe2O3 Nanocomposite and Sn Doping.* Chemistry of Materials, 2009. 21(20): p. 4803-4810.

31. Beller, H.R., D. Grbić-Galić, and M. Reinhard, *Microbial degradation of toluene under sulfate-reducing conditions and the influence of iron on the process.* Applied and Environmental Microbiology, 1992. 58(3): p. 786-793.

32. Boyd, P.W., et al., *A mesoscale phytoplankton bloom in the polar Southern Ocean stimulated by iron fertilization.* Nature, 2000. 407(6805): p. 695.

33. Ridgwell, A.J., *Dust in the Earth System: The Biogeochemical Linking of Land, Air and Sea.* Philosophical Transactions: Mathematical, Physical and Engineering Sciences, 2002. 360(1801): p. 2905-2924.

34. Smetacek, V., et al., *Deep carbon export from a Southern Ocean iron-fertilized diatom bloom.* Nature, 2012. 487(7407): p. 313-319.

35. Lindsay, W., *Solubility and Redox Equilibria of Iron Compounds in Soils*, in *Iron in Soils and Clay Minerals*, J.W. Stucki, B.A. Goodman, and U. Schwertmann, Editors. 1987, Springer Netherlands. p. 37-62.

36. NIST, *NIST Critically Selected Stability Constants of Metal Complexes Database*, U.S.D.o. Commerce, Editor 2004: Washington DC.

37. Adamson, A.W., *Physical Chemistry of Surfaces*. 4 ed1982, New York: Wiley.

38. Hochella, M.F., *There's plenty of room at the bottom: nanoscience in geochemistry.* Geochimica Et Cosmochimica Acta, 2002. 66(5): p. 735-743.

39. Trolard, F. and Y. Tardy, *The stabilities of gibbsite, boehmite, aluminous goethites and aluminous hematites in bauxites, ferricretes and laterites as a function of water activity, temperature and particle size.* Geochimica Et Cosmochimica Acta, 1987. 51(4): p. 945-957.

40. Postma, D., *The reactivity of iron oxides in sediments: A kinetic approach.* Geochimica Et Cosmochimica Acta, 1993. 57(21–22): p. 5027-5034.

41. Cornell, R.M. and R. Giovanoli, *Acid dissolution of hematites of different morphologies.* Clay Minerals, 1993. 28(2): p. 223-232.

42. Schwertmann, U., *Solubility and dissolution of iron oxides.* Plant and Soil, 1991. 130(1-2): p. 1-25.

43. Duckworth, O.W. and S.T. Martin, *Surface complexation and dissolution of hematite by C1-C6 dicarboxylic acids at pH = 5.0.* Geochimica Et Cosmochimica Acta, 2001. 65(23): p. 4289-4301.

44. Kraemer, S., *Iron oxide dissolution and solubility in the presence of siderophores.* Aquatic Sciences, 2004. 66(1): p. 3-18.

45. Lindsay, W.L., *Iron oxide solubilization by organic matter and its effect on iron availability*, in *Iron Nutrition and Interactions in Plants*, Y. Chen and Y. Hadar, Editors. 1991, Springer Netherlands. p. 29-36.

46. Zhang, Y., N. Kallay, and E. Matijevic, *Interaction of metal hydrous oxides with chelating agents. 7. Hematite-oxalic acid and -citric acid systems.* Langmuir, 1985. 1(2): p. 201-206.

47. Dos Santos Afonso, M. and W. Stumm, *Reductive dissolution of iron(III) (hydr)oxides by hydrogen sulfide.* Langmuir, 1992. 8(6): p. 1671-1675.

48. Schwarzenbach, R.P., P.M. Gschwend, and D.M. Imboden, *Environmental Organic Chemistry* 2003, Hoboken, New Jersey: John Wiley & Sons, Inc.

49. Stack, A.G., et al., *Reaction of hydroquinone with hematite: II. Calculated electron-transfer rates and comparison to the reductive dissolution rate.* Journal of Colloid and Interface Science, 2004. 274(2): p. 442-450.

50. Pedersen, H.D., et al., *Fast transformation of iron oxyhydroxides by the catalytic action of aqueous Fe(II).* Geochimica Et Cosmochimica Acta, 2005. 69(16): p. 3967-3977.

51. Roden, E.E. and J.M. Zachara, *Microbial Reduction of Crystalline Iron(III) Oxides: Influence of Oxide Surface Area and Potential for Cell Growth.* Environmental Science & Technology, 1996. 30(5): p. 1618-1628.

52. Roden, E.E., *Geochemical and microbiological controls on dissimilatory iron reduction.* Comptes Rendus Geoscience, 2006. 338(6–7): p. 456-467.

53. Dos Santos Afonso, M., et al., *The reductive dissolution of iron oxides by ascorbate : The role of carboxylate anions in accelerating reductive dissolution.* Journal of Colloid and Interface Science, 1990. 138(1): p. 74-82.

54. Larsen, O. and D. Postma, *Kinetics of reductive bulk dissolution of lepidocrocite, ferrihydrite, and goethite.* Geochimica Et Cosmochimica Acta, 2001. 65(9): p. 1367-1379.

55. Siffert, C. and B. Sulzberger, *Light-induced dissolution of hematite in the presence of oxalate. A case study.* Langmuir, 1991. 7(8): p. 1627-1634.

56. Sulzberger, B. and H. Laubscher, *Reactivity of various types of iron(III) (hydr)oxides towards light-induced dissolution.* Marine Chemistry, 1995. 50(1-4): p. 103-115.

57. Madden, A.S. and M.F. Hochella Jr, *A test of geochemical reactivity as a function of mineral size: Manganese oxidation promoted by hematite nanoparticles.* Geochimica Et Cosmochimica Acta, 2005. 69(2): p. 389-398.

58. Barton, L.E., et al., *Size-Dependent Pb Sorption to Nanohematite in the Presence and Absence of a Microbial Siderophore.* Environmental Science & Technology, 2011. 45(8): p. 3231-3237.

59. Cwiertny, D.M., et al., *Surface Chemistry and Dissolution of alpha-FeOOH Nanorods and Microrods: Environmental Implications of Size-Dependent Interactions with Oxalate.* Journal of Physical Chemistry C, 2009. 113(6): p. 2175-2186.

60. Anschutz, A. and R.L. Penn, *Reduction of crystalline iron(III) oxyhydroxides using hydroquinone: Influence of phase and particle size.* Geochemical Transactions, 2005. 6(3): p. 60.

61. Echigo, T., et al., *Influence of size, morphology, surface structure, and aggregation state on reductive dissolution of hematite nanoparticles with ascorbic acid.* Geochimica Et Cosmochimica Acta, 2012. 90(0): p. 149-162.

62. Echigo, T., et al., *Nanopores in hematite (α-Fe2O3) nanocrystals observed by electron tomography.* American Mineralogist, 2013. 98(1): p. 154-162.

63. Rubasinghege, G., et al., *Simulated atmospheric processing of iron oxyhydroxide minerals at low pH: Roles of particle size and acid anion in iron dissolution.* Proceedings of the National Academy of Sciences, 2010. 107(15): p. 6628-6633.

64. Rubasinghege, G., et al., *Nanorod Dissolution Quenched in the Aggregated State.* Langmuir, 2009. 26(3): p. 1524-1527.

65. Rubasinghege, G., et al., *Proton-promoted dissolution of α-FeOOH nanorods and microrods: Size dependence, anion effects (carbonate and phosphate), aggregation and surface adsorption.* Journal of Colloid and Interface Science, 2010(0).

66. Gregg, S.J. and K.S.W. Sing, *Adsorption, surface area and porosity*. 2 ed1991, London: Academic Press.

67. Brunauer, S., P.H. Emmett, and E. Teller, *Adsorption of Gases in Multimolecular Layers.* Journal of the American Chemical Society, 1938. 60(2): p. 309-319.

68. Colombo, C., V. Barrón, and J. Torrent, *Phosphate adsorption and desorption in relation to morphology and crystal properties of synthetic hematites.* Geochimica Et Cosmochimica Acta, 1994. 58(4): p. 1261-1269.

69. Hiemstra, T., et al., *Nanoparticles in natural systems I: The effective reactive surface area of the natural oxide fraction in field samples.* Geochimica Et Cosmochimica Acta, 2010. 74(1): p. 41-58.

70. Santamarina, J.C., et al., *Specific surface: determination and relevance.* Canadian Geotechnical Journal, 2002. 39(1): p. 233-241.

71. Breeuwsma, A. and J. Lyklema, *Interfacial electrochemistry of haematite ([small alpha]-Fe2O3).* Discussions of the Faraday Society, 1971. 52: p. 324-333.

72. Fokkink, L.G.J., A. de Keizer, and J. Lyklema, *Temperature dependence of the electrical double layer on oxides: Rutile and hematite.* Journal of Colloid and Interface Science, 1989. 127(1): p. 116-131.

73. Tipping, E. and M. Ohnstad, *Colloid stability of iron oxide particles from a freshwater lake.* Nature, 1984. 308(5956): p. 266-268.

74. Liang, L. and J.J. Morgan, *Chemical aspects of iron oxide coagulation in water: Laboratory studies and implications for natural systems.* Aquatic Sciences - Research Across Boundaries, 1990. 52(1): p. 32-55.

75. Amal, R., J.A. Raper, and T.D. Waite, *Effect of fulvic acid adsorption on the aggregation kinetics and structure of hematite particles.* Journal of Colloid and Interface Science, 1992. 151(1): p. 244-257.

76. Baalousha, M., et al., *Aggregation and surface properties of iron oxide nanoparticles: Influence of ph and natural organic matter.* Environmental Toxicology and Chemistry, 2008. 27(9): p. 1875-1882.

77. Raiswell, R., et al., *The determination of labile Fe in ferrihydrite by ascorbic acid extraction: Methodology, dissolution kinetics and loss of solubility with age and de-watering.* Chemical Geology, 2010. 278(1–2): p. 70-79.

78. Gilbert, B., et al., *The effects of nanoparticle aggregation processes on aggregate structure and metal uptake.* Journal of Colloid and Interface Science, 2009. 339(2): p. 285-295.

79. Gilbert, B., G. Lu, and C.S. Kim, *Stable cluster formation in aqueous suspensions of iron oxyhydroxide nanoparticles.* Journal of Colloid and Interface Science, 2007. 313(1): p. 152-159.

80. Mylon, S.E., K.L. Chen, and M. Elimelech, *Influence of Natural Organic Matter and Ionic Composition on the Kinetics and Structure of Hematite Colloid Aggregation: Implications to Iron Depletion in Estuaries.* Langmuir, 2004. 20(21): p. 9000-9006.

81. He, Y., J. Wan, and T. Tokunaga, *Kinetic stability of hematite nanoparticles: the effect of particle sizes.* Journal of Nanoparticle Research, 2008. 10(2): p. 321-332.

82. Bligh, M.W. and T.D. Waite, *Formation, reactivity, and aging of ferric oxide particles formed from Fe(II) and Fe(III) sources: Implications for iron bioavailability in the marine environment.* Geochimica Et Cosmochimica Acta, 2011. 75(24): p. 7741-7758.

83. Hofmann, A., et al., *Characterization of the pores in hydrous ferric oxide aggregates formed by freezing and thawing.* Journal of Colloid and Interface Science, 2004. 271(1): p. 163-173.

84. Cwiertny, D.M., et al., *Interpreting nanoscale size-effects in aggregated Fe-oxide suspensions: Reaction of Fe(II) with Goethite.* Geochimica Et Cosmochimica Acta, 2008. 72(5): p. 1365-1380.

85. Yanina, S.V. and K.M. Rosso, *Linked Reactivity at Mineral-Water Interfaces Through Bulk Crystal Conduction.* Science, 2008. 320(5873): p. 218-222.

86. Larese-Casanova, P. and M.M. Scherer, *Fe(II) Sorption on Hematite: New Insights Based on Spectroscopic Measurements.* Environmental Science & Technology, 2006. 41(2): p. 471-477.

87. Handler, R.M., et al., *Atom Exchange between Aqueous Fe(II) and Goethite: An Fe Isotope Tracer Study.* Environmental Science & Technology, 2009. 43(4): p. 1102-1107.

88. Kwan, W.P. and B.M. Voelker, *Decomposition of Hydrogen Peroxide and Organic Compounds in the Presence of Dissolved Iron and Ferrihydrite.* Environmental Science & Technology, 2002. 36(7): p. 1467-1476.

89. Voelker, B.M., F.M.M. Morel, and B. Sulzberger, *Iron Redox Cycling in Surface Waters: Effects of Humic Substances and Light.* Environmental Science & Technology, 1997. 31(4): p. 1004-1011.

90. Cooper, W.J., et al., *Photochemical formation of hydrogen peroxide in natural waters exposed to sunlight.* Environmental Science & Technology, 1988. 22(10): p. 1156-1160.

91. Cooper William, J., et al., *Sunlight-Induced Photochemistry of Humic Substances in Natural Waters: Major Reactive Species*, in *Aquatic Humic Substances*1988, American Chemical Society. p. 333-362.

92. Huston, P.L. and J.J. Pignatello, *Degradation of selected pesticide active ingredients and commercial formulations in water by the photo-assisted Fenton reaction.* Water Research, 1999. 33(5): p. 1238-1246.

93. Belaidi, S., et al., *Photodegradation kinetics of 2,6-dimetylphenol by natural iron oxide and oxalate in aqueous solution.* Journal of Photochemistry and Photobiology A: Chemistry, 2012. 237(0): p. 31-37.

94. Cho, M., et al., *Inactivation of Escherichia coli by Photochemical Reaction of Ferrioxalate at Slightly Acidic and Near-Neutral pHs.* Appl. Environ. Microbiol., 2004. 70(2): p. 1129-1134.

95. Nieto-Juarez, J.I., et al., *Inactivation of MS2 coliphage in Fenton and Fenton-like systems: role of transition metals, hydrogen peroxide and sunlight.* Environmental Science & Technology, 2010. 44(9): p. 3351-3356.

96. Vermilyea, A.W. and B.M. Voelker, *Photo-Fenton Reaction at Near Neutral pH.* Environmental Science & Technology, 2009. 43(18): p. 6927-6933.

97. Hu, Y.-S., et al., *Pt-Doped α-Fe2O3 Thin Films Active for Photoelectrochemical Water Splitting.* Chemistry of Materials, 2008. 20(12): p. 3803-3805.

98. Wheeler, D.A., et al., *Nanostructured hematite: synthesis, characterization, charge carrier dynamics, and photoelectrochemical properties.* Energy & Environmental Science, 2012. 5(5): p. 6682-6702.

99. Rubasinghege, G., et al., *Reactions on Atmospheric Dust Particles: Surface Photochemistry and Size-Dependent Nanoscale Redox Chemistry.* The Journal of Physical Chemistry Letters, 2010. 1(11): p. 1729-1737.

100. Elzey, S. and V.H. Grassian, *Agglomeration, isolation and dissolution of commercially manufactured silver nanoparticles in aqueous environments.* J. Nanopart. Res., 2010. 12: p. 1945-1958.

101. Meulenkamp, E.A., *Size dependence of the dissolution of ZnO nanoparticles.* J. Phys. Chem. B., 1998. 102: p. 7764-7769.

102. Mudunkotuwa, I.A., et al., *Dissolution of ZnO nanoparticles at circumneutal pH: a study of size effects in the presence and absence of citric acid.* Langmuir, 2012. 28: p. 396-403.

103. Liu, J., et al., *Influene of size and aggregation on the reactivity of an environmentally and industrially relevant nanomaterial (PbS).* Environ. Sci. Technol., 2009. 43: p. 8178-8183.

104. Waychunas, G.A., C.S. Kim, and J.F. Banfield, *Nanoparticulate Iron Oxide Minerals in Soils and Sediments: Unique Properties and Contaminant Scavenging Mechanisms.* Journal of Nanoparticle Research, 2005. 7(4): p. 409-433.

105. Banfield, J.F. and H. Zhang, *Nanoparticles in the Environment*, in *Reviews in Mineralogy and Geochemistry: Nanoparticles and the Environment*, J.F. Banfield and A. Navrotsky, Editors. 2001 The Mineralogical Society of America: Washington, D.C. p. 1-58.

106. Shi, Z., et al., *Impacts on iron solubility in the mineral dust by processes in the source region and the atmosphere: A review.* Aeolian Research, 2012. 5(0): p. 21-42.

107. Madden, A.S., M.F. Hochella Jr, and T.P. Luxton, *Insights for size-dependent reactivity of hematite nanomineral surfaces through Cu2+ sorption.* Geochimica Et Cosmochimica Acta, 2006. 70(16): p. 4095-4104.

108. Erbs, J.J., B. Gilbert, and R.L. Penn, *Influence of Size on Reductive Dissolution of Six-Line Ferrihydrite.* The Journal of Physical Chemistry C, 2008. 112(32): p. 12127-12133.

109. Grassian, V.H., *When Size Really Matters: Size-Dependent Properties and Surface Chemistry of Metal and Metal Oxide Nanoparticles in Gas and Liquid Phase Environmentsâ€* The Journal of Physical Chemistry C, 2008. 112(47): p. 18303-18313.

110. Chernyshova, I.V., M.F. Hochella, Jr., and A.S. Madden, *Size-dependent structural transformation of hematite nanoparticles. 1. phase transition.* Phys. Chem. Chem. Phys., 2007. 9: p. 1736-1750.

111. Maurice, P.A.H., M. F. ;Parks, G.A.; Sposito, G.;Schwertmann, U., *Evolution of Hematite Surface Microtopography Upon Dissolution By Simple Organic Acids.* Clays and Clay Minerals, 1995. 43(1): p. 29-38.

112. Eggleston, C.M., et al., *The structure of hematite (α-Fe2O3) (001) surfaces in aqueous media: scanning tunneling microscopy and resonant tunneling calculations of coexisting O and Fe terminations.* Geochimica Et Cosmochimica Acta, 2003. 67(5): p. 985-1000.

113. Rustad, J.R. and A.R. Felmy, *The influence of edge sites on the development of surface charge on goethite nanoparticles: A molecular dynamics investigation.* Geochimica Et Cosmochimica Acta, 2005. 69(6): p. 1405-1411.

114. Villalobos, M., M.A. Trotz, and J.O. Leckie, *Variability in goethite surface site density: evidence from proton and carbonate sorption.* Journal of Colloid and Interface Science, 2003. 268(2): p. 273-287.

115. Vikesland, P.J., et al., *Particle Size and Aggregation Effects on Magnetite Reactivity toward Carbon Tetrachloride.* Environmental Science & Technology, 2007. 41(15): p. 5277-5283.

116. Bligh, M.W. and T.D. Waite, *Formation, aggregation and reactivity of amorphous ferric oxyhydroxides on dissociation of Fe(III)–organic complexes in dilute aqueous suspensions.* Geochimica Et Cosmochimica Acta, 2010. 74(20): p. 5746-5762.

117. Sorum, S.H., *The preparation of chloride free, colloidial Fe_2O_3 from $FeCl_3$.* J Am. Chem. Soc., 1928(50): p. 1263-1267.

118. Schwertmann, U. and R.M. Cornell, *Iron Oxides in the Laboratory: Preparation and Characterization*. 2nd ed2000, New York: WILEY-VCH.

119. Hatchard, C.G. and C.A. Parker, *A New Sensitive Chemical Actinometer. II. Potassium Ferrioxalate as a Standard Chemical Actinometer.* Proceedings of the Royal Society of London. Series A, Mathematical and Physical Sciences, 1956. 235(1203): p. 518-536.

120. Goldstein, S. and J. Rabani, *The ferrioxalate and iodide-iodate actinometers in the UV region.* Journal of Photochemistry and Photobiology A: Chemistry, 2008. 193(1): p. 50-55.

121. Stucki, J.W. and W.L. Anderson, *The quantitative assay of minerals for Fe2+ and Fe3+ using 1,10-phenanthroline. I. sources of variability.* Soil Science Society of America Journal, 1981. 45(633-637).

122. Stucki, J.W., *The quantitative assay of minerals for Fe2+ and Fe3+ using 1,10-phenanthroline. II. A photochemical method.* Soil Science Society of America Journal, 1981. 45: p. 638-641.

123. Cornell, R.M., A.M. Posner, and J.P. Quirk, *Kinetics and mechanisms of the acid dissolution of goethite ([alpha]-FeOOH).* Journal of Inorganic and Nuclear Chemistry, 1976. 38(3): p. 563-567.

124. Banwart, S., S. Davies, and W. Stumm, *The role of oxalate in accelerating the reductive dissolution of hematite (α-Fe2O3) by ascorbate.* Colloids and Surfaces, 1989. 39(2): p. 303-309.

125. Suter, D., S. Banwart, and W. Stumm, *Dissolution of hydrous iron(III) oxides by reductive mechanisms.* Langmuir, 1991. 7(4): p. 809-813.

126. Cwiertny, D.M., M.A. Young, and V.H. Grassian, *Chemistry and photochemistry of mineral dust aerosol.* Annual Review of Physical Chemistry, 2008. 59: p. 27-51.

127. Jickells, T.D., et al., *Global iron connections between desert dust, ocean biogeochemistry and climate.* Science, 2005. 308(5718): p. 67-71.

128. Dehner, C.A., et al., *Size-Dependent Bioavailability of Hematite (α-Fe2O3) Nanoparticles to a Common Aerobic Bacterium.* Environmental Science & Technology, 2010. 45(3): p. 977-983.

129. Dehner, C.A., et al., *Roles of siderophores, oxalate and ascorbate in mobilization of iron from hematite by the aerobic bacterium Pseudomonas mendocina.* Appl. Environ. Microbiol., 2010. 76: p. 2041-2048.

130. Barton, L.E., A.N. Quicksall, and P.A. Maurice, *Siderophore-mediated dissolution of hematite (α-Fe_2O_3): effects of nanoparticle size.* Geomicrobiology Journal, 2012. 29: p. 314-322.

131. Catalano, J.G., et al., *Structure and oxidation state of hematite surfaces reacted with aqueous Fe(II) at acidic and neutral pH.* Geochimica Et Cosmochimica Acta, 2010. 74(5): p. 1498-1512.

132. Frierdich, A.J., Y. Luo, and J.G. Catalano, *Trace element cycling through iron oxide minerals during redox-driven dynamic recrystallization.* Geology, 2011. 39: p. 1083-1086.

133. Frierdich, A.J. and J.G. Catalano, *Controls on Fe(II)-activated trace element release from goethite.* Environ. Sci. Technol., 2011. 46: p. 1519-1526.

134. Southworth, B.A. and B.M. Voelker, *Hydroxyl Radical Production via the Photo-Fenton Reaction in the Presence of Fulvic Acid.* Environmental Science & Technology, 2003. 37(6): p. 1130-1136.

135. Bodker, F. and S. Morup, *Size dependence of the properties of hematite nanoparticles.* Europhysics Letters, 2000. 52(2): p. 217-223.

136. Lanzl, C.A., J. Baltrusaitis, and D.M. Cwiertny, *Dissolution of Hematite Nanoparticle Aggregates: Influence of Primary Particle Size, Dissolution Mechanism, and Solution pH.* Langmuir, 2012. 28(45): p. 15797-15808.

137. Behra, P. and L. Sigg, *Evidence for redox cycling of iron in atmospheric water droplets.* Nature, 1990. 344(6265): p. 419-421.

138. Deng, Y. and W. Stumm, *Reactivity of aquatic iron(III) oxyhydroxides—implications for redox cycling of iron in natural waters.* Applied Geochemistry, 1994. 9(1): p. 23-36.

139. Klausen, J., et al., *Reduction of Substituted Nitrobenzenes by Fe(II) in Aqueous Mineral Suspensions.* Environmental Science & Technology, 1995. 29(9): p. 2396-2404.

140. Wielinga, B., et al., *Iron Promoted Reduction of Chromate by Dissimilatory Iron-Reducing Bacteria.* Environmental Science & Technology, 2000. 35(3): p. 522-527.

141. Stumm, W. and J.J. Morgan, *Aquatic Chemistry Chemical Equilibira and Rates in Natural Waters*. 3 ed. 1996, New York, NY: John Wiley & Sons, Inc.

142. Verway, E.J.W. and J.T.G. Overbeek, *Theory of the Stabilility of Lyphobic Colloids*1948, Amsterdam: Elsevier.

143. Breeuwsma, A. and J. Lyklema, *Physical and chemical adsorption of ions in the electrical double layer on hematite (α-Fe2O3).* Journal of Colloid and Interface Science, 1973. 43(2): p. 437-448.

144. Schudel, M., et al., *Absolute Aggregation Rate Constants of Hematite Particles in Aqueous Suspensions: A Comparison of Two Different Surface Morphologies.* Journal of Colloid and Interface Science, 1997. 196(2): p. 241-253.

145. Maximova, N. and O. Dahl, *Environmental implications of aggregation phenomena: Current understanding.* Current Opinion in Colloid & Interface Science, 2006. 11(4): p. 246-266.

146. Baalousha, M., *Aggregation and disaggregation of iron oxide nanoparticles: Influence of particle concentration, pH and natural organic matter.* Science of The Total Environment, 2009. 407(6): p. 2093-2101.

147. Smoluchowski, M., *Versuch einer mathematischen Theorie der Koagulationskinetik kolloider Lösungen.* Zeitschrift für Physikalische Chemie, 1917(92): p. 129-168.

148. Ferretti, R., J. Zhang, and J. Buffle, *Kinetics of hematite aggregation by polyacrylic acid: effect of polymer molecular weights.* Colloids and Surfaces A: Physicochemical and Engineering Aspects, 1997. 121(2–3): p. 203-215.

149. Ji, Y.-Q., et al., *Hydrophobic coagulation and aggregation of hematite particles with sodium dodecylsulfate.* Colloids and Surfaces A: Physicochemical and Engineering Aspects, 2007. 298(3): p. 235-244.

150. Burleson, D.J. and R.L. Penn, *Two-Step Growth of Goethite from Ferrihydrite.* Langmuir, 2005. 22(1): p. 402-409.

151. Bushell, G.C., et al., *On techniques for the measurement of the mass fractal dimension of aggregates.* Advances in Colloid and Interface Science, 2002. 95(1): p. 1-50.

152. Tang, P. and J.A. Raper, *Modelling the settling behaviour of fractal aggregates–a review.* Powder Technology, 2002. 123(2–3): p. 114-125.

153. Lanzl, C.A. and D.M. Cwiertny, *Unpublished work: Fe(II) uptake onto 8 and 40 nm hematite at pH 7*, 2013, University of Iowa.

154. Wang, C.-y., et al., *A comparative study of nanometer sized Fe(iii)-doped TiO2 photocatalysts: synthesis, characterization and activity.* Journal of Materials Chemistry, 2003. 13(9): p. 2322-2329.

155. Williams, A.G.B. and M.M. Scherer, *Spectroscopic Evidence for Fe(II)âˆ'Fe(III) Electron Transfer at the Iron Oxide-Water Interface.* Environmental Science & Technology, 2004. 38(18): p. 4782-4790.

156. Baker, A.R. and T.D. Jickells, *Mineral particle size as a control on aerosol iron solubility.* Geophysical Research Letters, 2006. 33(17).

157. Zepp, R.G., B.C. Faust, and J. Hoigne, *Hydroxyl radical formation in aqueous reactions (pH 3-8) of iron(II) with hydrogen peroxide: the photo-Fenton reaction.* Environmental Science & Technology, 1992. 26(2): p. 313-319.

158. Borer, P., et al., *Photodissolution of lepidocrocite (γ-FeOOH) in the presence of desferrioxamine B and aerobactin.* Geochimica Et Cosmochimica Acta, 2009. 73(16): p. 4673-4687.

159. Zinder, B., G. Furrer, and W. Stumm, *The coordination chemistry of weathering: II. Dissolution of Fe(III) oxides.* Geochimica Et Cosmochimica Acta, 1986. 50(9): p. 1861-1869.

160. Garg, S., A.L. Rose, and T.D. Waite, *Photochemical production of superoxide and hydrogen peroxide from natural organic matter.* Geochimica Et Cosmochimica Acta, 2011. 75(15): p. 4310-4320.

161. Ritchie, J.D. and E.M. Perdue, *Proton-binding study of standard and reference fulvic acids, humic acids, and natural organic matter.* Geochimica Et Cosmochimica Acta, 2003. 67(1): p. 85-96.

162. *International Humic Substance Society*. 2013 [cited 2013 4/8/2013]; Available from: http://www.humicsubstances.org/.

163. Kochany, J. and J.R. Bolton, *Mechanism of photodegradation of aqueous organic pollutants. 1. EPR spin-trapping technique for the determination of hydroxyl radical rate constants in the photooxidation of chlorophenols following the photolysis of hydrogen peroxide.* The Journal of Physical Chemistry, 1991. 95(13): p. 5116-5120.

164. Bader, H., V. Sturzenegger, and J. Hoigné, *Photometric method for the determination of low concentrations of hydrogen peroxide by the peroxidase catalyzed oxidation of N,N-diethyl-p-phenylenediamine (DPD).* Water Research, 1988. 22(9): p. 1109-1115.

165. Au, K.-K., et al., *Natural organic matter at oxide/water interfaces: complexation and conformation.* Geochimica Et Cosmochimica Acta, 1999. 63(19–20): p. 2903-2917.

166. Zhang, Y., R. Del Vecchio, and N.V. Blough, *Investigating the Mechanism of Hydrogen Peroxide Photoproduction by Humic Substances.* Environmental Science & Technology, 2012. 46(21): p. 11836-11843.

167. Miller, G.W., et al., *Hydrogen peroxide method intercomparision study in seawater.* Marine Chemistry, 2005. 97(1–2): p. 4-13.

168. King, D.W., et al., *Flow Injection Analysis of H2O2 in Natural Waters Using Acridinium Ester Chemiluminescence: Method Development and Optimization Using a Kinetic Model.* Analytical Chemistry, 2007. 79(11): p. 4169-4176.

169. Kwan, W.P. and B.M. Voelker, *Influence of Electrostatics on the Oxidation Rates of Organic Compounds in Heterogeneous Fenton Systems.* Environmental Science & Technology, 2004. 38(12): p. 3425-3431.

170. Nakatani, N., et al., *Contribution of the Photo-Fenton Reaction to Hydroxyl Radical Formation Rates in River and Rain Water Samples.* Analytical Sciences, 2007. 23(9): p. 1137-1142.

171. Arakaki, T., et al., *Chemical composition and photochemical formation of hydroxyl radicals in aqueous extracts of aerosol particles collected in Okinawa, Japan.* Atmospheric Environment, 2006. 40(25): p. 4764-4774.

172. Rodriguez, R.D., et al., *Rhombohedral Shape of Hematite Nanocrystals Synthesized via Thermolysis of an Additive-free Ferric Chloride Solution.* The Journal of Physical Chemistry C, 2007. 111(45): p. 16866-16870.

173. Tanwar, K.S., et al., *Structural study of Fe(II) adsorption on hematite.* Geochimica Et Cosmochimica Acta, 2008. 72(14): p. 3311-3325.

174. Eggleston, C., et al., *Adatom Fe(III) on the hematite surface: Observation of a key reactive surface species.* Geochemical Transactions, 2004. 5(2): p. 33.

175. Wang, X.G., et al., *The Hematite (α- Fe_2O_3) (0001) Surface: Evidence for Domains of Distinct Chemistry.* Physical Review Letters, 1998. 81(5): p. 1038-1041.

176. Hardee, K.L. and A.J. Bard, *Semiconductor Electrodes V. The Application of Chemically Vapor Deposited Iron Oxide Films to Photosensitized Electrolysis.* Journal of The Electrochemical Society, 1976. 123(7): p. 1024-1026.

177. Cesar, I., et al., *Influence of Feature Size, Film Thickness, and Silicon Doping on the Performance of Nanostructured Hematite Photoanodes for Solar Water Splitting.* The Journal of Physical Chemistry C, 2008. 113(2): p. 772-782.

178. Boily, J.-F., et al., *Modeling proton binding at the goethite (α-FeOOH)–water interface.* Colloids and Surfaces A: Physicochemical and Engineering Aspects, 2001. 179(1): p. 11-27.

179. Vayssieres, L., et al., *One-Dimensional Quantum-Confinement Effect in α-Fe2O3 Ultrafine Nanorod Arrays.* Advanced Materials, 2005. 17(19): p. 2320-2323.

180. Friedmann, D., C. Mendive, and D. Bahnemann, *TiO2 for water treatment: Parameters affecting the kinetics and mechanisms of photocatalysis.* Applied Catalysis B: Environmental, 2010. 99(3–4): p. 398-406.

181. Kumar, P., et al., *Electrodeposited zirconium-doped α-Fe2O3 thin film for photoelectrochemical water splitting.* International Journal of Hydrogen Energy, 2011. 36(4): p. 2777-2784.

182. Kumari, S., et al., *Spray pyrolytically deposited nanoporous Ti4+ doped hematite thin films for efficient photoelectrochemical splitting of water.* International Journal of Hydrogen Energy, 2010. 35(9): p. 3985-3990.

183. Zepp, R.G., J. Hoigne, and H. Bader, *Nitrate-induced photooxidation of trace organic-chemicals in water.* Environmental Science & Technology, 1987. 21(5): p. 443-450.

184. Alif, A. and P. Boule, *Photochemistry and environment Part XIV. Phototransformation of nitrophenols induced by excitation of nitrite and nitrate ions.* Journal of Photochemistry and Photobiology, A: Chemistry, 1991. 59(3): p. 357-367.

185. Davies-Colley, R.J., A.M. Donnison, and D.J. Speed, *Sunlight wavelengths inactivating faecal indicator microorganisms in waste stabilisation ponds.* Water Science and Technology, 1997. 35(11-12): p. 219-225.

186. Kohn, T. and K.L. Nelson, *Sunlight-mediated inactivation of MS2 coliphage via exogenous singlet oxygen produced by sensitizers in natural waters.* Environmental Science & Technology, 2007. 41(1): p. 192-197.

187. Alkan, U., et al., *Efficiency of the UV/H2O2 process for the disinfection of humic surface waters.* Journal of Environmental Science and Health Part a-Toxic/Hazardous Substances & Environmental Engineering, 2007. 42(4): p. 497-506.

188. Mamane, H., H. Shemer, and K.G. Linden, *Inactivation of E-coli, B-subtilis spores, and MS2, T4, and T7 phage using UV/H2O2 advanced oxidation.* Journal of Hazardous Materials, 2007. 146(3): p. 479-486.

189. Salih, F.M., *Enhancement of solar inactivation of Escherichia coli by titanium dioxide photocatalytic oxidation.* Journal of Applied Microbiology, 2002. 92(5): p. 920-926.

190. Rincón, A.-G. and C. Pulgarin, *Bactericidal action of illuminated TiO2 on pure Escherichia coli and natural bacterial consortia: post-irradiation events in the dark and assessment of the effective disinfection time.* Applied Catalysis B: Environmental, 2004. 49(2): p. 99-112.

191. Gogniat, G., et al., *The bactericidal effect of TiO2 photocatalysis involves adsorption onto catalyst and the loss of membrane integrity.* Fems Microbiology Letters, 2006. 258(1): p. 18-24.

192. Cho, M., et al., *Different inactivation Behaviors of MS-2 phage and Escherichia coli in TiO2 photocatalytic disinfection.* Applied and Environmental Microbiology, 2005. 71(1): p. 270-275.

193. Sutherland, I.W., *Microbial exopolysaccharides - their role in microbial adhesion in aqueous systems.* Crc Critical Reviews in Microbiology, 1983. 10(2): p. 173-201.

194. Cescutti, P., et al., *Structural determination of the acidic exopolysaccharide produced by a Pseudomonas sp strain 1.15.* Carbohydrate Research, 1999. 315(1-2): p. 159-168.

195. Fang, H.H.P. and X.S. Jia, *Extraction of extracellular polymer from anaerobic sludges.* Biotechnology Techniques, 1996. 10(11): p. 803-808.

196. Veiga, M.C., et al., *Composition and role of extracellular polymers in methanogenic granules.* Applied and Environmental Microbiology, 1997. 63(2): p. 403-407.

197. Zhang, X.Q., P.L. Bishop, and B.K. Kinkle, *Comparison of extraction methods for quantifying extracellular polymers in biofilms.* Water Science and Technology, 1999. 39(7): p. 211-218.

198. Jagger, J., *Solar-UV Actions on Living Cells*1985, New York: Praeger Publishers.

199. Webb, R.B. and M.S. Brown, *Action spectra for oxygen-dependent and independent inactivation of Escherichia-coli-WP2s from 254-nm to 460-nm.* Photochemistry and Photobiology, 1979. 29(2): p. 407-409.

200. Maness, P.C., et al., *Bactericidal activity of photocatalytic TiO2 reaction: Toward an understanding of its killing mechanism.* Applied and Environmental Microbiology, 1999. 65(9): p. 4094-4098.

201. Sunada, K., T. Watanabe, and K. Hashimoto, *Studies on photokilling of bacteria on TiO2 thin film.* Journal of Photochemistry and Photobiology a-Chemistry, 2003. 156(1-3): p. 227-233.

202. Watts, R.J., et al., *Photocatalytic inactivation of coliform bacteria and viruses in secondary waste-water effluent.* Water Research, 1995. 29(1): p. 95-100.

203. Rincon, A.G. and C. Pulgarin, *Bactericidal action of illuminated TiO2 on pure Escherichia coli and natural bacterial consortia: post-irradiation events in the dark and assessment of the effective disinfection time.* Applied Catalysis B-Environmental, 2004. 49(2): p. 99-112.

204. Ferris, F.G. and T.J. Beveridge, *Functions of bacterial-cell surface-structures.* Bioscience, 1985. 35(3): p. 172-177.

205. Watanabe, M., et al., *Flocculating property of extracellular polymeric substance derived from a marine photosynthetic bacterium, Rhodovulum sp.* Journal of Bioscience and Bioengineering, 1999. 87(5): p. 625-629.

206. Frank, B.P. and G. Belfort, *Polysaccharides and sticky membrane surfaces: critical ionic effects.* Journal of Membrane Science, 2003. 212(1-2): p. 205-212.

207. Olofsson, A.C., M. Hermansson, and H. Elwing, *N-acetyl-L-cysteine affects growth, extracellular polysaccharide production, and bacterial biofilm formation on solid surfaces.* Applied and Environmental Microbiology, 2003. 69(8): p. 4814-4822.

208. Sutherland, I.W., *Microbial exopolysaccharides - structural subtleties and their consequences.* Pure and Applied Chemistry, 1997. 69(9): p. 1911-1917.

209. Kiraly, Z., H.M. ElZahaby, and Z. Klement, *Role of extracellular polysaccharide (EPS) slime of plant pathogenic bacteria in protecting cells to reactive oxygen species.* Journal of Phytopathology-Phytopathologische Zeitschrift, 1997. 145(2-3): p. 59-68.

210. Fantel, A.G., *Reactive oxygen species in developmental toxicity: Review and hypothesis.* Teratology, 1996. 53(3): p. 196-217.

211. Liu, Y., et al., *Bactericidal activity of nitrogen-doped metal oxide nanocatalysts and the influence of bacterial extracellular polymeric substances (EPS).* Journal of Photochemistry and Photobiology a-Chemistry, 2007. 190(1): p. 94-100.

212. Boulos, L., et al., *LIVE/DEAD (R) BacLight (TM): application of a new rapid staining method for direct enumeration of viable and total bacteria in drinking water.* Journal of Microbiological Methods, 1999. 37(1): p. 77-86.

213. Mack, J. and J.R. Bolton, *Photochemistry of nitrite and nitrate in aqueous solution: a review.* Journal of Photochemistry and Photobiology a-Chemistry, 1999. 128(1-3): p. 1-13.

214. Dubrovsky, N.M., and Hamilton, P.A., *Nutrients in the Nation's streams and groundwater: National Findings and Implications: U.S. Geological Survey Fact Sheet* USGS, Editor 2010.

215. Vaughan, P.P. and N.V. Blough, *Photochemical Formation of Hydroxyl Radical by Constituents of Natural Waters.* Environmental Science & Technology, 1998. 32(19): p. 2947-2953.

216. Kohn, T., et al., *Association with natural organic matter enhances the sunlight-mediated inactivation of MS2 coliphage by singlet oxygen.* Environmental Science & Technology, 2007. 41(13): p. 4626-4632.

217. Latch, D.E. and K. McNeill, *Microheterogeneity of singlet oxygen distributions in irradiated humic acid solutions.* Science, 2006. 311(5768): p. 1743-1747.

218. Hatchard, C.G. and C.A. Parker, *A new sensitive chemical actinometer .2. potassium ferrioxalate as a standard chemical actinometer.* Proceedings of the Royal Society of London Series a-Mathematical and Physical Sciences, 1956. 235(1203): p. 518-536.

219. Haznedaroglu, B.Z., C.H. Bolster, and S.L. Walker, *The role of starvation on Escherichia coli adhesion and transport in saturated porous media.* Water Research, 2008. 42(6-7): p. 1547-1554.

220. Bolster, C.H., et al., *Correlating Transport Behavior with Cell Properties for Eight Porcine Escherichia coil Isolates.* Environmental Science & Technology, 2010. 44(13): p. 5008-5014.

221. Kim, H.N., et al., *Surface Characteristics and Adhesion Behavior of Escherichia coli O157:H7: Role of Extracellular Macromolecules.* Biomacromolecules, 2009. 10(9): p. 2556-2564.

222. Gong, A.S., et al., *Extraction and Analysis of Extracellular Polymeric Substances: Comparison of Methods and Extracellular Polymeric Substance Levels in Salmonella pullorum SA 1685.* Environmental Engineering Science, 2009. 26(10): p. 1523-1532.

223. Liu, Y., C.H. Yang, and J. Li, *Influence of extracellular polymeric substances on Pseudomonas aeruginosa transport and deposition profiles in porous media.* Environmental Science & Technology, 2007. 41(1): p. 198-205.

224. Dubois, M., et al., *Colorimetric method for determination of sugars and related substances.* Analytical Chemistry, 1956. 28(3): p. 350-356.

225. Lowry, O.H., et al., *Protein measurement with the Folin phenol reagent.* Journal of Biological Chemistry, 1951. 193(1): p. 265-275.

226. Wegelin, M., et al., *Solar water disinfection: Scope of the process and analysis of radiation experiments.* Aqua (Oxford), 1994. 43(4): p. 154-169.

227. Haag, W.R. and J. Hoigné, *Photo-sensitized oxidation in natural water via .OH radicals.* Chemosphere, 1985. 14(11-12): p. 1659-1671.

228. Ireland, J.C., et al., *Inactivation of Escherichia-coli by titanium-dioxide photocatalytic oxidation.* Applied and Environmental Microbiology, 1993. 59(5): p. 1668-1670.

229. Nielsen, P.H., A. Jahn, and R. Palmgren, *Conceptual model for production and composition of exopolymers in biofilms.* Water Science and Technology, 1997. 36(1): p. 11-19.

230. Gabor, F., et al., *Photobiological activity of exogenous and endogenous porphyrin derivatives in Escherichia coli and Enterococcus hirae cells.* Radiation and Environmental Biophysics, 2001. 40(2): p. 145-151.

231. Wigginton, K.R., et al., *Oxidation of Virus Proteins during UV254 and Singlet Oxygen Mediated Inactivation.* Environmental Science & Technology, 2010. 44(14): p. 5437-5443.

232. Rincon, A.G. and C. Pulgarin, *Effect of pH, inorganic ions, organic matter and H2O2 on E-coli K12 photocatalytic inactivation by TiO2 - Implications in solar water disinfection.* Applied Catalysis B-Environmental, 2004. 51(4): p. 283-302.

233. Rincon, A.G. and C. Pulgarin, *Solar photolytic and photocatalytic disinfection of water at laboratory and field scale. Effect of the chemical composition of water and study of the postirradiation events.* Transactions of the ASME. Journal of Solar Energy Engineering, 2007. 129(1): p. 100-10.